The University Of Sheffield.

Theoretical Investigations of Sources of Magnetism in cobalt-doped ZnO

A thesis submitted in partial fulfilment to the requirements for the degree of Doctor of

philosophy

University of Sheffield

Faculty of Science

Department of Physics and Astronomy

By: Fatma M. Gerriu

December 2018

Contents

Abstract

This thesis provides an original work towards understanding some of the magnetism sources in cobalt-doped ZnO. The point defects in ZnO were investigated by deriving an equation that gives an indication of the sign and the relative magnitude of the Magnetic Circular Dichroism (MCD) signal. The equation was derived by considering the effects of spin-orbit coupling on the defect states and the Zeeman interaction as perturbations. The relative strength of the expected signal was found to be proportional to the deviation of the g-factor from 2.00 as long as the spin-orbit coupling is much larger than the Zeeman energy.

Cobalt nanoparticles embedded in ZnO were modelled by multilayered structures sandwiched within pure and cobalt-doped ZnO lattice along the [0001]-direction. The magnetisation and the magnetic exchange energies between the metallic stacks were calculated by first principles. The modelled Co nanoparticles in pure ZnO were investigated in hcp and fcc phases. The calculations showed the preference of the hcp phase over the fcc. Except for the interfacial layers, the magnetisation and the charge of the Co layers were found to tend to bulk values as the number of the layers increases. The magnetic exchange interaction was found to be ferromagnetic in both Co phases. The model was repeated by doping the ZnO lattice with 12.5 at % Co. The results showed that the substitutional Co ions

have small magnetic moments compared to the values of the ions in metallic stacks which were found to approach bulk value with adding extra Co layers. The magnetic exchange was found to be antiferromagnetic which agrees with the experimental data. Moreover, the oxygen ions in the interfacial region, in both cases, were spin polarised in the same direction as that of the nanoparticle which is also in agreement with the experimental results.

Dedication

In the Name of Allah, the Most Beneficent, the Most Merciful

To my first educator who waited for long time to see this moment; my mother, the dearest "Amna Abu Fares"

To the memory of my father whom gave me the motivation to continue in this journey: "Meftah Gerriu"

To the memory of my grandmother;

"Muna"

To my husband who encourged me during my study,

"Mohamed"

To my children who were patient with me and waited long for this moment

" Ali, Sarah and Almuntaser"

To all my sisters and brothers who waited me to finish this long journey,

I dedicate this work

Acknowledgements

I would like to thank all people who helped me during the duration of my PhD. First, my special thanks go to my supervisor: Prof Gillian Gehring for her useful discussions, encouragement and friendship.

Secondly, I would like to thank my second supervisor: Prof Mark Fox, for being positive and supportive all the time. I really appreciate his support.

I would like to thank my financial sponsor: University of Misurata, the Ministry of Higher Education and Scientific Research and the Libyan Cultural Attaché in London for providing the funding for this work. A special appreciation goes to CASTEP community; namely Prof Matt Probert and Dr Phil Hasnip at York university and Prof Stewart Clark at the university of Durham for letting me participate in their training course on CASTEP and material modelling and for helping me as well as others to solve most technical problems via CASTEP email list. I really appreciate their support.

Many thanks to all my group colleagues Dr. Hasan Albargi, Dr. Wala Dizayee, Dr. Aliaa Zaki, and Mr. Ahmad Saeedi for being supportive. A special appreciation to my office colleague: Mr William S Fall for his computational assistance and being positive and helpful all the time.

Finally, I would like to express my sincere gratitude to my mother, husband, children,

brothers, sisters and friends for the patience, support, and continuous encouragement throughout my studies.

Publications

- Minju Ying, Shida Wang, Tao Duan, Bin Liao, Xu Zhang, Zengxia Mei, Xiaolong Du, **F.M.Gerriu**, A.M.Fox , G.A.Gehring, **The structure, optical and magnetic properties of arsenic implanted ZnO films prepared by molecular beam epitaxy**, Materials Letters171(2016)121–124.

- Minju Ying, Harry J. Blythe, Wala Dizayee, Steve M. Heald, **Fatma M. Gerriu**, A. Mark Fox, and Gillian A. Gehring, **Advantageous use of metallic cobalt in the target for pulsed laser deposition of cobalt-doped ZnO films**, Appl. Phys. Lett. 109, 072403 (2016).

- **Fatma M. Gerriu**, A. Mark Fox, and Gillian A. Gehring, **First principles modelling of Co nanoparticles embedded in ZnO**, *submitted to Magnetism and Magnetic Materials.*

- **Fatma M. Gerriu**, A. Mark Fox, and Gillian A. Gehring, **First Principles magnetisation study of Co nanoparticles in ZnCoO system**, the paper is under preparation.

Conferences and Workshops

- IoP postgraduate magnetism workshop, University of York, York, UK (December, 2015).
- First Principles Materials Modelling training course, University of York, York, UK (September-October, 2017).
- Fatma M. Gerriu, A. Mark Fox and Gillian Gehring, Poster "**Magnetic Circular Dichroism study of defects in ZnO**", the IoP Magnetism 2016, University of Sheffield, Sheffield, UK (April 2016).
- Fatma M. Gerriu, A. Mark Fox and Gillian Gehring, Poster "**The Origin of MCD from defect states in magnetic oxides** ", the IoP Magnetism 2017, University of York, York, UK (April 2017).
- Fatma M. Gerriu, A. Mark Fox and Gillian Gehring, Poster "**First principles study of Co nanoparticles in Co/ZnO system**", Magnetism 2018, University of Manchester, Manchester, UK (April 2018).

Chapter 1

Introduction and thesis structure

1.1 Introduction

Spintronics, also known as magneto-electronics, is an advancing promising technology which exploits the spin state of the electron as well as its charge. Controlling the spin flow within a device can result in fascinating properties. Various spintronic devices have been proposed such as the magnetoresistive random access memory (MRAM), spin field effect transistors, (Spin-LEDs) and others as shown in the schematic representation of spintronics in Figure (1.1). Therefore, integrating the electron spin, optical and electronic properties is a very hot research topic nowadays. The main issues controlling the efficiency of a spintronic device are how to effectively inject the spins into the material and then control their transport within the material and finally detect these spins. For high efficient spin injection, diluted magnetic semiconductors (DMSs), which can provide a source of spin polarised carriers, are being developed. A DMS is a semiconductor material that is doped with small concentration of magnetic elements as Figure (1.2) shows.

In order to develop a DMS, the material must be ferromagnetic; preferably with a high Curie temperature, T_C. Room temperature ferromagnetism (RTFM) has been reported in many oxide DMSs in the absence of the magnetic clusters. However, the origin of such observed FM is still controversial. XMCD measurements implemented on cobalt-doped ZnO samples by Tietz et *al* [1] has shown that the substitutional cobalt ions are paramagnetic and hence they suggested that the observed magnetisation is due to defects, in particular due to oxygen vacancies [2, 3] or zinc vacancy states [4, 5]. Other studies by Straumel et al suggested the source is the grain boundaries in nanograined TM-doped ZnO samples [6–9].

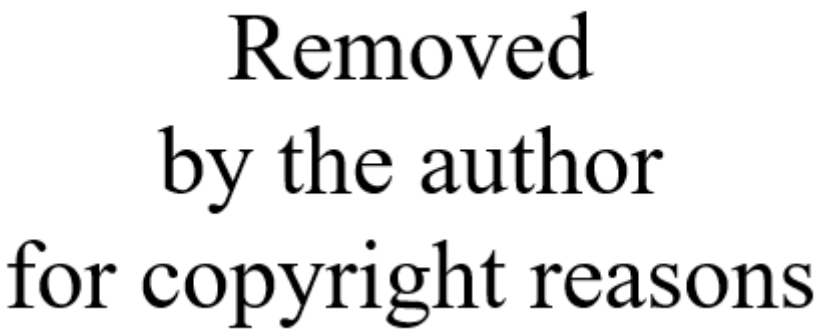

Figure 1.1: A schematic sketch of the idea of the spintronics.

ZnO is a promising material in spintronics and other optical devices. The material has a wide band gap ~ 3.4 eV, so that it can be operated with high power and at high temperatures. In addition, a room temperature long spin coherence time has been reported for n-type bulk ZnO [11] which is a desired property in spintronics. The availability of high quality ZnO bulk single crystals and the simple growth techniques of ZnO samples make the fabrication of ZnO-based devices cheaper compared to other materials [12]. Spin injection from a doped ZnO layer to a pure ZnO or another conventional semiconductor

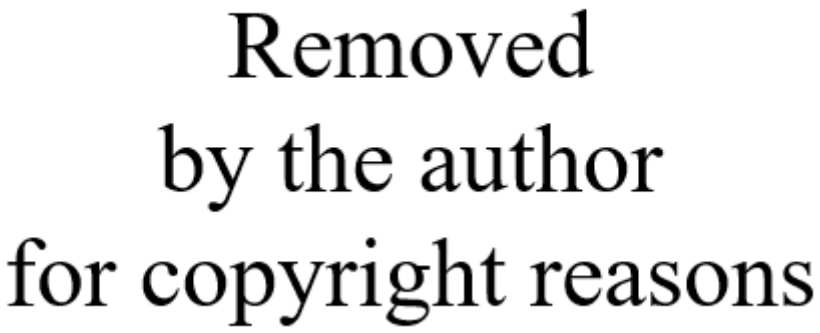

Figure 1.2: Comparison between magnetic semiconductors (A), diluted magnetic semiconductors (B), and non-magnetic semiconductors (C), adopted from [10].

layer is a vital long-term goal of the study of ZnO as a DMS [13]. The spin manipulation in Co-doped ZnO has been reported to result in the observation of tunnel magnetoresistance (TMR) [13–15]. It has also been shown that the material can be stably switched at different resistance states manipulated by an electric and a magnetic field. This has led to a developement of a novel electrode/ZnO/ZnO-Co/electrode storage device referred to as resistive random access memory (ReRAM) as shown in Figures (1.3) and (1.4) [16]. Furthermore, the reported electron- and hole-mediated ferromagnetism reported in TM doped ZnO samples makes it applicable in bipolar spintronic devices [17]. However, there have been some drawbacks before realizing such applications. These include the difficulty in reproducing p-type conductivity and diluted magnetic doping [18].

Controlling sources of the observed room temperature ferromagnetism in ZnO is an important step towards its application as a DMS material that can be exploited in other applications. These sources can be native such as lattice defects; point defects and grain boundaries, or secondary phases such as metallic nanoparticles of the doped transition metals. Co-doped ZnO material has been among the most intensively investigated DMS

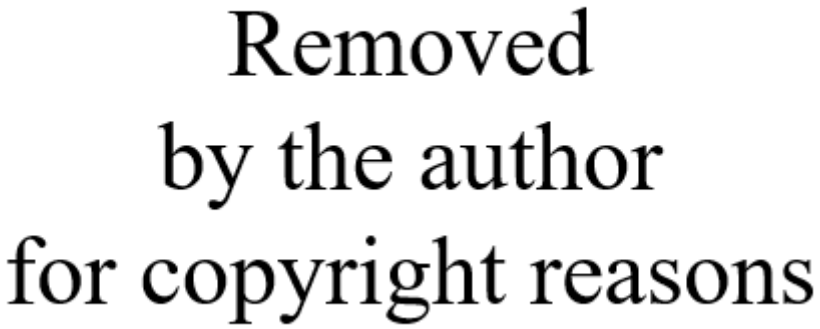

Figure 1.3: A schematic structure of the Pt/ZnO/ZnO-Co/Au sample which has been shown to exhibit a resistive switching behaviour, adopted from [16].

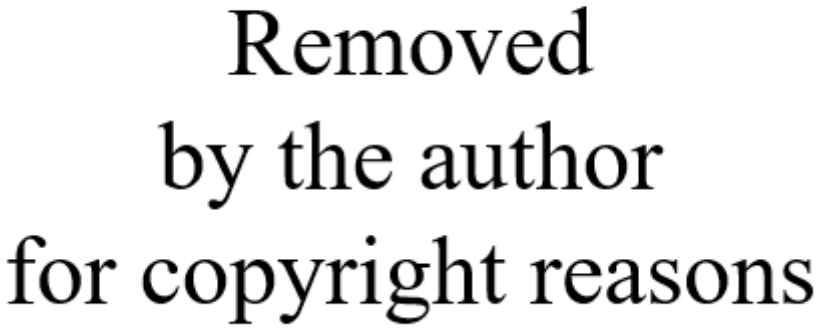

Figure 1.4: (a) The I–V curve of the ZnO/ZnO-Co sample in a semilogarithmic scale at room temperature. The arrows indicate the sweeping directions of the voltage. The magnetic field dependence of room temperature MR ratio of the sample at the high resistance state (HRS) (b) and the low resistance state (LRS) (c), dopted from [16].

candidates [19]. However, the reported results in the literature are still controversial. Some studies reported observing ferromagnetism even in small concentration of Co [20], others have either observed a negligible magnetisation [21] or failed to achieve any ferromagnetism in high quality Co-doped thin films [22], or in bulk polycrystalline samples [23] which has suggested the role of defects in mediating ferromagnetism. Other reports have found that a fraction of the doped Co atoms cluster into metallic Co nanoparticles under

certain preparation conditions and post-growth treatments such as preparing the samples in a low oxygen atmosphere [24], or annealing the prepared specimen in a reduced oxygen atmosphere [25]. The resulting metallic phase can be detected by X-ray absorption techniques [26] and they have been found to enhance the observed room temperature ferromagnetism and their magnetic contribution can be further coupled to the semiconducting contribution if more carriers are added when the samples are co-doped with Al [27]. Co nanoparticles embedded in ZnO have been found to enhance the observed magnetoresistance (MR) values due to spin dependent tunelling via the interfacial region [28]. These types of samples can be exploited in sensing applications and as spin-injectors in semiconductors.

The work in this thesis contributes towards a theoretical modelling of sources of magnetism in cobalt-doped ZnO material. It is divided into two main parts. The first part is a theoretical derivation of Magnetic Circular Dichroism (MCD) equation due to point defects in ZnO. Using MCD as a characterisation tool enables us to distinguish between different possible point defects that may be the source of the observed room temperature ferromagnetism in samples with no metallic contamination. The second part is a Density Functional Theory (DFT) modelling of Co nanoparticles in ZnO. The model is concerned with the interfacial region of the nanoparticle and the semiconducting region. The magnetisation and exchange energies of the nanoparticles in pure and Co-doped ZnO supercells were evaluated and discussed in details.

1.2 Thesis Structure

The work in the thesis presents an investigation of the role of defects in mediating ferromagnetism in Co-doped ZnO by means of simple quantum mechanics. It also includes the first original study of Co nanoparticles in ZnO using density functional theory as implemented in CASTEP. The body of the thesis consists of seven chapters as follows:

- **Chapter 1** contains the introduction of the thesis.
- **Chapter 2**: presents a brief discussion on magnetism and magnetic materials, types of the magnetic exchange, and a discussion of the behaviour of magnetic nanoparticles.
- **Chapter 3**: presents a simple QM study of MCD signal due to point defects in ZnO. In this chapter, the details of the derivation and a comparison to experimental data available were shown in detail.
- **Chapter 4**: describes the basics of the Density Functional Theory (DFT) method which was used in the second part of the thesis to form the basic background to explain the results presented in the rest of the thesis.
- **Chapter 5**: presents the model of Co nanaoparticles embeded in pure ZnO. In this chapter, the magnetisation of the Co layers as well as ZnO at the interface were addressed for Co hcp and fcc structures. Additionally, the magnetic exchange energies between the modelled nanoparticles were calculated.
- **Chapter 6**: contains a comparison of the magnetism of and the exchange between Co monolayers in a more realistic model in Co-doped ZnO supercells since experimentally the nanoparticles form as a fraction of the doped Co.

- Finally **chapter 7** draws the main conclusions of the thesis and future work suggestions.

Chapter 2

A review of magnetism

2.1 Introduction

Magnetic materials are essential in many applications nowadays, such as data storage, medical applications and power generation. The interesting magnetic effects found in these materials have two main origins: first, the atoms have magnetic moments and second, these moments interact with each other in a particular way to create some magnetic order.

This chapter introduces the basic magnetic concepts relevant to the investigation in this thesis. In particular, the fundamentals of magnetism and magnetic materials are introduced in sections 2.2 and 2.3, respectively. The origins of the exchange interactions which form the main aim of this work are presented in section 2.4. Finally, the fundamental behaviours of magnetic nanoparticles are discussed in details in section 2.5, in order to form a basic background to understand the literature and the results presented in

this work for Co nanoparticles in ZnO. The brief introduction to principles of magnetism in this chapter is based on several text books: Introduction to Solid State Physics by C. Kittel [29], Introduction to Magnetic Materials by B.D. Cullity [30], Magnetism and Magnetic Materials by J. M. D. Coey [31], Magnetic Materials Fundamentals and Device Applications by N. A. Spaldin [32], The Magnetic Properties of Solids by J.R Crangle [33], and Magnetism in condensed matter by S Blundell [34].

2.2 Basics of magnetism

2.2.1 Isolated atoms

In order to understand the atomic origin of the magnetic moment and hence the magnetisation, one has to consider the two angular momenta of isolated atoms; the orbital and the spin angular momentum and the interaction between them. The basic ingredient to form the magnetisation is the magnetic moment, **m**, which is defined classically for a current loop with area A, carrying current I as;

$$\mathbf{m} = I\mathbf{A} \tag{2.1}$$

In SI unit, it is measured in A.m^2, and in emu in cgs units. The latter is more commonly used in the literature. Therefore, for an electron (mass m, charge -e) circulating around a nucleus with angular velocity $\omega = v/r$, the magnitude of the magnetic moment is

$$|\mathbf{m}| = I|\mathbf{A}| = (-e\omega/2\pi)(\pi r^2) = -e\omega r^2/2 \tag{2.2}$$

Classically, the orbital angular momentum of the electron is given as

$$|\mathbf{L}| = m|\mathbf{r} \times \mathbf{v}| = m\omega r^2 \tag{2.3}$$

hence, and from (2.2) and (2.3), the relationship between the magnetic moment and the orbital angular moment is linear;

$$\mathbf{m} = \frac{-e}{2m}\mathbf{L} \tag{2.4}$$

Quantum mechanically, the orbital angular momentum is quantised in units of $\hbar$. Therefore, the lowest value of L is $\hbar$, and thus, the minimum non-zero value of the magnetic moment of the electron is $\mu_B = \frac{e\hbar}{2m} = 9.27 \times 10^{-24} JT^{-1}$ which is referred to as Bohr magneton and it is used as a natural unit of expressing magnetic moments. As the orbital momentum is quantised and linearly connected to the magnetic moment, the latter is also quantised but in units of μ_B;

$$\mathbf{m}_l = -g_l \mu_B \mathbf{L} \tag{2.5}$$

Where $g_l = 1$ is the orbital g-factor. In external magnetic field in z-direction, the component of the magnetic moment in the field direction is given as

$$m_{lz} = -\mu_B m_l \tag{2.6}$$

Where m_l is the orbital momentum component parallel to the applied field, and it can only take integer values between $-l$ and l. Moreover, electrons also possess another type of angular momentum, the spin angular momentum, which gives rise to an extra contribution to the magnetic moment;

$$\mathbf{m}_s = -g_s \frac{e\hbar}{2m}\mathbf{S} = -g_s \mu_B \mathbf{S} \tag{2.7}$$

Where, $g_s = 2.002290716(10)$ is the spectroscopic splitting factor (or the g-factor for the free electrons). Like the orbital contribution, the parallel component to the field of the magnetic moment is

$$m_{sz} = -g_s \mu_B m_s \tag{2.8}$$

Where m_s is the spin angular momentum component parallel to the applied field, and it can only take values of $\pm\frac{1}{2}$. Therefore, the spin magnetic moment parallel to the field can only have $\pm\mu_B$.

For many-electron atoms, the total orbital angular momentum is given by summing all over the electronic orbital angular momenta.

$$\mathbf{L} = \sum_i l_i \tag{2.9}$$

Thus, the total orbital angular momentum for a complete shell is zero, and the only non-zero contributions arise from the incomplete shell. Similarly, the total spin angular momentum is

$$\mathbf{S} = \sum_i s_i \tag{2.10}$$

In addition, the total angular momentum **J** results by the combination of **L** and **S** through the spin-orbit interaction. The spin-orbit coupling originates from the interaction between the spin magnetic moment and the magnetic field originated by the orbital motion. Furthermore, it is a weak relativistic effect responsible for Hund's third rule as it will be discussed later. Moreover, it is the origin of several interesting phenomena; such as magnetocrystalline anisotropy, magnetostriction, and anisotropic magnetoresistance. The interaction is weak for light elements, however, becomes very important for heavy elements since it goes as $\sim Z^4$ [31].

The coupling between the two angular momenta can have two situations. First when the spin-orbit is weaker than the residual electrostatic interaction and this occurs in atoms with small and medium atomic number. In this case, the coupling between the total L and S and is called LS coupling or the Russell-Saunders coupling. Filled shells do not contribute to the total L and S and hence the summations in (2.9) and (2.10) only

needs to be performed over the valence electrons. The angular momentum summation rule usually allows several possible values of L and S for a particular electronic configuration and they differ in energy due to the residual electrostatic interaction. The atomic state defined by a particular L and S are called atomic term. For each term, total angular momentum of the atom can be found as

$$\mathbf{J} = \mathbf{L} + \mathbf{S} \tag{2.11}$$

The states of different J for each LS-term have different energies due to the spin-orbit interaction.

On the other hand, the second situation which is more common and only important in heavy elements is the jj coupling. In this case the spin-orbit interaction is much stronger than the residual electrostatic interaction. In this regime, since the spin-orbit interaction is strong, it couples the spin and the orbital angular momenta of the individual electrons first, the resultant total angular momentum J is found by summing all the individual j of each valence electron;

$$\mathbf{j}_i = \mathbf{l}_i + \mathbf{s}_i \tag{2.12}$$

$$\mathbf{J} = \sum_{i=1}^{N} \mathbf{j}_i \tag{2.13}$$

LS coupling regime is common for most elements and more important than the jj coupling scheme, since a particular configuration can have several atomic terms which will be split further by the spin-orbit interaction.

2.2.2 Hund's rules for atoms

In an atom, the energy of a single electron is described via the four quantum numbers, n, l, m_l and m_s. According to the Pauli exclusion principle, no two electrons can have same quantum numbers, i.e. same energy state. In order to determine the lowest energy state of a multi-electron atom, Hund's rules are developed. These rules are:

- The value of the total spin angular momentum S, for the electrons in the open subshell, takes its maximum as far as it is allowed by Pauli exclusion principle. Firstly, it was proposed that electrons in different orbitals are further apart and hence the electrostatic repulsion energy is minimised. However, a more accurate quantum-mechanical description has been later given. The electrons when singly occupy the orbitals, they are less screened so that such orbitals are contract and thus electron-nucleus attraction energy decreases [35].

- The value of the total orbital angular momentum also takes its maximum as far as it is not contradicting with the first rule. This can be explained considering the classical picture of the orbits. When the electrons are orbiting in the same direction which means higher total orbital angular momentum, the electron-electron repulsion energy is minimized since the electrons meet less often than if some of them orbit in opposite directions, and hence the value of L is maximised.

- If the shell is less than half-full, the total angular momentum is $\mathbf{J} = |\mathbf{L} - \mathbf{S}|$, if it is, otherwise, more than half-full, $\mathbf{J} = |\mathbf{L} + \mathbf{S}|$. For half-filled shell L=0 and hence $\mathbf{J} = \mathbf{S}$. This is to do with the energy shifts due to spin–orbit coupling when it is weak compared to the residual electrostatic interaction. The spin-orbit coupling term gives the dependence of the ground state energy on the magnitude of $\mathbf{J}$.

2.2.3 Atoms and ions in solids

So far we talked about isolated atoms and ions. Now, we consider what happens when atoms/ions are placed in a crystal, i.e. when the effect of the surrounding environment is addressed.

Crystal field

Crystal field is an electric field which results from the surrounding atoms or ions in the crystal. The orbitals of the surrounding atoms are simply modelled as negative point charges according to the crystal-field theory. Ligand-field theory improves the approximations in the former and focuses on the overlap between d-orbitals of the transition metal with neighbouring ions (ligands). The symmetry of the local environment determines the strength and the nature of the field.

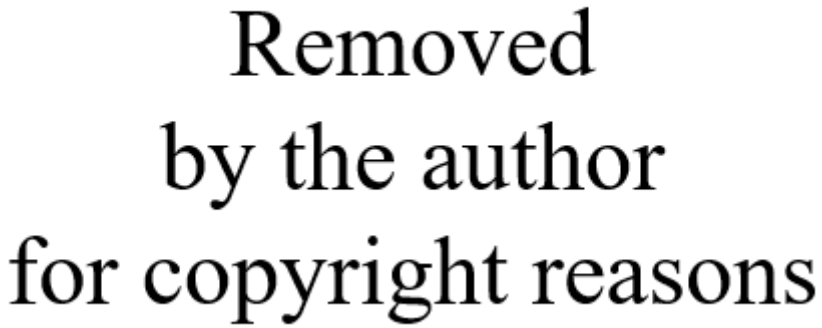

Figure 2.1: Angular distributions of s, p, and d-orbitals, with e_g and t_{2g} classes of d-orbitals are identified. Adopted from [36].

Before discussing the crystal-field effects in different environments, the symmetry of the orbitals and the classifications of the d-orbitals are presented. Figure (2.1) shows the

angular distributions of the s, p, and d-orbitals with the two classes of the d-orbitals are identified. The s-orbitals are symmetrically distributed, whereas the p-orbitals have lobes pointing along x, y and z axes. There are two groups of d-orbitals, the first group has orbitals pointing between the Cartesian axes, these are d_{xy}, d_{yz}, and d_{xz} orbitals. This class of orbitals are called the t_{2g}. The second class includes orbitals pointing along the axes, these are $d_{x^2-y^2}$ with lobes along x and y axes, and d_{z^2} with lobes pointing along the z-axis, these are called e_g.

If a transition metal (TM) ion is placed at the centre of an octahedron of oxygen ions, as in magnetites, the effect of the crystal field on the TM depends on the type of the d-orbital being from the t_{2g} or e_g classes. For the t_{2g} orbitals, such as d_{xy} shown in Figure (2.2 a), the overlap between the d-orbitals of the TM and the p-orbitals of the oxygen is lower than that of the e_g orbitals , as shown in Figure (2.2 b) for the $d_{x^2-y^2}$ orbitals. Therefore, the energy of the t_{2g} orbitals is lower than the energy of the e_g orbitals, and hence the crystal field splits the two d-orbital groups by an energy Δ which is called the crystal field splitting with the t_{2g} orbitals lowered by 0.4Δ and the e_g orbitals raised by 0.6Δ as shown in Figure (2.3 a).

In a tetrahedral environment, the effect of the crystal field is exactly the opposite of that in the octahedral environment and hence the two-fold e_g orbitals are lower in energy than the three-fold t_{2g} orbitals as shown in Figure (3b).

To fill the electronic states of the incomplete d-shell, for example in the octahedral environment, the electrons will occupy the lowest levels first. However, there is a com-

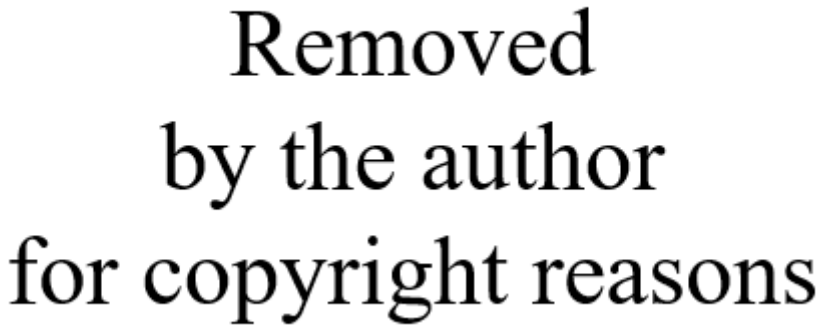

Figure 2.2: An x-y projection of a TM d-orbitals in an octahedral environment. (a) The overlap of the d_{xy} orbitals is lower than that of (b) $d_{x^2-y^2}$, adopted from [34].

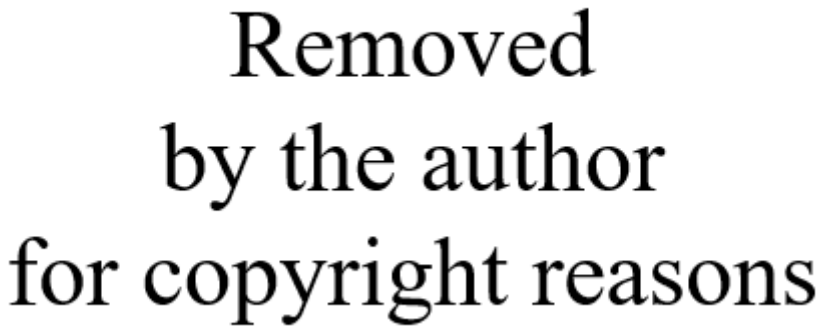

Figure 2.3: Crystal field splitting in (a) an octahedral and (b) tetrahedral environments, adopted from [36].

petition between two energies, namely the crystal-field energy and the pairing energy. In the weak-field limit, when the crystal field energy is lower than the pairing energy, the electrons will singly occupy all levels first before any orbital is doubly occupied. However, in the strong field limit, each orbital is doubly occupied by electrons first before moving to higher levels.

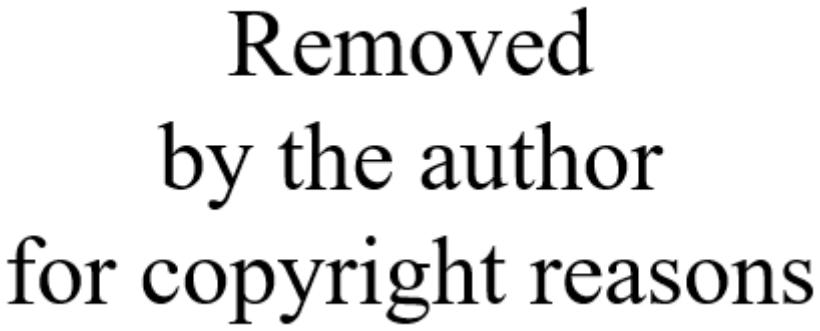

Figure 2.4: Calculated S, L, J and ground state energy terms with effective magnetic moment, p_1 according to Hund's rules against observed effective moment, p_{exp} and effective magnetic moment due to spin only, p_2, adopted from [34].

Orbital quenching

Figure (2.4) shows a table of expected effective magnetic moment, p_1, and experimental magnetic moments of the transition metal ions, p_{exp}. Values of S, L, J and expected moment $p_1 = g_J[J(J+1)]^{\frac{1}{2}}$ are calculated according to Hund's rules outlined in section 2.2. With an exception of half- or completely full d-orbitals, there is large discrepancy between the expected effective moment, p_1 and the experimental values, p_{exp}. The reason for this discrepancy for the 3d ions that the crystal field interaction is much stronger than the spin-orbit interaction. This suggests that Hund's third rule which assumes that the spin-orbit interaction is the second stronger interaction after Coulomb interaction is not valid in this case. The data show a better agreement if the effective moment is calculated considering L=0 and hence J=S, $g_J = 2$ and

$$\mu_{eff} = 2\mu_B\sqrt{S(S+1)} = p_2\mu_B. \tag{2.14}$$

As shown in the table, this results in a better agreement between p_{exp} and p_2, and this effect is known as orbital quenching. This happens because the crystal field is strong for

the 3d ions and hence forces the orbital angular momentum to be strongly bound to the lattice preventing it from contributing to the total angular momentum and hence to the total magnetic moment. This has no effect on the spin because of the weaker spin-orbit interaction.

Orbital quenching is less important in the 4f ions and the higher transition metal ions(4d and 5d series). In the 4f ions case, the orbitals are more localised so that the crystal field interaction is less important and Hund's rules obeyed. For the heavier transition metals, the spin-orbit coupling becomes significant and may be comparable to the crystal field interaction.

2.3 Magnetic materials

When a material is placed in an external magnetic field **H**, the response of the material is called its magnetic induction, **B** measured in $Tesla$ in SI and $gauss$ in cgs units. The relationship between these two quantities is a property of the material. This relation in cgs units can be written as:

$$\mathbf{B} = \mu_0(\mathbf{H} + \mathbf{M}) \tag{2.15}$$

, where **M** is the magnetisation of the medium and it is defined as a measure of the magnetic moment per unit volume;

$$\mathbf{M} = \frac{\mu}{V} \tag{2.16}$$

measured in A/m in SI units and with emu/cm^3 in cgs unit system. The quantity **M** is also a property of the material, and it is determined by the individual magnetic moments

of the constituents and the interactions between these moments. In addition, the way that these quantities, **M** and **B**, vary with the external magnetic field also matters.

The susceptibility, χ, is another characteristic property for the magnetic behaviour of the material. It is defined as the ratio between the magnetisation and the applied magnetic field in low field limit:

$$\chi = \lim_{H \to 0} \frac{\partial \mathbf{M}}{\partial \mathbf{H}} \tag{2.17}$$

It is a dimensionless quantity since H and M have the same units.

There is another important characteristic feature which is a measure of how permeable the material is to the magnetic field. It is defined as the ratio of the magnetic induction to the magnetic field also in the linear regime.

$$\mu = \frac{\mathbf{B}}{\mathbf{H}} \tag{2.18}$$

It is measured in Henry/meter $H.m^{-1}$. By using equations (2.15), (2.17) and (2.18); it can be shown that the relation between the permeability and the susceptibility is linear:

$$\mu = \mu_0(1 + \chi) \tag{2.19}$$

Where μ_0 is the permeability of the free space.

2.3.1 Non-hysteretic materials

Magnetic behaviour of the material is mainly determined by graphs of **M** or **B** versus **H** and these are called magnetisation curves. If the curve is linear going through the origin and the slope is very small and negative as well as the permeability is slightly less than unity, the material is referred to as diamagnetic.

Similarly, if the relation is linear but the susceptibility is small and positive and the permeability is slightly greater than unity, the material is either paramagnetic or antiferromagnetic. What is common in all the previous classifications is that no magnetism is retained when the applied magnetic field is removed.

2.3.2 Hysteretic materials

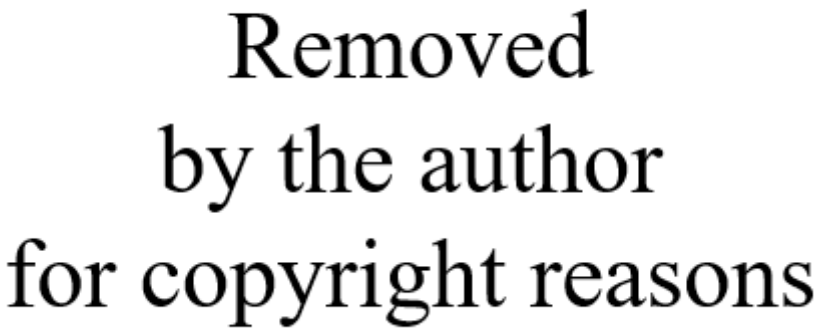

Figure 2.5: A sketch of a hysteresis loop indicting the coercive field ,H_c, the remnant magnetisation, M_r, and the saturation magnetisation, M_s values. Adopted from [34].

Another class of materials which is usually more interesting for applications is one in which a very large magnetisation is caused by applying a small magnetic field is called ferromagnetic. The magnetisation saturates above a certain magnetic field value where increasing the magnetic field beyond that value does not affect the magnetisation and the magnetisation value is referred to as the saturation magnetisation, M_S. Moreover, by decreasing the magnetic field to zero, the **M-H** curve follow a new pattern and the magnetisation at zero field does not vanish, rather it has a particular value known as the remnant magnetisation M_r. Similarly, when the sample is completely demagnetised, the magnetic field has non-zero value called the coercive field, H_C. This characteristic

behaviour of the material is known as hysteresis as shown in Figure (2.5) and it is vital in technological applications.

2.4 Exchange interactions

Exchange interactions are important interactions between the magnetic moments so that some order may be produced. It is nothing but Coulomb electrostatic interaction resulting because same spins prefer to be apart from each other to save energy. In the following subsections, a discussion of the origin of the exchange as well as the main exchange mechanisms in insulators and metals are introduced.

2.4.1 Origins of exchange

Considering a simple model of just two electrons at $\mathbf{r}_1$ and $\mathbf{r}_2$ respectively; the wavefunction of the joint state of the electrons can be written as a product of the single electron wavefunctions. Thus, if one of the electrons in state $\psi_a(\mathbf{r}_1)$ and the other is in state $\psi_b(\mathbf{r}_2)$, the joint state of both is $\psi_a(\mathbf{r}_1)\psi_b(\mathbf{r}_2)$. However, if the two electrons are exchanged, the product $\psi_a(\mathbf{r}_1)\psi_b(\mathbf{r}_2)$ does not obey the exchange symmetry. Consequently, the only allowed states are:

$$\psi_S = \frac{1}{\sqrt{2}}[\psi_a(\mathbf{r}_1)\psi_b(\mathbf{r}_2) + \psi_a(\mathbf{r}_2)\psi_b(\mathbf{r}_1)]\chi_S \tag{2.20}$$

and

$$\psi_T = \frac{1}{\sqrt{2}}[\psi_a(\mathbf{r}_1)\psi_b(\mathbf{r}_2) - \psi_a(\mathbf{r}_2)\psi_b(\mathbf{r}_1)]\chi_T \tag{2.21}$$

which represent the singlet and the triplet states respectively. The singlet spin state is symmetric in space and antisymmetric in spin, whereas the triplet state has exactly the reverse spatial and the spin symmetry. The energy difference between these two states can be written as:

$$E_S - E_T = 2 \int \psi_a^*(\mathbf{r}_1)\psi_b^*(\mathbf{r}_2)\hat{H}\psi_a(\mathbf{r}_2)\psi_b(\mathbf{r}_1)d\mathbf{r}_1 d\mathbf{r}_2 \tag{2.22}$$

and by parametrising the difference using the product $\mathbf{s}_1.\mathbf{s}_2$, where $\mathbf{s}_1$ and $\mathbf{s}_2$ are the single electron spins, the Hamiltonian can be written as:

$$\hat{H} = \frac{1}{4}(E_S + 3E_T) - (E_S - E_T)\mathbf{s}_1.\mathbf{s}_2 \tag{2.23}$$

where the first term is constant and can be absorbed in energy. The second is more interesting which carries the effective exchange Hamiltonian. Therefore, if the exchange constant (or exchange integral), $\mathbf{J}$ is defined as

$$J = \frac{E_S - E_T}{2} = \int \psi_a^*(\mathbf{r}_1)\psi_b^*(\mathbf{r}_2)\hat{H}\psi_a(\mathbf{r}_2)\psi_b(\mathbf{r}_1)d\mathbf{r}_1 d\mathbf{r}_2$$

The effective exchange Hamiltonian is:

$$\hat{H}_{ex} = -2\mathbf{J}\mathbf{s}_1.\mathbf{s}_2 \tag{2.24}$$

where as it can be seen from the definition of J if $J > 0$, $E_S > E_T$, and hence the triplet state is favoured, otherwise, if $J < 0$, $E_S < E_T$, and thus the singlet state is energetically favourable.

The previous simple model can be generalised to many-body system by applying the interaction between all neighbouring atoms. Thus, the Hamiltonian is given by Heisenberg model:

$$\hat{H} = -\sum_{i \neq j} J_{ij}\mathbf{S}_i.\mathbf{S}_j \tag{2.25}$$

or can be rewritten:

$$\hat{H} = -2\sum_{i>j} J_{ij}\mathbf{S}_i.\mathbf{S}_j, \tag{2.26}$$

if the double counting is avoided, where $\mathbf{S}_i$ and $\mathbf{S}_j$ are the total spins of the interacting atoms/ions. Therefore, the interaction, as it is described by the previous Hamiltonian, can be either ferromagnetic or antiferromagnetic depending on the sign of the exchange constant being positive or negative, respectively.

The type of the magnetic order of the material depends mainly on the exchange interaction. Additionally, the exchange coupling of the magnetic moments results from the competition between the kinetic energy and the Coulomb repulsion. There are various classifications of such interactions in solids depending on moments being localised or delocalised, the interaction being short or long-ranged, and whether they lead to FM or AFM alignment. In the following, the exchange interactions will be discussed according to their occurrence in metals and insulators. For the work presented in chapters 5 and 6, the relevant exchange interaction for cobalt magnetism is the band magnetism. For the exchange interaction of Co ions at the ZnO interface through the oxygen ions is the superexchange interaction.

2.4.2 Exchange in insulators

Superexchange and Goodenough-Kanamori rules

The interaction that can occur in insulators, usually in oxides, sulphides, and fluorides, is the superexchange interaction where there is a virtual hopping of the O-2p electrons. It occurs, for example, in transition metal oxides with a singly occupied 3d-orbital or a

half-filled d shell (Fe^{3+}, Mn^{2+}) in MnO and Fe_2O_3 or between Mn^{3+} ions in $LaMnO_3$. It is short ranged compared to the Coulomb interaction. Moreover, it is indirect since it happens between non-neighbouring magnetic cations via an intervening non-magnetic anion. In oxides, it depends on the hybridization of the 3d orbital with the oxygen 2p orbital; $\psi_{3d} = \alpha\psi_{3d}+\beta\psi_{2p}$ and $|\alpha|^2+|\beta|^2 = 1$. The coupling between the magnetic ions can be either ferromagnetic or antiferromagnetic depending on the 3d orbital occupancy (the number of the electrons, and e_g or t_{2g} character) and the cation-anion-cation bond angle, varying as $cos^2\theta$ [31]. The so called Goodenough-Kanamori-Anderson (GKA) rules [37] determine which of the two types of the magnetic ordering is present. As shown in Figure(2.6), the Mn^{3+} ions with electronic configuration $[Ar]3d^4$ have four electrons in the five 3d-orbitals, three of these occupy the t_{2g} orbitals with a core spin of $\frac{3}{2}$. The fourth electron occupies one of the two degenerate e_g orbitals which point along the crystal axes and hence overlap with the O-2p orbitals. The possible interactions are governed by, first Pauli exclusion principle which allows two electrons in the same orbital only if they are antiparallel and, second Hund's rule which favours parallel spins in different orbitals of the same shell. Figure (2.6) shows the three possible interactions in z-direction considering the GKA rules as follows:

- Rule 1: when the two cations have lobes of the magnetic orbitals (i.e. partially populated d-orbitals) pointing towards the same anion p-orbital, the 3d orbitals hybridise with the p-orbitals and hence the overlap is very large. As shown in Figure (2.6) (a), the Mn^{3+} ions along z-direction with one electron in their $3d_{z^2}$ orbitals, virtual hopping of the two O-p_z electrons results in reducing the total energy if the electrons in the t_{2g} orbitals in Mn are antialigned. Therefore, the interaction in this case is strong and the AFM alignment is favourable in order to

Figure 2.6: Three different possible superexchange cases according to Goodenough-Kanamori-Anderson rules in doped manganites, e.g. $LaMnO_3$, where the exchange is strong and antiferromagnetic in (a), weak and ferromagnetic in (b), and (c). The magnetic exchange between the $3d_{z_2}$ orbital of two Mn^{3+} ions via the $2p_z$ orbital of an O^{2-} ion. Adopted from ref [38].

satisfy Pauli exclusion principle. Such type of interactions occur in materials when the cation-anion-cation alignment is 180^0.

- Rule 2: when two cations have an overlap between singly occupied 3d orbitals and empty or doubly occupied orbitals of the same type, the exchange is ferromagnetic, however it is weak as shown in Figure (2.6)(b) for the case of two Mn^{3+} ions where one has an electron in the $3d_{z^2}$ orbital and the second has no electrons in the same orbital. Virtual hopping between O-p_z electrons is possible with reducing the total energy of the system if the t_{2g} electrons are aligned parallel to each other .

- Rule 3: when the magnetic orbitals of the magnetic ions couple to different p-orbitals, the overlap is zero by symmetry. This type occurs when the geometrical alignment of the C-A-C is 90^0, as illustrated in Figure (2.6)(c). In this case, the interaction is also weak and ferromagnetic. In this case, te virtual hopping of one O-p_z and O-p_y electron results in minimising the total energy if the Mn core spins are aligned parallel to each other.

The interaction is a second order process, and the effective Hamiltonian is found by second order perturbation theory as $J \sim \frac{2t^2}{U}$. Thus, the strength of the transition is controlled by a parameter called the hopping integral, t between p and d orbitals which is proportional to the conduction band width and it is of order of 0.1 eV [31]. Additionally, the energy cost of making an excited state is given by the Coulomb energy U which is the onsite 3d Coulomb interaction and it is typically in the range 3-5 eV [31].

2.4.3 Exchange in metals

RKKY interaction

This type of interaction happens in metals when the magnetic moments of the magnetic ions are localised such as for the 4f states in rare earth elements and thus there can be no overlap with neighbouring sites. Consequently, the 4f localised states hybridize with the conduction band (6s, 5d); because of this hybridization, the localised moments spin-polarize the conduction electrons, and this polarisation couples to the neighbouring localised moments at a distance r. Accordingly, the interaction is indirect since it is mediated by the conduction electrons. It is known as RKKY referring to the initials of the surnames of the discoverers, or alternatively called itinerant exchange.

The exchange integral of two localised moments separated by a distance r takes the form:

$$J_{RKKY}(r) \sim \frac{\cos(2k_F r)}{r^3}, \tag{2.27}$$

assuming a spherical Fermi surface of radius k_F. As it can be seen from the definition above, the the interaction is long range and has an oscillatory dependence on r. Consequently, the coupling can be either ferromagnetic or antiferromagnetic depending on the distance r between the localised moments as shown in Figure (2.7). This explains why some rare earth elements are ferromagnetic and others are antiferromagnetic.

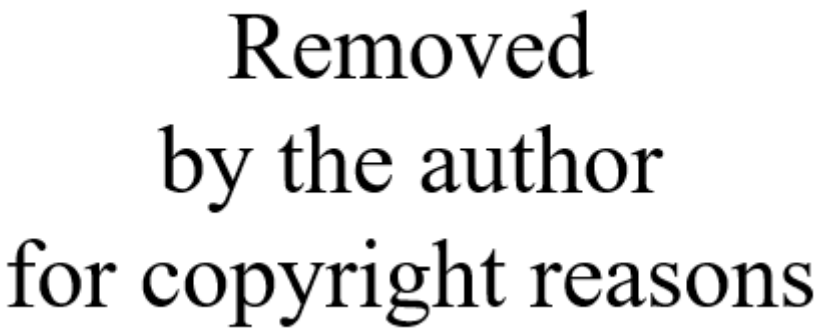

Figure 2.7: The RKKY exchange integral as a function of the distance between localised magnetic moments, r. Adopted from ref [39].

Double exchange interaction

Another indirect interaction that can occur in metals which is proposed by Zener to explain the observed magnetism in perovskite magnetites [40]. It takes place when a mixed-valence configuration exists in the material. It is expected in oxides with two different 3d cation valencies as the coupling is mediated by oxygen in between the transition metal ions. It is observed in doped manganites.

The coupling can be explained with reference to Figure (2.8). For example, in $(La_{1-x}Ba_x)MnO_3$, Mn ions are present in two different valence states; namely $Mn^{3+}(3d^4)$ and $Mn^{4+}(3d^3)$.

In such material, there are two simultaneous electron transfers. One of them from O^{2-} p-orbital to the $Mn^{4+}(3d^3)$, and the other from $Mn^{3+}(3d^4)$ to O^{2-} p-orbital. Consequently, as illustrated in Figure (2.8), the configuration changes from $Mn^{4+}O^{2-}Mn^{3+}$ to $Mn^{3+}O^{2-}Mn^{4+}$ in which both have the same energy resulting in ferromagnetic spin alignment.

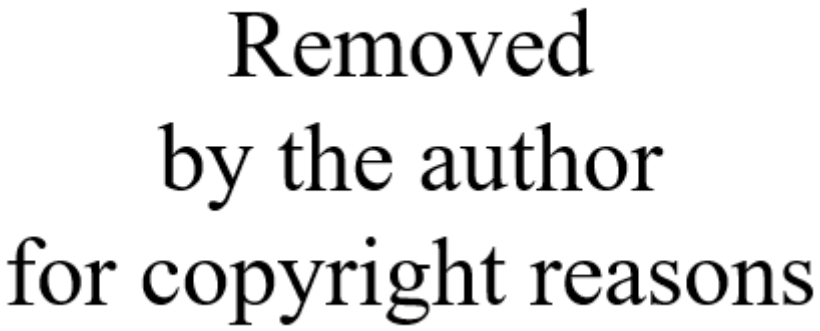

Figure 2.8: Double exchange interaction mechanism in doped manganites, e.g. $(La_{1-x}Ba_x)MnO_3$ where the material has two different valency states, Mn^{3+} and Mn^{4+}. The figure was adopted from [38].

Another example in Fe_3O_4 where there are pairs of iron ions with valencies; $Fe^{3+}(d^5)$ and $Fe^{2+}(d^6)$. The (d^5) configuration is a half-filled shell, and the sixth electron occupies the bottom of a t_{2g} band when the ion is in the octahedral position. The single electron can hop directly from (d^5) core to another. In fact, in such materials, there is usually a competition between superexchange and double exchange. Similar to the superexchange interaction, the double exchange interaction is short range.

2.4.4 Band magnetism (Stoner-Wolfarth)

Nearly all the transition metal elements have non-integral value of magnetic moment per atom. Therefore, such magnetisation can not be interpreted on the basis of localised moments on atoms. Hence, such values of magnetisations are strong evidence of band-ferromagnetism (or alternatively known as the itinerant ferromagnetism) in which the magnetisation is caused by spontaneously split bands. This spontaneously ferromagnetism can be achieved if

$$Ug(\epsilon_F) \geq 1 \tag{2.28}$$

Where U is the exchange Coulomb energy, and g(ϵ_F) is the density of states at the Fermi level .

Figure 2.9: Stoner criterion parameters of different elements, where $N(F_F)$ is the density of state at the Fermi level and I(eV) is the exchnge Colomb energy. Only Fe, Co, and Ni pass the criterion and hence they are spontaneously ferromagnetic. The figure was adopted from [31].

The condition is known as the Stoner criterion and it can be derived by calculating the total energy cost of moving a number of electrons from spin-down for example to spin-up or vice versa and this energy change must stabilize the system, i.e. $\Delta E < 0$. Therefore,

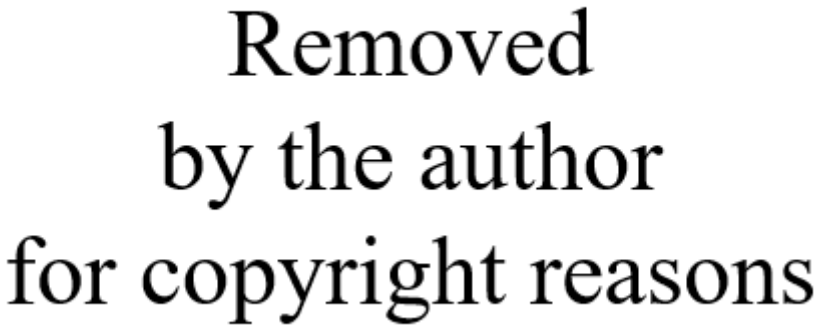

Figure 2.10: Density of states of Fe, Co, Ni and Cu for the majority and minority spins from [41]. The Fermi energy is set to zero.

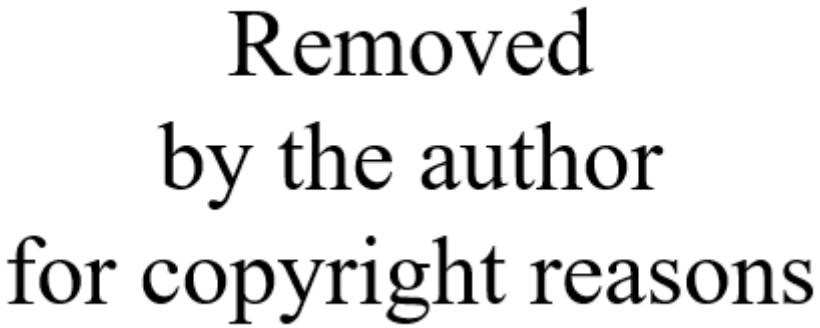

Figure 2.11: An illustrative sketch of a weak and strong ferromagnets, adopted from [31].

narrower bands tends to be more magnetic since the density of the states at the Fermi level scales inversely with the band width.The Stoner criterion is satisfied for Fe, Co and Ni, whereas Pd almost meets the condition as Figure (2.9) illustrates. Consequently, strong ferromagnetism requires strong Coulomb effects, U, and a large density of states at the Fermi level and hence the exchange parameter, U, has to be comparable to the width of the band for spontaneous band splitting to be observed. If the material is ferromagnetic due to the spin-split band, the spin-up and spin-down bands are unbalanced by an energy difference representing the exchange splitting, Δ, in the absence of the magnetic field as

shown in Figure (2.10).

The density of states plots of transition metals, as shown in Figure (2.10), and in metals in general show a highly structured 3d-band superposed on a more delocalised 4s band as illustrated in Figure (2.11). Providing that Stoner criterion is satisfied and if the splitting is sufficient to push the majority, spin up in Figure (2.11), d-subband completely below the Fermi level, the metal is a strong ferromagnet, otherwise it is weak. As Figure (2.10) shows, Fe is a weak ferromagnet, whereas Co and Ni are strong although their magnetic moments are 2.17, 1.71 and 0.58 μ_B, respectively [31].

2.5 Magnetic nanoparticles

2.5.1 Origin of anisotropy

Anisotropy is an important concept in understanding the behaviour of the magnetic material via the hysteresis loop since magnetic anisotropy strongly affects the shape of hysteresis loops and controls the coercivity and remanence. It originates from the fact that when no magnetic field is applied to a given magnetic material, the direction of the magnetisation prefers to point in a certain direction called the easy axis. However, when the magnetic field is switched on, the direction of the magnetisation is pulled towards the field direction as Figure (2.12) demonstrates. Furthermore, by increasing the magnitude of the field, the magnetisation direction becomes closer to the field direction. Crystal anisotropy is a consequence of the spin-orbit coupling. This is a coupling between the spin angular momentum and the orbital motion as it was previously mentioned, see section

2.2.1. When an external field tends to realign the spin of an electron, the orbit of that electron also attempts to be realigned because the two motions are coupled. On the other hand, the orbit is also coupled very strongly to the lattice via the crystal field and hence resists the realignment of the spin axis. Therefore, the energy required to rotate the spin system of a domain away from the easy direction, is the same as the energy just required to overcome the spin-orbit coupling and such energy is referred to as the anisotropy energy,

$$E = K\sin^2\alpha \tag{2.29}$$

where K is the anisotropy constant (J/m^3), E is the anisotropic energy per unit volume, and the angle α is the angle between easy axis and the saturation magnetisation. Values of K varies between less than 1 kJ/m^3 and more than 20 MJ/m^3 [31]. The anisotropy has temperature dependence, and must vanish at Curie temperature if there is no applied field.

Figure 2.12: A schematic description of the easy axis and the direction of the magnetisation, and the magnetic field.

Even though it is known that crystal anisotropy is due principally to the spin-orbit coupling, no further details about the exact relation are available and it is generally impossible for the anisotropy constants to be calculated from first principles. In addition,

there is no relation between the easy or the hard axis of the magnetisation and the way that atoms are arranged in the crystal. In FCC iron, the plane with the highest density of atoms is $< 111 >$, and this represents the hard axis. In Ni, the medium hard axis is $< 110 >$ which is the plane of the greatest atomic packing. However, in FeNi FCC alloys with 25% Fe, the easy axis changes from $< 111 >$ to $< 100 >$. Figure (2.13) shows the magnetisation curves for three different transition elements with the easy, medium, and hard axes are labelled. The crystalline anisotropy energy surfaces are also shown for the same elements in Figure (2.14).

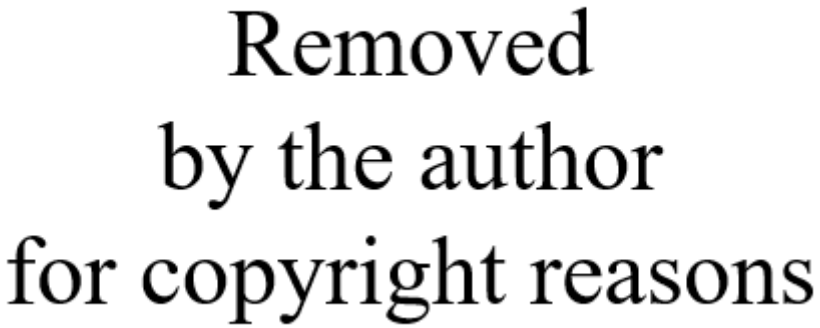

Figure 2.13: The magnetisation of single crystals of iron, nickel, and cobalt (HCP) respectively with the easy and hard axes are labelled. Figure was adopted from ref [30].

The magnitude of the crystal anisotropy generally decreases with temperature more rapidly than magnetisation, and becomes zero at the Curie point. Since the anisotropy is directly connected to the coercivity, the latter decreases very rapidly with temperature till it vanishes with the anisotropy. Conventional expressions for the anisotropy in different symmetries, in spherical polar coordinates (r, θ, ϕ), are: hexagonal;

$$E = K_1 \sin^2\theta + K_2 \sin^4\theta + K_3 \sin^6\theta + K_3^{'} \sin^6\theta \sin 6\phi \tag{2.30}$$

Figure 2.14: 3D first-order crystalline anisotropy energy surfaces, in spherical coordinates, $E_{(\theta,\phi)}$ for Fe, Co(HCP), and Ni. The different shapes of the surfaces are a reflection of the sign of K_1; for $K_1 > 0$, the surface shape is oblate spheroid, and for neagtive K_1 values, the shape is prolate spheroid. There are three easy axes $< 100 >$ in Fe, only one [001] surface in Co, and four $< 111 >$ in Ni. Adopted from [31].

tetragonal;

$$E = K_1 \sin^2\theta + K_2 \sin^4\theta + K_2^{'} \sin^4\theta \cos 4\phi + K_3 \sin^6\theta + K_3^{'} \sin^6\theta \sin 4\phi \qquad (2.31)$$

and cubic;

$$E = K_{1c}(\alpha_1^2\alpha_2^2 + \alpha_2^2\alpha_3^2 + \alpha_3^2\alpha_1^2) + K_{2c}(\alpha_1^2\alpha_2^2\alpha_3^2) \qquad (2.32)$$

The first term in eq(2.30) and (2.31) is second order in $sin\theta$, the weaker terms are fourth and sixth order and they are $\propto \lambda^n$, where λ is the s-o coupling constant, and α_i are the direction cosines of the magnetization. The K_{1c} term in eq(2.33) is equivalent to $K_{1c}(\sin\theta^4 \cos\phi^2 \sin\phi^2 + \cos\theta^2 \sin\theta^2)$.

Shape anisotropy originates from the demagnetizing field. The energy of a sample in its demagnetizing field H_d contributes to the magnetostatic energy, which depends on the direction of magnetization in the sample. Therefore, the energy varies as the shape of the sample varies. For a permanently magnetised body in zero applied field with

magnetization M, the magnetostatic energy is

$$E_{ms} = -\frac{1}{2}\mathbf{H}_d.\mathbf{M} \tag{2.33}$$

Eq.(2.34) can be rewritten in terms of the demagnetisation factor N_d, where $\mathbf{H}_d = N_d.\mathbf{M}$:

$$E_{ms} = \frac{1}{2}N_d M^2(erg/cm^3) \tag{2.34}$$

or

$$E_{ms} = \frac{1}{2}\mu_0 N_d M^2(joule/m^3) \tag{2.35}$$

Figure 2.15: Prolate ellipsoid with a major axis c and a minor axis a and magnetisation $\mathbf{M}$ at an angle θ to c-axis, Adopted from [30].

Now we consider a sample of a prolate ellipsoid shape with a major axis c, and a minor axis a and a magnetisation $\mathbf{M}$ with a direction θ with the c-axis as shown in Figure (2.15). Taking both components of $\mathbf{M}$, the magnetostatic energy in (SI units) can be written as:

$$E_{ms} = \frac{1}{2}\mu_0[N_c(M\cos\theta)^2 + N_a(M\sin\theta)^2] \tag{2.36}$$

Which can be simplified further to:

$$E_{ms} = \frac{1}{2}\mu_0 N_c M^2 + \frac{1}{2}\mu_0(N_a - N_c)M^2\sin\theta^2 \tag{2.37}$$

The first term in eq.(2.38) is constant and the second term has an angle dependence of the same form as the uni-axial crystal anisotropy energy eq.(2.30) and the major axis, c, plays the same role as the easy axis of the crystal, as shown in Figure (2.12), and hence the magnetisation is easy along the c-axis and equally hard along any direction perpendicular to c. Thus, the shape anisotropy constant K_s is given by:

$$K_s = \frac{1}{2}\mu_0(N_a - N_c)M^2 \tag{2.38}$$

If c becomes equal to a, the sample is then spherical and $N_a = N_c$ and hence $K_s = 0$ and no shape anisotropy exhibited.

A third type of the anisotropy is the induced anisotropy. The anistropy can be induced in certain alloys, for example, by annealing in a magnetic field and hence called induced anisotropy. An example of such type is permalloy, $Ni_{80}Fe_{20}$, which is an fcc alloy with the property that $K_1 \simeq 0$. When annealed at $\sim 800K$, a weak anisotropy is induced. In addition, the anistropy can be also induced by strain, and this effect is called magnetostriction. Magnetostriction is a property of ferromagnetic materials which causes them to expand or contract in response to an applied magnetic field. For a previously demagnetized crystal experiences a strain that can be measured as a function of applied field along the principal crystallographic axes, the material will change its dimension when it is magnetized. The fractional change in length $\frac{\Delta l}{l}$ is the strain caused by an applied stress, and to distinguish this from the magnetically induced strain , the latter is given the symbol λ, where $\lambda = \frac{\Delta l}{l}$. The value of λ measued at the saturation magnetisation is called the saturation magnetostriction, λ_s, and whenever the term "magnetostriction" is mentioned, λ_s is meant.

Within a domain, the molecules are aligned so that their dipoles point in the same direction. This causes a north and south pole or oppositely-charged portions on opposite sides of the domain. A material can have any number of domains as long as the number of domains minimizes the internal energy of the structure. The boundaries separating these regions (in bulk materials) are called Bloch walls. Bloch walls are made up of a thin layer of molecules in which their molecular dipoles are gradually rotated to align with their adjacent domains. The orientation of a Bloch wall depends on the directions of the applied magnetic field and the magnetic anisotropy of the crystal structure. When a magnetic field is applied to a ferromagnetic material, the magnetic field applies a force on the material's molecular dipoles which pushes them to align with the field. As the dipoles rotate, a strain is produced in the material, causing it to elongate.

Although the magnetostrictive stain is small in most magnetic materials, the existence of the effect means that an applied mechanical stress can alter the domain structure and create a new source of magnetic anisotropy. These effects can strongly affect the low-field magnetic properties, such as the permeability and the remenance [30].

2.5.2 Coercivity of nanoparticles

High coercivity of fine particles is often required for permanent magnetic applications. The coercivity of the nanoparticles has a well known dependence on their size. Figure (2.16) shows schematically how the size range of the nanoparticle is divided according to their coercivity with the type of each magnetic material corresponding to each range. Starting from zero particle size till a critical size D_p (typically a couple of tens nanometres as Figure (2.17) illustrates) is reached, the coercivity is zero because of the thermal

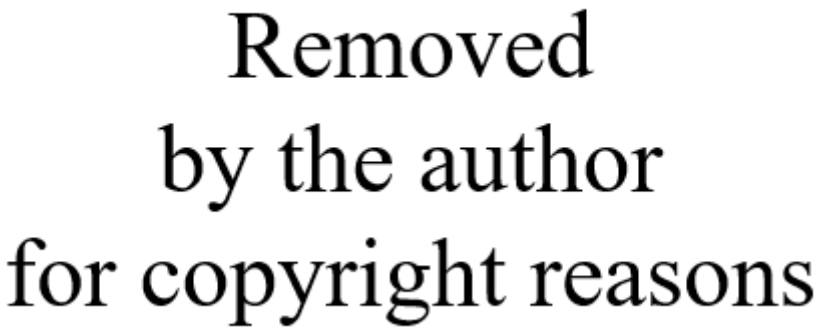

Figure 2.16: Intrinsic coercivity of nanoparticles as a function of the particle diameter. Superparamagnetic region is located between zero size and a critical size D_p, monodomain ferromagnetic behaviour where the particles change their magnetization by spin rotation till D_s where the coercivity is maximum, after which the particles are multi-domain where the magnetization changes by domain wall motion, adopted from [30].

fluctuations at room temperature which can demagnetise any previous saturated magnetisation. Particles with this size range are called superparamagnetic whose behaviour will be discussed in more details in the next subsection. By increasing the particle size until D_s, the coercivity increases until it reaches its maximum at D_s. This is because of the the decrease of the thermal effects with increasing the particle's size when the anisotropy increases. Above the critical diameter D_s, the particle becomes multi-domain and by increasing the size, the coercivity decreases and the magnetisation changes by domain wall motion. Figure (2.17) shows the typical threshold diameters for superparamagnetism; $d_{SP} = D_p$ and the maximum mono-domain size; $d_{cr} = D_s$ for spherical nanoparticles for common magnetic materials based on bulk materials parameters [42].

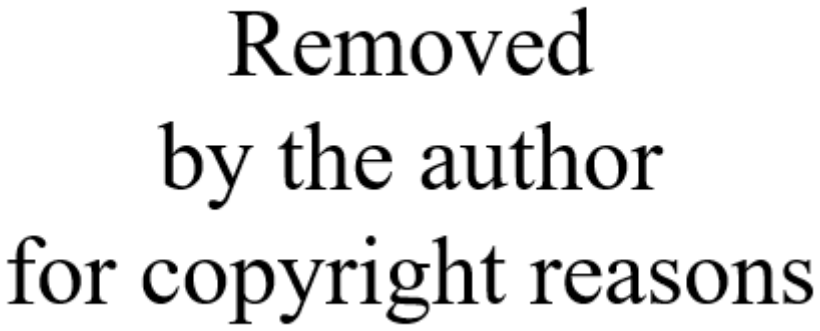

Figure 2.17: Threshold diameters for superparamagnetism (d_{SP}) and maximum mono-domain (d_{cr}) for spherical nanoparticles based on bulk material parameters for common magnetic materials. Figure was adopted from [42]. Note; $d_{SP} = D_p$ and $d_{cr} = D_s$ in Figure(2.15).

2.5.3 Superparamagnetism

As pointed out in the previous section, the magnetic properties of the nanoparticles are mainly size dependant. For uniaxial single-domain particles with anisotropic energy $E = Ksin^2\alpha$ and a particle volume V, the energy barrier that must be overcome so that the particle can flip its magnetisation is KV as demonstrated in Figure (2.18). If the particles become small enough, $d \leq D_p$, hence reducing this energy, thermal fluctuations can overcome the anisotropy forces and spontaneously flip the easy axis of the magnetisation from one to another even if no external field is present as it has been pointed out by Neel *et el.* [43].

In fact, for small enough particles with an applied field H, there is a competition between the magnetic energy which tries to align all the particles' magnetic moments in the direction of the field and the thermal energy which tends to randomise the moments in a very similar situation to paramagnetism. The only main difference between the

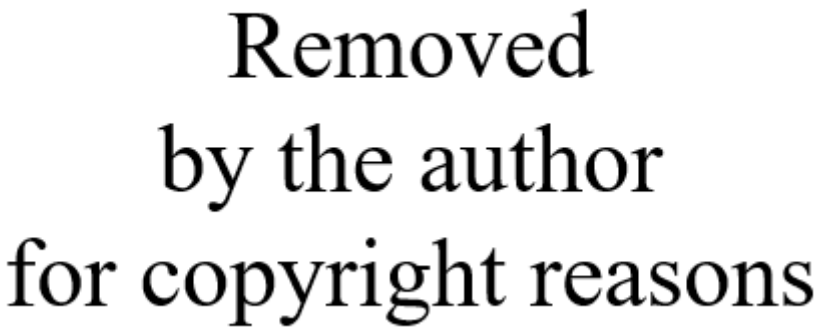

Figure 2.18: The energy (E) of a magnetic nanoparticle as a function of the magnetic moment of orientation relative to the external field direction (H). The energy barrier between the two spin orientations is non-zero even when $H = 0$ when $\Delta E = KV$. The energy is schematically drawn relative to high and low T thermal energies. The figure was cited from [42].

two is that the magnetic moment per atom or ion of a paramagnetic atom/ion is only a few Bohr magnetons, while in a spherical-nanoparticle with a size of a couple of tens of nanometres in diameter, there are thousands of atoms and hence its magnetisation is enormously larger; a couple of thousands of Bohr magnetons. The difference in the saturation magnetisation between paramagnetism, superparamagnetism and ferromagnetism is demonstrated in Figure (2.19). Therefore, in this case, the nanoparticles are classified as superparamagnetic and hence the term superparamagnetism to describe the behaviour of the nanoparticles in such size range with a very high saturation magnetisation and a zero coercivity [44].

Now, in order to visualise the magnetisation curves of the superparamagnetic particles, we will start with the situation when K=0, so each particle has no anisotropy, then the moments of the particles point in random directions, and hence the classical theory of the

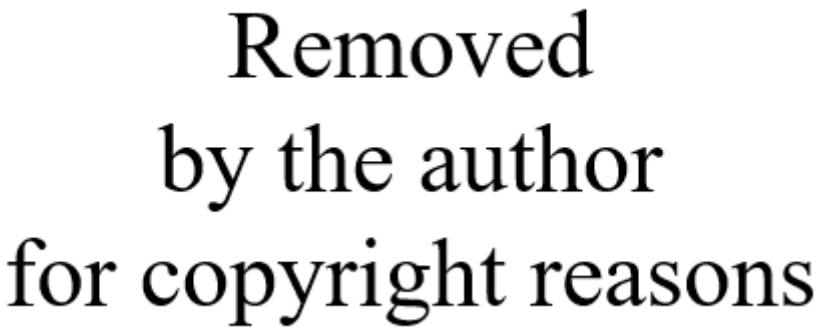

Figure 2.19: Schematic comparison of magnetisation curves of ferromagnetic, paramagnetic and superparamagnetic ($T > T_B$) materials; figure was adopted from ref [40].

paramagnetism is applied. Thus, the magnetisation of the assembly is described by:

$$M = n\mu L(a), \tag{2.39}$$

where n the number of particles per unit volume of the assembly, $\mu(= M_s V)$ is the magnetic moment per particle, where V is the volume of the nanoparticle, $a = \frac{\mu H}{k_B T}$, and $L(a)$ is the Langevin function. Since the magnetic moment of the particle is enormously large, even at small values of the applied field and high temperatures, the saturation of the superparamagnetic particles can be easily achieved comparing to paramagnetism. Whereas in paramagnetic samples, very high field and low temperatures are required to observe saturation as it is clearly shown in Figure (2.19) for the situation of H-field dependence at constant temperature. In the other extreme case, if $K \neq 0$ and the particles are aligned with the easy axis parallel to each other and to the applied field, then the directions of the magnetic moments are quantised, either aligned or anti-aligned with the field. In this case, quantum theory applies where:

$$M = n\mu \tanh a \tag{2.40}$$

A comparison of the two previous magnetic curves is shown in Figure (2.20).

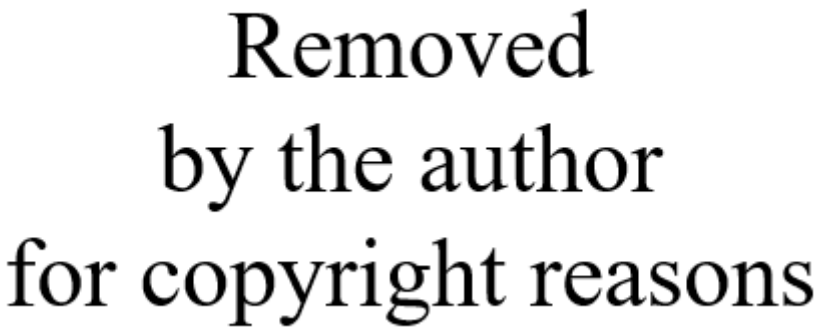

Figure 2.20: Comparison between Langevin, the red line, function which represents the classical description of the magnetisation of the superparamagnetic particles and tanh function, the blue line, which gives the quantum description [45].

For intermediate situation of non aligned particles of non-vanishing anisotropy, neither of the two previous equations will apply. Furthermore, such equations can not describe the usual situation where the particles have different sizes and hence they have different magnetic moments. In spite of that, two main superparamagnetic behaviours are always true. Firstly, magnetisation curves measured at different temperatures overlap when M is plotted as a function of $\frac{H}{T}$. Secondly, there is no hysteresis behaviour with both coercivity and retentivity are zero as shown in Figure (2.19). Furthermore, their size range must be less than D_p as depicted in Figure (2.16).

Blocking temperature

As it was discussed earlier, because of the nanoparticles magnetic anisotropy, the magnetic moment of uni-axial nanoparticles usually has two stable orientations antiparallel to each other, separated by the energy barrier as Figure (2.18) shows. The stable orientations define the nanoparticle's easy axis. Neel- Arrhenius equation gives the mean time

between two possible spin flips as a result of thermal fluctuations at finite temperature,

$$\tau_N = \tau_0 \exp \frac{KV}{k_B T} \tag{2.41}$$

where: τ_N is Neel relaxation time, τ_0 is characteristic length of time of the material called the attempt time or the attempt period; typically it is $10^{-9} - 10^{-10}$ seconds, K is the anisotropic constant, k_B is Boltzmann constant, and T is the temperature. If the magnetisation of single superparamagnetic nanoparticle is measured in a magnetic field where the measurement time is τ_m and $\tau_m \gg \tau_N$, the nanoparticle magnetization will flip several times during the measurement, thus the measured magnetization will average to zero and hence the particles will be in the superparamagnetic state. On the other hand, if $\tau_m \ll \tau_N$, the magnetization will not flip during the measurement, and the particles will be blocked in the initial magnetic state at the beginning of the measurement. Therefore, the magnetic state of the particle depends on the measurement time and a transition between the two magnetic states occurs when $\tau_m = \tau_N$. In practice, the measurement time is usually kept constant but the temperature is varied, so the transition is observed as a function of the temperature. The temperature for which $\tau_m = \tau_N$ is called the blocking temperature and defined as:

$$T_B = \frac{KV}{k_B ln(\frac{\tau_m}{\tau_0})}. \tag{2.42}$$

For typical laboratory measurements, the value of the logarithm in the previous equation is of order of 20–25. Typical magnetisation curves at high and low temperatures compared to T_B is shown in Figure (2.21), where at high temperatures or long measurement time, the sample reaches thermal equilibrium and superparamagnetic curve is measured (a). While if the temperature is low, equilibrium is not reached and the particles are blocked in their initial magnetisation state and hysteresis is observed (b).

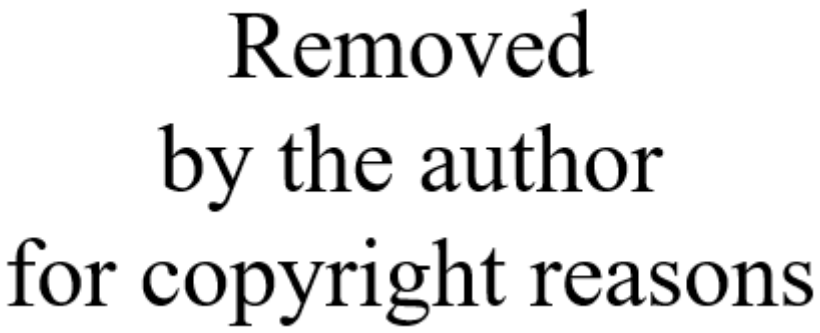

Figure 2.21: Magnetisation curves for (a) superparamagnetic particles for $T > T_B$ with zero coercivity and retentainty, and (b) for blocked nanoparticles, $T < T_B$, with hysteresis is observed. Adopted fro ref [42].

The blocking temperature is measured from the magnetic moment or the susceptibility as a function of temperature with the applied magnetic field is on and off. As a result, two curves are yielded namely; field cooled (FC) curve and zero field cooled curve (ZFC), respectively. In the FC curve, the magnetic moment increases with lowering the temperature. Similarly in ZFC curve, the moment increases when the sample is cooled, however, until a particular temperature is reached and then it decreases. The peak in the ZFC curve occurs at the blocking temperature, T_B which is directly proportional to the size of the particle. Figure (2.22) shows FC/ZFC curves for two different sizes of Co nanoparticles in ZnO samples prepared by PLD [27]. Figure (2.23) demonstrates the difference between Curie temperature and the blocking temperature. Below the blocking temperature, the magnetic moment of the nanoparticles are blocked in their initial magnetic state, whereas when the temperature is higher than T_B, the moments are randomised and the average magnetisation is zero. On the other hand, Curie temperature is a transition between ferromagnetic order of the magnetic moments of the constituting atoms or ions and the paramagnetic state where the thermal fluctuation dominants. In general, the blocking

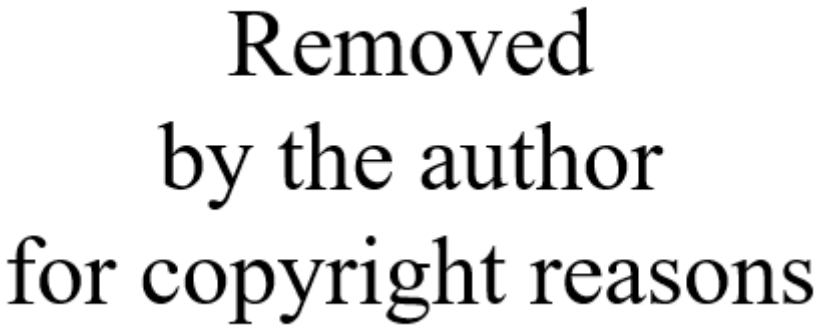

Figure 2.22: FC/ZCF for Co nanoparticles in ZnO samples prepared by PLD measured in 100 Oe for the FC curves. The figure is adopted from [27].

temperature is much less than Curie temperature; $T_B \ll T_C$.

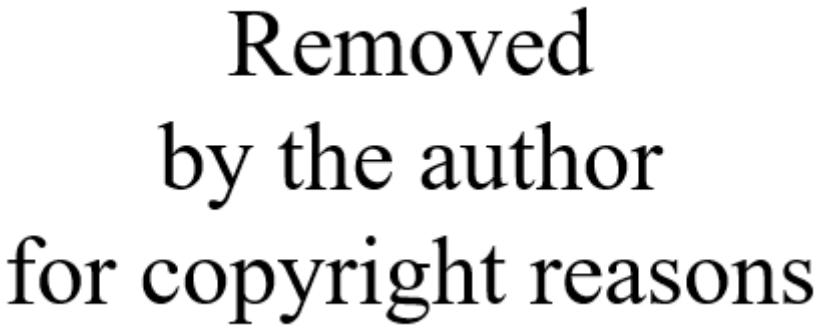

Figure 2.23: Comparison between the Blocking temperature and Curie temperature. For $T < T_B$, the particles are blocked in their initial magnetic state, where for $T > T_B$, the moments of the nanoparticles are randomised by thermal fluctuation. For $T < T_C$, the material has a ferromagnetic order, where as if $T > T_C$ the material is paramagnetic, adopted from [42].

Chapter 3

Modelling of Magnetic Circular Dichroism spectra due to point defects in ZnO

3.1 Introduction

There are different sources of magnetism in transition-metal-doped ZnO, these include metallic nanoparticles and lattice defects. Each source of magnetism has a characteristic magnetic behaviour. The ferromagnetism of the first source has a temperature dependent magnetisation as explained in the previous chapter. The lattice defects can be due to different contributions such as point defects, grain boundaries and surface states. The defect-induced magnetism has approximately a temperature independent ferromagnetism. In our experimental samples, the nanoparticle contribution can be detected by X-ray absorption techniques, and characterised by the negative MCD signal spanning an energy

range between 2- 3 eV and the magnitude of the signal is proportional to the fraction of the metallic clustering in the samples according to Maxwell-Garnet theory [46]. In this chapter, a quantum mechanical derivation of an equation that gives an indication of the sign and the relative magnitude of the MCD signal that may originate from point defects in ZnO is presented. Additionally, some experimental data were modelled and compared using the derived equation.

3.2 Previous Work

The origin of the observed ferromagnetism (FM) in doped oxides is still controversial. It has been found that nonmagnetic semiconductors and insulators become ferromagnetic when doped with just a few percent of transition metal (TM) cations [47–49]. The TM ions have finite moments due to their unpaired spins and the coupling between them is unable to provide any sort of magnetic order if the concentration of the dopants is below the percolation threshold, x_p, which is typically greater than 10% in oxides [50]. Even more surprising is that some of the undoped oxide films or doped with nonmagnetic elements have been observed to be ferromagnetic at room temperature [51, 52]. This manifests the importance of the point defects introduced during the growing process which may be spin polarised. There have been several reports on defect-induced magnetism in magnetic oxides, see for example [53–55]. ZnO has been observed to display room temperature ferromagnetism when undoped or doped with a low percentage of TM ions [53, 54, 56].

3.2.1 Point defects in ZnO

Point defects in ZnO include vacancies; V_O and V_{Zn}, interstitials; Zn_i and O_i, and antisite defects; O_{Zn} and Zn_O [57,58]. Figure (3.1) shows DFT results of calculations of the formation energies in all point defects in ZnO as a function of the Fermi energy and under Zn- and O-rich conditions. The formation of such defects and hence their concentration depends on the preparation conditions. There have been several first-principles studies on such defects [57–59]. They have been found that V_O, Zn_i and Zn_O behave as donors and are energetically favourable in Zn-rich environment in p-type samples. On the other hand, V_{Zn}, O_i and O_{Zn} are reported to be acceptors and have low formation energy in O-rich conditions and n-type ZnO samples. Although both vacancies are deep levels, they have the lowest formation energy among other defects. Furthermore, the antisite defects have the highest formation energy and hence are rarely formed. For interstitial levels, they are both shallow levels, however the Zn atom has smaller radius so expected to have the lower formation energy [59].

Figure 3.1: DFT calculated formation energies of point defects in ZnO as a function of Fermi level in (a) Zn-rich, and (b) O-rich environment, adopted from [57].

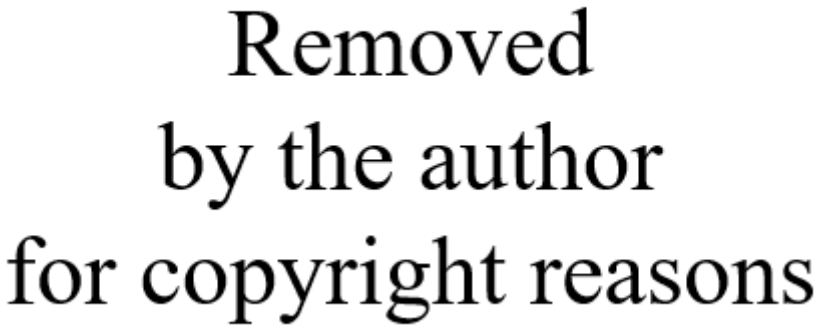

Figure 3.2: Photoluminescence (PL) spectra of oxygen-deficient ZnO films grown on sapphire as a function of reducing oxygen pressure from (a) to (c) [60].

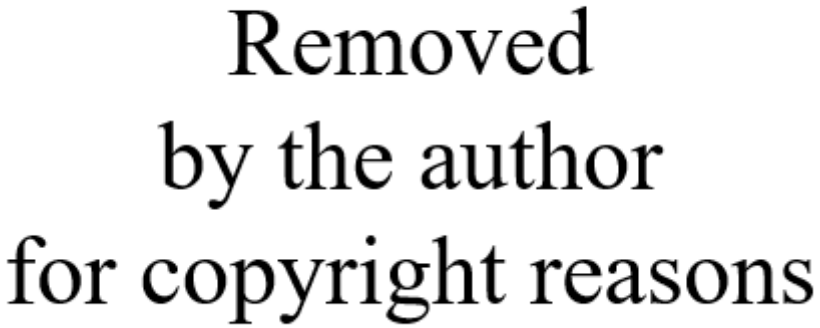

Figure 3.3: Temperature dependent PL spectra of (a) sol-gel and (b) MBE pure ZnO thin films. Inset of (a) shows the room temperature PL data of the Ar-annealed SG ZnO sample in comparison with the as-grown samples [5].

There have been a large number of reports on defect characterisation by Photoluminescence (PL) measurements in ZnO in the literature, see for example [5, 60–67]. All these reports have agreed about the source of the observed peak at the band edge which has been attributed to the exciton recombination and the intensity of this peak has been shown to correlate well with the quality of the prepared samples. The argument has been about the source of the observed deep band emissions, and more specifically the source of the observed green band emission (GBE). Some reports have claimed that the source

of these emissions are transitions involving singly ionised oxygen vacancy states [60–62] in O-deficient ZnO samples as shown in Figure (3.2). However, it has also been claimed that the PL source might be oxygen anti-site defect and proposed to be a deep acceptor level in [63, 64] in contrast to more recent DFT reports [57]. On the other hand, in some other recent reports in O-rich ZnO samples, the source of the green line emission has been claimed to be zinc vacancy deep acceptor states [5, 65, 66]. Xing *et el.* have shown that pure ZnO films prepared by sol-gel technique have stronger ferromagnetism than those prepared by MBE [5]. By measuring the PL spectra of both types of films as shown in Figure (3.3), the ferromagnetism has been attributed to Zn vacancy states which have been assumed to be the source of the observed GBE at energy about 2 eV. More interestingly, the GBE has been proposed to be caused by both vacancy transitions at slightly different energies [67]. It has been claimed that the green band centred at 2.3 eV is due to zinc vacancy complexes, while that observed at a peak 2.47 eV is caused by oxygen vacancy centres.

3.2.2 MCD Spectra

The Magnetic Circular Dichroism (MCD) signal at frequency ω is defined as the difference in absorption of right and left circularly polarised light,$\alpha_{\pm}$ in a film of thickness L in the presence of a magnetic field parallel to the direction of light propagation, in Faraday geometry where linearly polarized light travels parallel to a magnetic field and the linearly polarized light can be regarded as a superposition of circular components [68].

$$\frac{MCD}{L} \sim \frac{\alpha_+ - \alpha_-}{2} \tag{3.1}$$

The technique has been shown to be very powerful in detecting spin polarised gap states in non-magnetic materials [69] and magnetic thin films [24,28,56,70–74]. The MCD spectra can be measured as a function of temperature for a chosen magnetic field. They can also be measured as a function of the applied magnetic field at a particular energy and a constant temperature. All these types of spectra may give an indication of the sources of the magnetism in thin oxide films as will be shown later. Since MCD measures the difference in the absorption intensity between right and left circularly polarised light at a particular energy, the identification of the gap states may be estimated with the aid of the Photoluminescence measurements (PL). Great care must be taken when comparing the peak energies of the two spectra because the transitions are not exactly the same in both cases. The energy of the PL peak transition between two energy levels is lower than the corresponding energy for the absorption due to Franck-Condon effect. However, the Photoluminescence cannot always be measured due to the presence of any magnetic dopants that may quench the spectra [75].

There are two origins of the measured signals. The first occurs when there is a difference in the energy of the two transitions, RCP and LCP, but they have the same transition intensity due to their equal, or nearly equal, orbital population. The second type of signals is observed mainly due to the difference in the orbital population with a tiny difference in the transition energy leading to different intensities at approximately the same energy. The first type is referred to as the 'diamagnetic' signal and has a dispersive line shape; whereas the second signal is referred to as the 'paramagnetic' signal and results in an absorption line shape. It is worth mentioning that the observed paramagnetic signal does not indicate that the whole sample is paramagnetic if the bulk diamagnetism

dominates the measurements. Furthermore, to observe the diamagnetic MCD signal, a high resolution apparatus, higher than Zeeman energy, is required. Such MCD signals are too small to be accessed in our experiments and have been referred to as silent transitions [69]. Optical transitions occur between magnetically quantized electronic states with $\delta m_s = 0$ and $\delta m_l = \pm 1$ in Faraday geometry. Therefore, MCD signal can only be observed if the spin and orbital states are mixed by spin-orbit coupling. It is worth mentioning that the two sources might be present at the same time.

MCD in ZnO thin films

MCD has been used very effectively to identify the sources of the observed magnetism in thin films. There were several magneto-optical investigations in ZnO in the literature; see for example [24, 27, 28, 56, 69–74]. The MCD spectra in these reports show different types of signals being negative or positive at different energies. In the following subsection, a brief review of these different types of signals is presented.

Negative MCD spectra

It has been found that Co-doped films prepared by PLD with a low oxygen pressure in the PLD chamber usually contain metallic Co nanoparticles and they lead to an enhancement of the observed ferromagnetism and the anisotropy [24, 27]. Such magnetic source has been found to have a characteristic negative MCD signal between 2-3 eV as shown in Figure (3.4)(a), and (3.5)(a). Negative Signals can also arise at the band edge, $E_g \sim 3.4$ eV, due to shallow-donor impurity-band or spin-split valence band as shown in Figure (3.5) (b). Feng et *al* have shown that these two magnetic sources can be further coupled to each other by adding extra carriers via Al doping and this has been shown to enhance the observed ferromagnetism [27]. The MCD signal for the latter case is shown in Figure

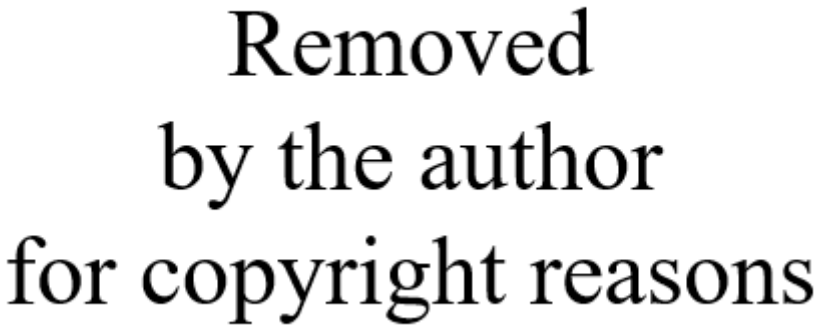

Figure 3.4: MCD spectra for (a) $Zn_{0.95}Co_{0.5}O$ films prepared at base pressure with metallic Co (sample A), CoO (sample D), and Co_3O_4 (sample E) as a a target precursor, and (b) films prepared with Co metal as a target precursor at base pressure, 10 mTorr, and 100 mTorr for samples A, B, and C, respectively, adopted from [24].

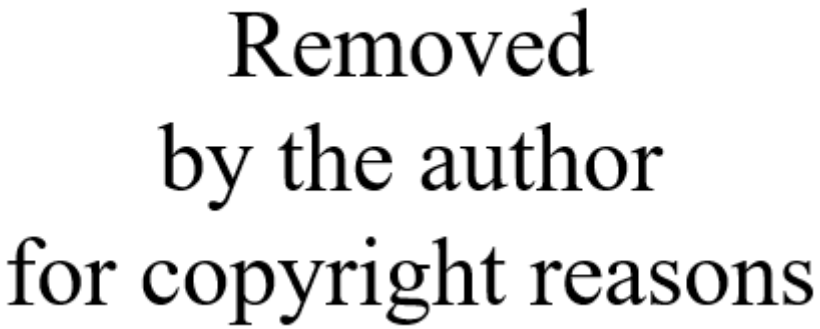

Figure 3.5: RT MCD spectra in sample A with 7 at % (a), sample B with undetectable amount (b) of metallic Cobalt in Co-doped ZnO samples, and in sample C with 2 at % of the doping percentage of Co in metallic state with 0.6 % of Al [27].

(3.5)(c).

Positive MCD spectra

Positive MCD signals have been detected for gap states for films prepared using metallic Co as a target precursor in high oxygen pressure [24] as shown in Figure (3.4)(b). The positive signal across the band gap has been also detected in pure [69] and in As-implanted

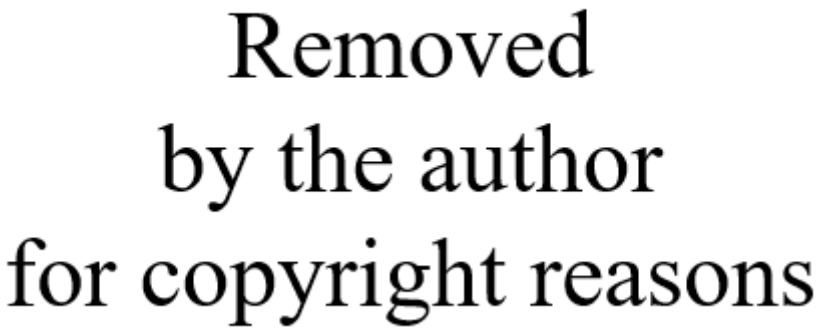

Figure 3.6: Room temperature MCD spectra of As-implanted films with increasing As concentration from undoped to sample 3 [72].

ZnO films prepared by MBE [72]. In the As-implanted films, the magnetisation has been found to increase with increasing the As concentration. The ion-implantation technique is known to produce lattice disorder, and Raman spectra have shown that this disorder increases with increasing the concentration. In these samples, the observed ferromagnetism was almost temperature independent which is typical for defect-induced ferromagnetism and hence was attributed to Zn vacancy states as has been found in sol-gel pure ZnO films [5] and the observed MCD spectra spanning an energy range of 2-3 eV for the As-implanted ZnO MBE films, shown in Figure (3.6), were also assigned to transitions involving such defects.

3.3 Results and Discussion

3.3.1 Calculation of MCD from localised defects

Pure ZnO has a full valence band and an empty conduction band. However, normally, there are some defect energy levels introduced in the band gap. A defect state with a

wavefunction, ϕ_0^0, at an energy E_0 from the valence band edge, has $\langle l^z \rangle = 0$ because either it is an s-state [57,58] or the angular momentum is quenched. ZnO is grown with the c-axis perpendicular to the plane of the film when grown on c-cut sapphire (0001)-substrate [76]. This is also the direction of the applied magnetic field. The MCD signal is non-zero when there is a difference in absorption between the right and left circularly polarised light, α_+ and α_-,respectively for $\delta m_l = \pm 1$, respectively for Faraday geometry. Hence the MCD signal is proportional to the orbital angular momentum along z-axis, $\langle l^z \rangle$.

Following Pryce *et al.* [77], we treat the spin-orbit coupling and Zeeman term as perturbations:

$$H^{'} = \lambda L^z S^z + \mu_B B^z (L^z + 2S^z) \tag{3.2}$$

Where λ is the spin-orbit coupling constant, B^z is the applied magnetic field along z-direction, and S^z is the spin component along the magnetic field. Thus, the first order perturbed ground state of the system is:

$$\phi_0^1 = \phi_0^0 - \sum_{n \neq 0} (\mu_B B^z + \lambda S^z) \frac{< n|L^z|0 >}{E_n - E_0} \phi_n^0 - \sum_{n \neq 0} 2\mu_B B^z \frac{< n|S^z|0 >}{E_n - E_0} \phi_n^0 \tag{3.3}$$

Where;

$$H_0 \phi_0^0 = E_0 \phi_0^0,$$

and

$$H_0 \phi_n^0 = E_n \phi_n^0 \tag{3.4}$$

Where ϕ_0^0, and $\phi_{\rm n}^0$ are the unperturbed ground, and excited states respectively. Since $\mu_B B^z$ for 1 T equals 10^{-4} eV, and hence is much smaller than all values of λ considered as shown in table 3.1, the third term can be safely neglected in eq(3.3). Therefore, the expectation of L_z in this basis is given by:

$$< \phi_0^1|L^z|\phi_0^1 >=< 0|L^z|0 > -2(\lambda S^z + \mu_B B^z)\Lambda_{zz} + {\rm O}^2(\lambda {\rm S}^{\rm z} + \mu_{\rm B}{\rm B}^{\rm z}) \tag{3.5}$$

Where;

$$\Lambda_{zz} = \sum_{n\neq 0} \frac{|< n|L^z|0 >|^2}{E_n - E_0} \tag{3.6}$$

The first term in eq.(3.5) vanishes, and the third term can be neglected since it is very small compared to the second term, and hence

$$< \phi_0^1|L^z|\phi_0^1 >= -2(\lambda S^z + \mu_B B^z)\Lambda_{zz} \tag{3.7}$$

The last derived equation, eq(3.7), is proportional to the strength of the intensity of the MCD signal.

MCD for defect states with spin

Magnetism in undoped ZnO is caused by defects, such as Zn vacancies [5] and grain boundaries that have unpaired electrons [6]. Such defects usually have spin value of S=1/2 or S=1 as for zinc vacancy doublet and triplet states [57, 58]. In this case, the electronic paramagnetic resonance (EPR) measurements on undoped ZnO may be used to find the

deviation of the g-value of the ground state of the defect from the free spin value [78]; where

$$\Delta g_{zz} = -2\lambda\Lambda_{zz} \tag{3.8}$$

Hence we find a relationship between the MCD and the measured values of Δg;

$$MCD \sim \Delta g_{zz}(S^z + \frac{\mu_B B^z}{\lambda}) \tag{3.9}$$

Equation (3.9) is a central result in this investigation and gives a useful interpretation for the MCD signal. It shows that the signal may arise from two sources: either from spin polarisation or from the polarisation of the orbits due to the applied magnetic field. The equation may be applied for both paramagnetic and ferromagnetic samples.

For paramagnetic samples, when $\frac{\mu_B B}{k_B T} \ll 1$, the average of the spin is $\langle S^z \rangle = \frac{\mu_B B^z}{k_B T}$; so that the paramagnetic MCD has the form:

$$MCD \sim \frac{\mu_B B^z}{k_B}\Delta g_{zz}(\frac{1}{T} + \frac{1}{T_\lambda}) \tag{3.10}$$

Where $T_\lambda = \frac{\lambda}{k_B}$. Therefore, if the MCD signal measured at room temperature is dominated by paramagnetic spin-polarised states, i.e.$T_\lambda \gg 300$K, the signal is expected to reflect the paramagnetic temperature dependence, i.e. MCD $\sim \frac{1}{T}$ in a constant applied magnetic field. However, if the effect of the spin-orbit coupling is small, $T_\lambda \ll 300$K, the second term dominates at room temperature and hence the MCD signal is expected to be

temperature independent till low T where $T \sim T_\lambda$. The MCD is expected to vary almost linearly with the variation of the applied magnetic field at constant temperature in both previous cases at low values of the applied field.

For ferromagnetic samples, however: $\langle S^z \rangle \propto$ magnetisation. For small values of the applied magnetic field such those used in our experiments where the Zeeman energy is much smaller than the s-o coupling constant, the first term dominates in equation (3.9). In this case, the magnitude of the MCD spectrum is predicted to follow the magnetic behaviour and follow a hysteresis loop with the change of the magnetic field as it has been shown in [74].

MCD for singlet defect states

Equation (3.7) shows that even for a nonmagnetic state, there is still a non-vanishing term, $MCD \sim \mu_B B \Lambda_{zz}$ which results in a small contribution in the magnetisation and the MCD at the small value of the applied magnetic field. This contribution arises from the well-known Van-Vleck temperature independent paramagnetism. This is the only contribution that can occur for both oxygen vacancies and zinc interstitials that are neutral or doubly ionised since they have been shown to have closed shell configurations [58, 59]. Taking into account the definition of Λ_{zz}, equation (3.6), the signal due to this contribution may be significant only if the applied magnetic field is large and the energy separation between the ground and the excited states is small.

Relative strength of MCD signal

The values of Δg for the three most common defects in ZnO, presented in Table (3.1), show that the strongest signal is expected from the shallow level of the interstitial zinc, Zn_i^+. In fact, the MCD signal per defect is expected to be an order of magnitude stronger than that caused by the oxygen vacancy, V_O^+ and two orders of magnitude more intense than the zinc vacancy, V_{Zn}^- signal. Therefore, the strength of the MCD signal varies from one defect to another depending on the value of the deviation of Landé g-factor from the free spin value as long as the spin-orbit coupling constant is much larger than Zeeman energy. This latter condition is satisfied for all defects considered here, as it can be seen from Table (3.1) where Zeeman energy, in our experiments, is of order of 10^{-4}eV and hence the second term, in equation (3.9), is ≤ 0.006 and much smaller than the first term which has a maximum value of $\frac{1}{2}$ for doublets. The values of the spin-orbit constant for

defect	Δg	λ **(eV)**	T_λ **(K)**
Oxygen Vacancy	-0.0078^a	0.016^b	194
Zinc interstitials	-0.0418^a	0.1084^c	1257
Zinc Vacancy	0.0001^a	0.5306^b	6157

Table 3.1: The reported values of Δg, λ, and equivalent temperature T_λ for the three most common point defects in ZnO, adapted from *a* [78], *b* [79] and *c* [80].

V_O^+ was adopted from Bartram *et al* [79] and converted to the relevant units and that for V_{Zn}^- was estimated from the same reference by averaging the s-o coupling constants of the vacancies of the surrounding elements of Zn in the periodic table, namely: Ca^{2+} and

Sr^{2+} since SrO and CaO are well studied divalent oxide compounds and the spin-orbit coupling constants are reported for the divalent cation vacancies, and that for Zn_i^+ was adopted from [80].

3.3.2 Comparison to experimental results

According to the sign of Δg of the point defects in Table (3.1), negative values for the MCD is expected from unpaired electrons in defect states due to oxygen vacancies and zinc interstitials. A negative MCD signal can also arise from other sources as it has been mentioned earlier. We have chosen to consider only samples that show a positive MCD in order to fit our theory because this arises uniquely from zinc vacancies.

Experimental results for films with positive MCD

Table (3.2) shows a list of films grown by PLD technique, grown by Dr Wala Dizayee, and a pure ZnO film made by MBE, grown by Dr Minju Ying [69]. The samples are listed according to their magnetisation at room temperature. Most of the films exhibit an approximately temperature independent ferromagnetism, $\frac{M_s(300K)}{M_s(5K)} > 0.85$ which is a clear signature of a defect-induced magnetism. In order to investigate the source of the observed ferromagnetism, the room temperature MCD spectra in a magnetic field of 1.8 T were measured and such spectra are presented in Figure (3.7). One can see that the films either have no metallic Co inclusion or have a tiny amount which might not be responsible for the observed ferromagnetism. It has also been experimentally proved that substitutional Co is paramagnetic and hence it is not the source of the observed magnetism [1]. The MCD spectra show positive signals spanning an energy range between 2 - 3 eV. The

positive signals, as we believe, are due to transitions involving Zn vacancy states since they are deep levels and may cause transitions in the observed energy range and their MCD signal is expected to be positive due to the positive Δg value. This argument is further supported by similar reports in the literature for Zn vacancy and other cation vacancies being the source of the observed ferromagnetism [5, 81–83] and by grain boundary model proposed by Gupta et al which suggests that the negatively charged Zn vacancy states are distributed across the grain boundaries to balance the positively charged oxygen vacancy states which are spread through the grains [84]. Photoluminescence measurements (PL) on Zn deficient sol-gel ZnO films performed by Xing et *al* showed broad Gaussian spectra peaked at nearly 2 eV with FWHM of about 0.7 eV assigned to donor-acceptor-pair (DAP) emission associated with Zn vacancies and the observed ferromagnetism has been showed to be caused by such deep-acceptor levels [5].

Sample	Target composition	Thickness (nm)	$H_c(5K)(Oe)$	$H_c(300K)(Oe)$	$M_s(5K)(\frac{emu}{cm^3})$	$M_s(300K)(\frac{emu}{cm^3})$	$\frac{M_s(300K)}{M_s(5K)}$
A	ZnO	400	0	0	0	0	/
B	$Zn_{0.95}Co_{0.05}O$	300	88.2	52.9	7.6	6.7	0.88
C	$Zn_{0.95}Co_{0.05}O$	100	185	86.2	12.5	9.1	0.73
D	$Zn_{0.95}Co_{0.05}O$	60	117.3	79.4	18.53	16.57	0.9
E	$Zn_{0.94}Co_{0.05}Al_{0.01}O$	59.5	152.7	103	18.41	17.62	0.96
F	$Zn_{0.69}Co_{0.30}Al_{0.01}O$	166	73.9	25.8	24.24	23.11	0.95

Table 3.2: ZnO target composition, thickness and magnetisation measurements of (A) MBE O-polar film [69], (B - F) PLD films ordered according to their magnetisation. The measurements have been done by colleagues Dr Wala Dizayee and Dr Minju Ying.

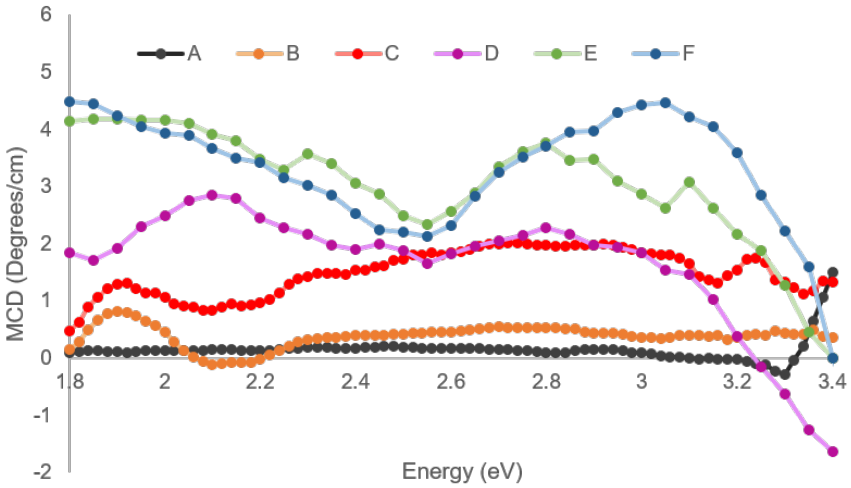

Figure 3.7: Room temperature MCD spectra in a magnetic field of 1 T of series of samples as a function of photon energy; meaurements were taken by Dr Wala Dizayee at the University of Sheffield.

Modelling the MCD signal

As we can see from Table (3.2) and Figure (3.7), the magnitude of the positive MCD signal increases with increasing the value of the saturation magnetisation for all samples. The signals for sample B and D, however, have lower MCD intensities than expected from their magnetisation. To see this relation more explicitly, we consider the average value of the MCD signal between 2- 3 eV. The estimated average signal was then plotted against the saturation magnetisation in Figure (3.8), and such a relation was found to be approximately linear. This indicates that the magnetism in these samples is caused primarily by zinc vacancy states which we believe are the origin of the positive MCD signal observed. Moreover, the magnetisation of the films, as shown in Table (3.2), are almost temperature independent being typical for defect-induced ferromagnetism [55]. On the other hand, if there are more than one type of defects contributing to the observed ferromagnetism, the expected strength of the MCD of one type should be lower than that expected from the total number causing the magnetism as it is the case for the

MCD intensity of our samples B and D. It appears that there are additional defects that contribute to the magnetism and produce a different MCD signals from the observed positive ones. These defects may be zinc interstitials for sample D which are shallow donors always donate their electrons to the conduction band as reported by Janotti et *al* [57] and thus produce a negative band edge signal at $E \sim 3.4$ eV as dominates other samples [73]. For sample B, the defects may be oxygen vacancy states which are deep donors and we showed that they are expected to produce a negative signal. The energy of the transition from the valence band to the deep donor level of oxygen vacancy is comparable to the transition energy from the conduction band to deep acceptor level of zinc vacancy and hence such signal is expected to reduce the observed MCD spectrum. This argument is supported with the fact that this sample is prepared at a lower oxygen pressure than the corresponding sample, C.

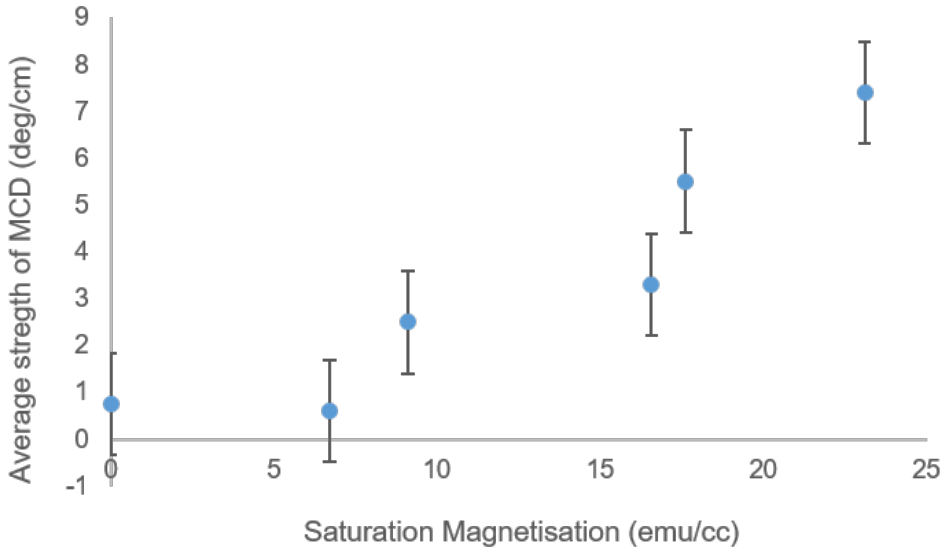

Figure 3.8: Average strength of MCD spectra as a function of saturation magnetisation of Co doped ZnO films.

From the theoretical calculation in section 3.1, we conclude that the MCD strength varies from one defect to another according to their values of Δg_{zz} and Λ_{zz}, where the latter depends on their spectra of their excited states. Moreover, we saw from experimental data that for a particular defect type, the strength of the MCD is proportional to the saturation magnetisation and also to the number density of the defects present in the film. From the classical definition of the MCD, we know that the MCD intensity per unit length is determined by the difference in absorption of left and right polarised light. Therefore, the MCD intensity also depends on the absorption which is given by

$$\alpha(\omega) = N_1 \sigma_a(\omega) \tag{3.11}$$

Where $\alpha(\omega)$ is the absorption coefficient and ω is the frequency, N_1 is the number of the defects in the ground state, and $\sigma_a(\omega)$ is the absorption cross section which gives the absorption probability as a function of the frequency. This is a further confirmation of the N-dependence of the strength of the MCD.

In these films, the magnetisation satisfies $M_s \leq 25$ emu cm^{-3} and if this is all due to Zn vacancies it would imply that $N_d \leq 1.25 \times 10^{21}$cm^{-3} which is large but not unreasonable because it suggests that a fraction of about 3% of the Zn are missing from Zn sites and this can be acceptable if we adopt the idea of defect doping at the grain boundaries proposed by Gupta *et al* [84]. The number of defects at room temperature was estimated from the corresponding values of the saturation magnetisation considering each zinc vacancy associated with a magnetic moment of 1.7 μ_B as reported in the literature [5, 85, 86].

3.4 Summary and conclusion

An MCD equation was derived based on perturbation theory where the spin-orbit coupling and the Zeeman interaction are treated as perturbations. The equation predicts that the magnitude of the spectrum should follow the behaviour of the magnetism in the sample as it has been assured in previous work [56, 74]. It also differentiates between two different sources of magnetism; spin polarised gap states and a small contribution for zero spin states arises from the polarisation of the orbits due to the applied magnetic field. It also shows clearly that the relative strength is governed completely by the deviation of the g-factor of the defect from the free spin value as long as the spin-orbit coupling is much larger than the Zeeman energy. The latter condition is satisfied for all defects considered in our study under the experimental conditions used in our laboratory. From the measured values of Δg, the strongest signal expected from a single paramagnetic centre in ZnO is caused by the often ionised interstitial zinc. The oxygen vacancy and zinc vacancy states have relatively weaker signal by a factor of 10 and 100, respectively. Moreover, the signal is expected to be negative for the donor levels of zinc interstitials and oxygen vacancy, while positive for the zinc vacancy acceptor levels, and this gives an opportunity to distinguish between these sources, especially if the preparation conditions were taken into consideration.

Our experimental MCD data show positive signals between 2 and 3 eV being typical for deep defect states, which we believe the Zn vacancy states. The intensity of the signal increases linearly with increasing the magnetisation of the films which means that the magnetism is predominantly caused by the same defects causing the positive MCD; Zn vacancy defects. Such defects have been reported to be the origin of the observed

magnetism in un-doped ZnO [5] and Co-doped samples with stronger ferromagnetism [53, 71]. Moreover, the saturation magnetisation values of these films with the positive MCD have a very weak temperature dependence as has been found for defect induced magnetism [55]. For particular type of defects, the main factor that determines the intensity, as we found, is the number density of that defect type. Therefore, the MCD intensity is directly proportional to Δg and the number density of the defects. However, if the ferromagnetism is caused by more than one type of defects, the total strength of the MCD is hence the sum of the strengths of all signals which may or may not be distinguishable from the spectra because of possible cancellation.

Chapter 4

Basics of density functional theory

4.1 Introduction

Modelling a system with $\sim 10^{23}$ interacting electrons and nuclei is extremely challenging. The task has been greatly simplified by Density Functional Theory (DFT) that was introduced in two original papers in the 1960's: Hohenberg-Kohn (1964) [87] and Kohn-Sham (1965) [88]. Nowadays, it has become the most important technique in material modelling studies. Therefore, the Nobel Prize in Chemistry 1998 was assigned to Walter Kohn for his great efforts towards developing such a theory. Figure (4.1) shows the number of the publications of DFT between 1974 and 2015. Understanding the basics of the Density Functional Theory (DFT) is a very important step towards its application to the system of interest. This chapter introduces the basic principles of the theory and its applicability to solids using plane-waves and explains the background theory of our methodology used for the rest of the thesis. The information in this chapter was written based on references; [90–92].

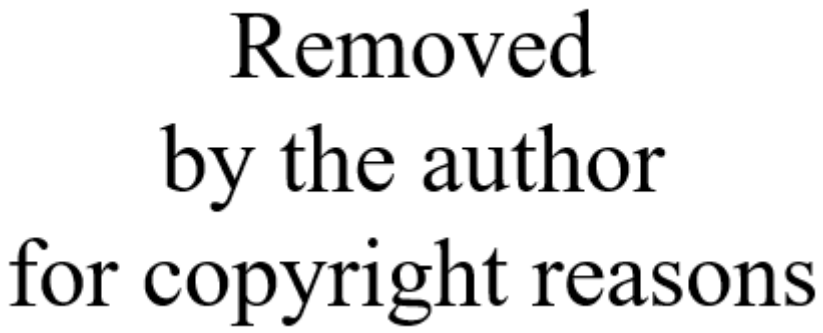

Figure 4.1: DFT publication between 1964 and 2015, adopted from [89].

4.2 Schrödinger equation of the many-body problem

The Schrödinger equation for many-body systems contains many terms; kinetic energy terms of the electrons and nuclei, the electrons-nuclei term, the electrons-electrons term, and the nuclei-nuclei term. For a few grams of a material, there are typically 10^{23} nuclei and 10^{24} electrons. Therefore the equation is impossible to be solved even numerically without approximations.

4.3 Born-Oppenheimer approximation

This approximation simplifies the problem of the complicated many-body equation. It exploits the fact that nuclei are substantially heavier than electrons and hence they are much slower. In addition, their wavefunctions are very localised in space, and hence electrons react instantly to the nuclear motion. Therefore, if the nuclei are treated as fixed in space "i.e. frozen", the quantum efforts will be focused only on electrons. What is more, it removes the time-dependence from describing the problem. Thus, this ap-

proximation changes the time dependent equation of the electrons and the nuclei into a time-independent equation that only involves electrons.

4.4 The Hohenberg-Kohn theorems

The whole theory originated from the two theorems of Hohenberg and Kohn and the derivations of a set of equations by Kohn and his postdoc Sham. In this section, the basic two theorems that make up the entire field will be discussed. The theorems provide a formalism for any system of interacting particles in an external potential $V_{ext}(\mathbf{r})$, including any choice of the number of electrons and the positions of the fixed nuclei, the Hamiltonian can be written as

$$H = -\frac{\hbar^2}{2m_e}\sum_i \nabla_i^2 + \sum_i V_{ext}(\mathbf{r}_i) + \frac{1}{2}\sum_{i\neq j}\frac{e^2}{|\mathbf{r}_i - \mathbf{r}_j|} \tag{4.1}$$

Therefore, by solving the problem for only electrons, the constant term of nuclei-nuclei interaction can be added easily later.

4.4.1 Theorem I

It states that "For any system of interacting particles in an external potential $V_{ext}(\mathbf{r})$, the potential $V_{ext}(\mathbf{r})$ is determined uniquely, except for a constant, by the ground state particle density $n_0(\mathbf{r})$" [92]. Since the Hamiltonian is completely determined by the ground state density $n_0(\mathbf{r})$, except for a constant energy shift, the many-body wavefunctions are determined and thus all ground state properties of the system once the ground state density is known. Moreover, the great advantage of this pioneering theorem is the reduction

of the dimensionality of the problem from being 3N- dimensional using the wavefunction description into only a 3-dimensional problem by exploiting the electronic density.

4.4.2 Theorem II

Even though the first theorem states that there is a unique ground state density, it did not give the recipe of how to find such a density. The second theorem, however, fills the gap and gives such a recipe. It states that "For any particular $V_{ext}(\mathbf{r})$, the exact ground state energy of the system is the global minimum value of this functional, and the density $n(\mathbf{r})$ that minimizes the functional is the exact ground state density $n_0(\mathbf{r})$" [92]. This is nothing but the variational principle applied to the ground state. This means that for any trial density, which satisfies the necessary boundary conditions and which is associated with some external potential $V_{ext}(\mathbf{r})$, the energy obtained from the energy functional represents an upper bound to the true ground state energy E_0. Therefore, E_0 results if and only if the exact ground state density is inserted. Figure (4.2) shows a schematic representation of the theorems as described here.

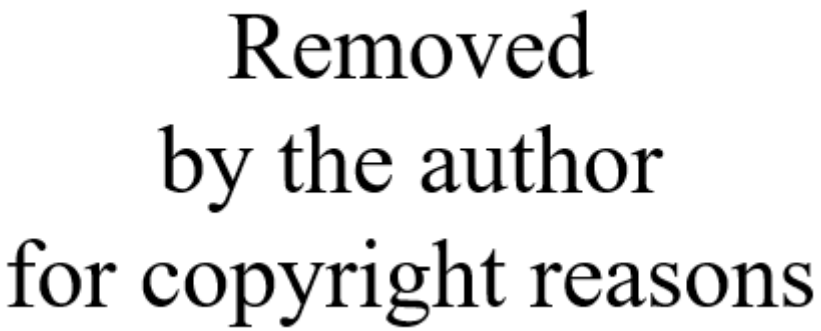

Figure 4.2: A schematic representation of Hohenberg-Kohn theorem, adopted from [92].

4.5 Kohn-Sham equations

DFT approach would still not be feasible without Kohn-Sham ansatz which changes the interacting many-particles problem into many non-interacting quasi-particles which makes it possible to solve. Kohn-Sham formalism assumes that the ground state density of the original interacting system is the same as the chosen non-interacting system. This yields many independent-quasi-particle equations which can be numerically soluble with all the difficult unknown many-body terms included into the exchange-correlation functional, (which will be defined in the following section), of the density as shown in the following equation in the plane wave basis:

$$H_{eff}(\mathbf{r})\psi_i(\mathbf{r}) = [-\frac{\hbar^2}{2m_e}\nabla^2 + V_{eff}(\mathbf{r})]\psi_i(\mathbf{r}) = \epsilon_i\psi_i(\mathbf{r}) \tag{4.2}$$

Therefore, the degree of the accuracy of solving the non-interacting-particle equations to find the ground state density and energy depends on the approximations in exchange-correlation functional. In fact, the Kohn-Sham approach has resulted in very applicable approximations that made first principles calculations possible in predicting electronic structure of the condensed matter materials and large molecules. Figure (4.3) shows a schematic example of the Kohn-Sham DFT computational loop.

4.6 The exchange-correlation (XC) functionals

The aim of DFT calculations is to solve the Schrödinger equation for many body systems along with the ground state density and energy. It is extremely difficult however to do so even numerically because of the complication of the many-body problem. The results

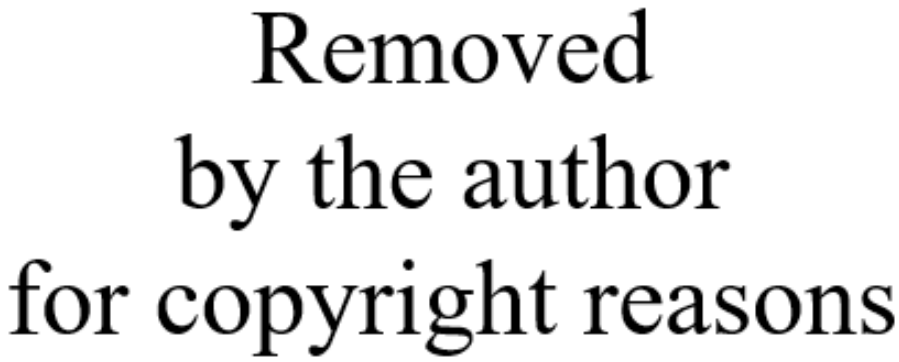

Figure 4.3: DFT algorithm loop, adopted from First Principles Materials Modelling course material by Prof Matt Probert.

from Hohenberg, Kohn and Sham have simplified the problem by finding an approach of obtaining the ground state energy by minimising the energy of the energy functional, and this, as it has been shown earlier, can be accomplished by solving a set of single quasi-particle equations self-consistently. There is only one approximation lies in the heart of such formalism which is incorporated in the exchange-correlation functional and the exact form of the functional whose existence is guaranteed by Hohenberg-Kohn theorem is not yet known. However, there are some very good approximations and their use depends on the type of the system studied and the purpose of the calculation. The exchange-correlation functional is known to include all the missing terms when making the mapping between the interacting and the non-interacting systems. electrons are Fermions and hence obey Pauli exclusion principle. If the coordinates of two identical particles are exchaged then total wavefunction will be antisymmetric and this gives rise to the exchange energy as it has been discussed in section 2.4. Electronic correlation is more difficult to define, however, it can be defined as the interaction between electrons in the electronic structure of a quantum system. The correlation energy is usually defined as difference between

exact many-body quatum-mechanical non-relativistic energy and Hartree-Fock answer. The exchange-correltion energy can be written as:

$$E_{XC} = \frac{1}{2} \int \int n(r) \frac{n_{xc}(r, r^{'})}{|r - r^{'}|} dr dr^{'} \tag{4.3}$$

where n_{xc} is the Coulomb energy of an electron at r interacting with its XC hole at $r^{'}$ and the XC hole is the displaced charge around an electron. The XC hole obeys the sum role; $\int n_{xc}(r, r^{'}) dr^{'} = -1$, which follows from Pauli exclusion principle. However, the shape of the hole is not known.

As emphasized earlier, the Kohn-Sham approach was vital towards developing the theory. The importance of the ansatz is two fold: first, it yields a set of controllable independent-particle equations that made solving the many-interacting particles problem a reality. Second, by separating the kinetic and the potential terms of the independent particle, the remaining exchange-correlation term can be fairly approximated by local or semi-local functionals of the electronic density. DFT would be formally exact if the exact form of the exchange-correlation functional, whose existence is guaranteed by Hohenberg-Kohn theorem, was known. Nevertheless, there are very good approximations that have been developed and proved their efficiency in real calculations. In this section, some of the local approximations as well as some approaches to treat the strongly-correlated systems correctly are discussed in detail.

4.6.1 The local density approximation LDA

LDA was historically the first functional to be used in DFT [93]. In fact, the main idea has been mentioned in Kohn and Sham's seminal paper [88]. They indicated that solids

can be treated as a homogeneous electron gas in which the effects of the exchange and correlation are local in character. Furthermore, they proposed constructing the functional in which the XC energy is an integral over all space with the XC energy density at each point considered to be the same as in a homogeneous electron gas with that density [88].

$$E_{XC}^{LDA} = \int d^3 r n(\mathbf{r}) E_{XC}^{hom}(n(\mathbf{r})) \tag{4.4}$$

Where $E_{XC}^{hom}(n(\mathbf{r}))$ is the XC energy density of a uniform gas of a density n(r). The exchange contribution was first written by Dirac [94], and the correlation contribution has been calculated and accurately parametrised [95]. Therefore, it is expected to work well for solids close to homogeneous electron gas limit (i.e nearly-free electron metals) and badly for inhomogeneous cases. However, LDA proved to work well in both cases. One important reason for such success is that the XC hole obeys all the sum rules since it is the exact hole for some Hamiltonian, even if it is not the correct Hamiltonian. Because of the great success that LDA made, more ideas for constructing improved functionals have been stimulated and developed.

4.6.2 Generalized-gradient approximations GGAs

The success of LDA has led to constructing improved functionals that give better results in some cases; namely the Generalized-gradient approximations (GGAs). Beyond including the density in the integration, GGAs include a functional of the magnitude of the gradient of the density at each point in space. Such approximation has been suggested by Kohn and Sham in their original paper and implemented by Herman *et al.* [96] and others. This leads to an energy functional that depends on both the density and its gradient but retains the analytic properties of the exchange correlation hole inherent in

the LDA. Thus, the approximation is semi-local and hence is still quick to be calculated.

$$E_{XC}^{GGA} = \int d^3r n(\mathbf{r}) E_{XC}^{GGA}(n(\mathbf{r}), \nabla n(\mathbf{r})) \tag{4.5}$$

Where it is parameterized from QMC calculations of HEG and cosine perturbation. Unlike LDA, in GGA there are different ways of parametrising the same set of data. Hence there are many used forms of GGAs. The most three widely used flavours are Becke (B88) [97], Perdew and Wang (PW91) [95], and Perdew, Burke, and Ernzerhof (PBE) [98]. GGAs include more physical information about the system than LDA, hence, it is usually thought that GGAs are better; which is not always true. In principle, more functionals can be constructed by adding other pieces of physical information. In fact, there is a functional ladder of adding extra information and not necessarily with increasing accuracy.

4.6.3 Orbital-dependent functionals

Even though the previous developed functionals proved their efficiency in calculating many properties in many materials, they failed in describing classes of materials in which the electrons are localised and strongly interacting. Examples of such materials are the transition metal oxides and rare earth elements and compounds. Therefore, several methods have been developed to expand the functional to include these effects and hence better describe these materials. Two of these methods are self-interaction-correction (SIC) and LDA + U.

SIC method involves using the approximate local functionals and adding "self-interaction-corrections" to aim to correct for the unphysical self-interaction in local functionals for the exchange and correlation. The interaction of an electron with itself in the Hartree

term is cancelled in the exact treatment of the exchange as in Hartee-Fock formalism.

The expression LDA+U refers to methods that involve utilizing the local functionals LDA-or GGA-type as well as using an extra orbital-dependent interaction term [99, 100]. The extra term is applied only for highly localized orbitals such as d and f orbitals and it is of the same form as the U interaction term in Hubbard models [101]. The effect of such a term is to shift the localised orbitals relative to the other orbitals, which attempts to correct for the obvious errors in LDA or GGA calculations as a result of the self-interaction in the local functionals. For example, most transition metal monoxides are wide-band gap antiferromagnetic insulators [102, 103], however, they are predicted to be either ferromagnetic metals such as FeO and CoO or small gap semiconductors such as MnO and NiO by LDA calculations [104]. Figure (4.4) shows a comparison between the calculated band structure of FeO with and without Hubbard U correction. It shows that the calculations yield a metal with $U = 0$ which is not experimentally correct. Adding Hubbard U term corrects for the calculated error by shifting the d orbital up. The "U" parameter is often taken from "constrained density functional" calculations so that the theories do not contain adjustable parameters or easily set as an empirical fit to obtain the correctly experimental behaviour. Nevertheless, adding the localised term as an empirical fit usually gives qualitative results, see for example [105].

Since each form of the functional will give different results for a particular configuration of atoms, it is important for any DFT calculation to report the functional used.

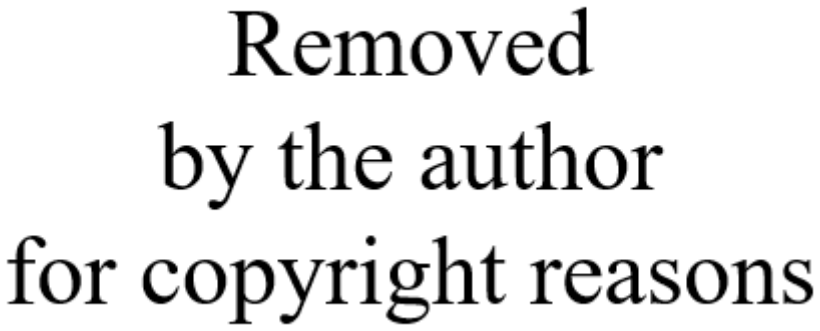

Figure 4.4: GGA(PBE) (top) and DFT+U (bottom) calculations of the band structure with spin up of FeO. Energies are relative to the valence band maximum [106].

4.7 Plane Wave DFT

So far, we showed that Hohenberg, Kohn, and Sham have simplified the problem of the many body Schrödinger equation from being N interacting particles problem into a set of N independent particle problems. However, the problem is still numerically expensive because of the infinitely large number of the electrons in real solids. However, because solids repeat themselves in a periodic pattern, periodicity can be exploited.

4.7.1 Bloch's Theorem

Bloch's theorem states that the electronic wavefunction of electrons moving in a perfectly periodic potential can be written as a product of a periodic part $u_k(\mathbf{r})$ which has the same periodicity as the potential and arbitrary phase factor $\exp i\mathbf{k}.\mathbf{r}$:

$$\psi_k(\mathbf{r}) = u_k(\mathbf{r}) \exp i\mathbf{k}.\mathbf{r}. \tag{4.6}$$

Therefore, by exploiting Bloch's theorem, the problem can only be simplified further to solve Kohn-Sham equations in a single unit cell where the number of electrons has

greatly reduced ($N \sim 10^2$) although in fact an infinite number of electrons is simulated. Furthermore, the supercell approach can be utilized to study non-periodic systems e.g. molecules, surfaces, interfaces, grain boundaries, etc. The symmetry in antiferromagnetic materials is broken, and hence the smallest supercell that should be studied must include the interacting pair. An example of this is the study of formation of the AFM CoO at the ZnO interface in which a pair of Co ions shoud be included to study the interaction being either antiferromagnetic or ferromagnetic.

4.7.2 Reciprocal space sampling

As it has been shown in the previous section, the electronic wavefunction can be written as a product of a periodic part $u_k(\mathbf{r})$ which has the same periodicity as the potential and arbitrary phase factor $\exp i\mathbf{k}.\mathbf{r}$. Thus, the electronic wavefunction in neighbouring unit cells varies by the complex phase factor $\exp i\mathbf{k}.\mathbf{r}$. Hence, in constructing the electronic density, we need to integrate over all possible values of $\mathbf{k}$;

$$n(\mathbf{r}) = \int |\psi_k(\mathbf{r})|^2 d^3\mathbf{k} \simeq \sum_k |\psi_k(\mathbf{r})|^2. \tag{4.7}$$

Since most of the calculations reduces to evaluating an integral of the form $g = \frac{V_{cell}}{(2\pi)^3} \int_{BZ} g(\mathbf{k}) d\mathbf{k}$, the integral is conveniently performed within the first Brillouin zone and the number of the k-points chosen for a particular system depends on the size of the zone for this system. For large systems in real space, a small number of k-points is needed and vice versa. Furthermore, the sampling is performed according to some developed methods. Most DFT packages offer the option of setting k-points based on Monkhorst and Pack (M-P) 1976 method which is the most widely used [107, 108]. For supercells that have the same length in each lattice vector direction (i.e. symmetric), it is natural to choose the same

number of k-points in each direction. If L k-points is chosen in each direction, the usual notation of the M-P grid is $L \times L \times L$. Of course, using higher number of k-points than L improve the quality of the calculation. Since the integral over k-points is infinite, the number of points that gives a relatively qualitative results needs to be determined. This is achieved by performing the convergence test of the ground state energy of the system with respect of the number of k-points used. Therefore, this requires repeating the same calculation for different number of k-points until the energy is well converged as shown in Figure (4.5). Moreover, in perfect solids, there are many symmetry operations within

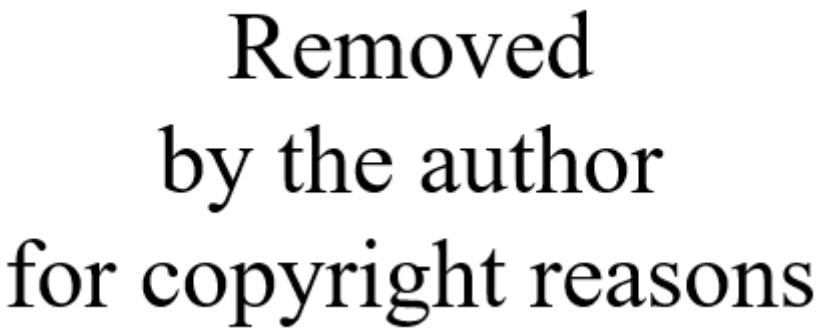

Figure 4.5: An example of k-points convergence test, adopted from First Principles Materials Modelling course material by Prof Matt Probert.

the Brillouin zone. These symmetries lead to a further reduction in the number of k-points needed since the calculation can be performed on the smallest region possible, the irreducible Brillouin zone (IBZ) that can be extended without approximations to fill the entire BZ using symmetry. Therefore, symmetry reduces the numerical effort required to evaluate integral in reciprocal space.

However, not all properties obey the variational principle and hence they are difficult to converge. Magnetic properties are one of these as shown in Figure(4.6) for the magnetic

interaction energies of the interacting Co dopant ions in ZnO as a function of kpoints-sampling and for three different cutoff energies which indicates that qualitatively incorrect magnetic behaviuor often occurs for lower values of k-points and cutoff energies (which will be discussed in section (4.7.3). Similarly rigorous convergence parameters have been shown to be required for accurate calculations for Co-doped TiO_2 [109].

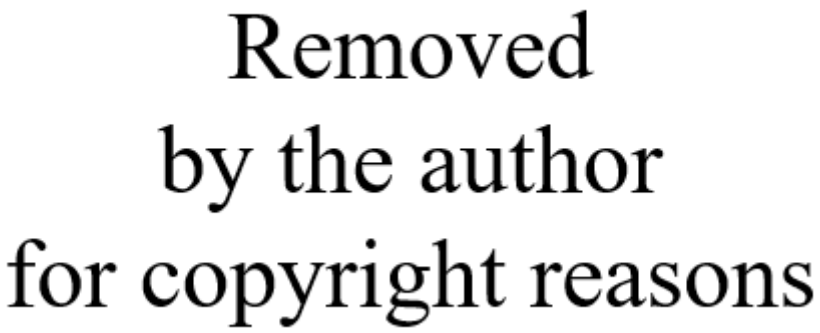

Figure 4.6: Plot of E(AFM)-E(FM) for $Zn_{0.875}Co_{0.125}O$ as a function of the k-point grid and for three different plane-wave energy cutoffs [32]

.

Problems with metals

The previous discussion on the k-points sampling gives the standard grid that is usually used in integration when constructing the electronic density. However, the integration over k-points in reciprocal space does not always run smoothly since not all the functions are continuous and may be integrated easily. An example of such discontinuous functions appears when dealing with metals since a metal can be defined as a material with a Brillouin zone with two distinct regions with occupied and unoccupied electronic states. In terms of calculations, the functions which are integrated change discontinuously from

non-zero to zero at the Fermi level. Therefore, if no special care is taken in calculating such integrals, a very large number of k-points is needed to capture the discontinuity at the Fermi level in order to obtain a well-converged answer.

Metals are important materials and hence there are some approaches that have been developed to overcome this issue. One of the tricks used in metals is to force the function being integrated to be continuous by smearing out the discontinuity. There are various schemes of smearing such as the simple Fermi-Dirac function, Gaussian, and other methods. A common smearing method was developed by Methfessel and Paxton [110].

Another well known method to overcome the discontinuity problem of metals is the tetrahedron method. The idea is to use the discrete set of k-points to define a set of tetrahedra in k-space and to define the function of interest at every point in a tetrahedron using interpolation. The simplest form is the linear interpolation which can be utilized within each tetrahedron. After the interpolation is accomplished, the resulted function will have a simple form at all points in k-space and the integration can then be calculated using the whole space and not just the previous discrete points. The most common method which is widely used nowadays is developed by P.E.Blo¨chl *et al.* [111].

4.7.3 Energy cut-offs

As it was shown earlier, the solution of the Schrödinger equation with a periodic system (i.e. supercell) has the form in equation (4.6) where $u_k(\mathbf{r})$ is periodic with the same periodicity of the supercell. This periodic part can be expanded in terms of known basis functions. The obvious choice of a periodic system is the 3-dimensional sine and cosine

functions; i.e. a special set of plane waves:

$$u_k(\mathbf{r}) = \sum_{\mathbf{G}} c_{\mathbf{G}} \exp i\mathbf{G}.\mathbf{r} \tag{4.8}$$

Where the summation is over all possible values of $\mathbf{G}$; the reciprocal lattice vectors and $c_{\mathbf{Gk}}$ are unknown complex coefficients.

By combining equations (4.6) and (4.8), the wavefunction can be written as

$$\psi_k(\mathbf{r}) = \sum_{\mathbf{G}} c_{\mathbf{G+k}} \exp i(\mathbf{G+k}).\mathbf{r}. \tag{4.9}$$

Equation (4.8) shows that evaluating the wavefunction even at a single k-point requires an infinite sum over all possible values of G, with the smallest value corresponds to the largest wavelength in real space, and this is not numerically practical. Therefore, the summation must be truncated at some value of $\mathbf{G}_{max}$. Fortunately, this can be achieved at specific values for each element without affecting the quality of the calculation too much since in practice as $\mathbf{G}$ gets larger, the complex coefficients $c_{\mathbf{G+k}}$ become smaller. The wavefunction in equation (4.8) represents solutions of Schrödinger equation with energies:

$$E = \frac{\hbar^2}{2m}|\mathbf{k+G}|^2, \tag{4.10}$$

and solutions with low energy are physically important. In practice, the truncation parameter is defined in terms of energy rather than $\mathbf{G}$:

$$E_{cut} = \frac{\hbar^2}{2m}(\mathbf{G}_{max} + k)^2. \tag{4.11}$$

Hence, E_{cut} is another important parameter that must be reported in DFT calculations similar to k-points sampling. However, such a parameter is easier than k-points sampling to be defined as most packages will apply sensible default values if no value is inserted. As

for k-points sampling, the value of this parameter changes with the type of the element and the quality of the calculation. Therefore, convergence test with respect to E_{cut} should be achieved to ensure high quality calculations. For supercells with different type of elements, the largest default value of the cutoff energy among all elements is applied for the system by default. However, for energy difference calculations, the highest value must be adopted for all elements separately to avoid any systematic errors introduced.

4.7.4 Pseudopotentials (PPs)

In the previous section, it was mentioned that large wavelength oscillations in real space correspond to fewer plane waves needed in the calculations and hence modelling it is numerically less expensive. However, the situation is not always ideal like this. There are some situations where small oscillations in real space need to be computed which is computationally expensive. An example of these oscillations is those of the wavefunctions of the tightly bound core electrons as shown in Figure (4.7) for sodium atom. Therefore, these states are numerically expensive. However, their contribution towards the bonding and other material properties is negligible. Rather, material properties are dominated by the less tightly bound valence states. Therefore, it has been thought about if there is any methods that can approximate the properties of the core electrons in such way to reduce the number of plane waves in calculations. The most common approach is to use pseudopotentials.

In the pseudopotential approach, the core electrons are frozen with the nucleus to make a pseudo-ion. As a result, the valence electrons feel a weaker effective potential in the core region and hence their wavefunctions are smoother and nodeless as shown

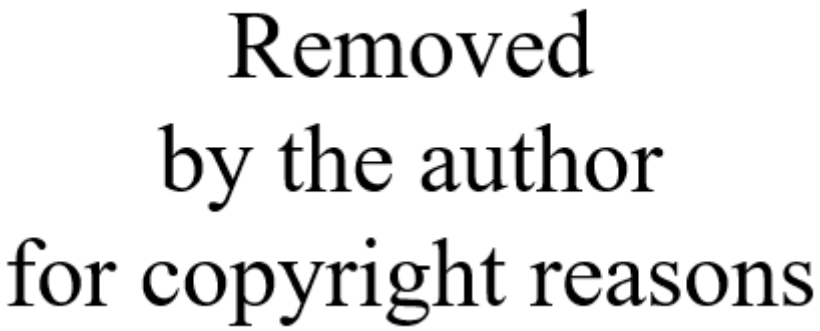

Figure 4.7: The radial probability of electronic states of sodium atom, adopted from First Principles Materials Modelling course material by Prof Matt Probert.

in Figure (4.8). Therefore, the pseudopotential approach presents two-folded advantages in terms of calculation. Firstly, the number of Kohn-Sham equations is reduced due to the reduction in the number of electrons entering the computation. Secondly, since the valence electrons have smoother wavefunctions (i.e.less oscillating), fewer plane waves are needed per electronic state. Therefore, the pseudopotential method has great advantages in simplifying the computations.

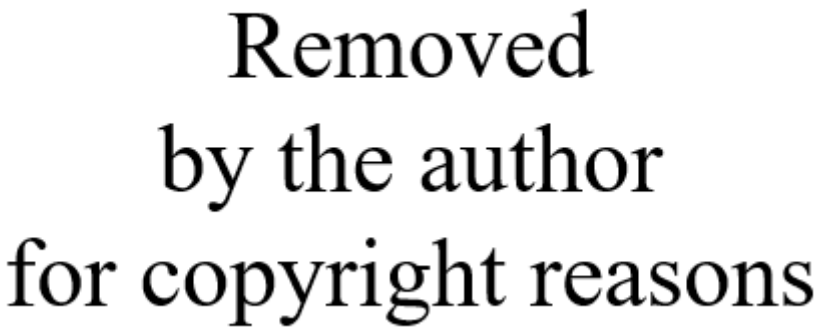

Figure 4.8: The radial probability of electronic states of sodium atom showing the difference of the valence state in Coulomb potential and the pseudopotential, adopted from First Principles Materials Modelling course material by Prof Matt Probert.

Since the properties of the core electrons are fixed in all subsequent calculations, this approach is called "frozen core" approximations. There are other methods in the literature that do not include this approximation and hence called "all electrons" calculations and are less widely used. The term "all electrons" might be a bit misleading since even in the PP approach, all electrons are included; however, the core electrons enter the calculation via the PP. A pseudopotential is constructed for an isolated atom for a particular element, however, it can be used safely when the atom is placed in a different chemical environment without further change. This is a very important property of the pseudopotential which is referred to as the transferability of the pseudopotential.

The PP of a particular element includes the minimum cutoff energy that should be used in the computations. The ones that require high cutoff values are referred to as hard, while those that require low values are known as soft. The latter are computationally preferred since they are more efficient. The most widely used method in constructing PP is based on the work performed by Vanderbilt [112]; these are the ultrasoft PP (USPPs) and they require very lower cutoff values compared to other methods.

4.7.5 Geometry Optimisation

So far, the basic principles and assumptions of DFT were explained in detail. In reality, all these could be applied for fixed atomic coordinates. Therefore, the optimum atomic configuration, i.e. with the lowest ground state energy, must be identified by the user to obtain reasonable results. A numerical procedure with various methods has been developed to achieve this as a pre-requisite of any further calculations and such a procedure is called geometry optimisation. The basic principles of such a procedure can be found

in any DFT package documentations. In this section, there are some important general issues which shall be discussed in details because of their practical importance.

Classically, the force is determined by the differentiating the potential energy with respect to atomic positions. Quantum mechanically, however, it is the expectation value of the total energy which is differentiated instead. For a position-independent basis set, the differentiation turns out to be evaluated only for the Hamiltonian. Therefore, in Kohn-Sham Hamitonian, the electron-ion (the pseudopotential), and the ion-ion Coulomb interaction terms are all potentials that contribute towards the force. The electrons adjust instantly to the position of ions when changing atomic configuration, and as a result a multi-dimensional potential energy surface is yielded for which the global minimum is required. There are various optimisation methods used in different packages such as the steepest descent, damped molecular dynamics, conjugate gradients and BFGS which are all used in CASTEP package which was used for the work presented in this thesis. All these methods, however, can get stuck in a local minimum and this problem is a developing topic of active research nowadays.

The total energy of a system, E is a function that gives the energy of the atomistic system in terms of its atomic positions. Denoting the atomic positions of the system being composed of N atoms by R_i where i = 1, ...,N, the energy function has the following form:

$$E = E(R_i, ..., R_N) \tag{4.12}$$

The position of the j-th atom R_j is a vector with the three components (X_i, Y_i , Z_i). Since the electrons are responsible for the interactions of atoms in condensed matter systems

one has to solve in principle the electronic Schrodinger equation to obtain E. The solution of the many-electron Schrodinger equation gives several sets of corresponding eigenvalues E_i and eigenvectors Ψ_i:

$$H\Psi_i = E_i\Psi_i \tag{4.13}$$

The energies E_i of each set depend on the positions of the atoms since the Hamiltonian is parametrized by the atomic positions. The various functions $E_i(R1, ..., R_N)i$ are called Born-Oppenheimer surfaces. The ground state Born-Oppenheimer surface E_0 is called Potential Energy Surface (PES) as shown in Figure (4.9). Thus the task for optimisation is to find the atomic configuration that gives the lowest energy which means finding the global minimum on the potential energy surfcae.

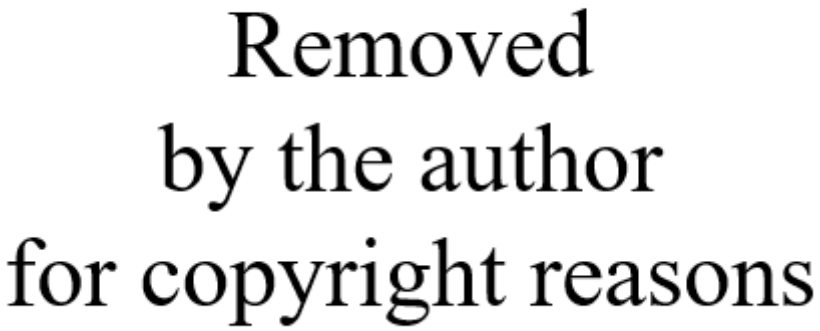

Figure 4.9: Landmark points of the potential energy surface; minima and saddle points. The in-plane axes (x,y) refer to the bond length and the perpendicular axis (z) refers to the energy values.

The geometry optimisation can be done in different ways and constraints. One of these is the variable cell optimisation. This type of relaxation is usually performed for bulk solids to find out the optimum lattice constants. The details of the calculations depend on the

DFT package being used, however, they are all involving varying the supercell volume until determining the lowest energy configuration. Such type of relaxation is usually done as an initial step of optimising a bulk structure to obtain the optimum lattice parameters and for further surface and interface investigations.

Unlike the previous type of optimisation, sometimes it is essential to keep the shape and volume of the supercell fixed and let the atomic coordinates relax inside the fixed volume. This type is called fixed-cell optimisation and it is usually useful in interface studies. Furthermore, there are some other types of calculations where it is convenient to optimise some atomic positions while keeping the others in the system fixed at their initial positions. This type of relaxation is referred to as constrained optimisation and it is useful for calculations involving solid surfaces. Optimisation problems that require some constrains are much more numerically challenging than the unconstrained ones.

4.8 Electronic structure and magnetic properties

There are large number of physical properties where the details of the electronic structure are vital in the material. Two important properties are the electronic structure which determines the type of the material being a metal, semiconductor or an insulator and the magnetic properties of the material. Sections 8.1 and 8.2 are allocated for the discussion of the first property, whereas section 8.3 is devoted for discussing magnetic properties and how they are characterised in DFT calculations.

4.8.1 Band structure

As shown in section 4.7.1, according to Bloch's theorem, the solutions to the Schrödinger equation for periodic systems, are quasi-periodic, however, the electronic density has the same periodicity as the potential. The periodic part of the wavefunction can be expanded in the basis of plane waves as illustrated by equation (4.7) where $\mathbf{G}$ is the reciprocal lattice vector defined by $\mathbf{G}.\mathbf{L} = 2\pi m$ and m is an integer number. Thus, adding or subtracting $\mathbf{G}$ from $\mathbf{k}$ does not affect any physical properties. Therefore, the system is also periodic in the reciprocal space. Given all that, the behaviour of the system in the reciprocal-space unit cell is all what is needed to be studied to know how the system behaves elsewhere. It is conventional to centre the reciprocal-space unit cell around Gamma point; $\mathbf{G} = 0$, and such unit cell is referred to as the first Brillouin zone. The way the energy of the states varies with $\mathbf{k}$ across the Brillouin zone is called the band structure. To understand calculated band structures of materials, two different extreme limits will be considered in the following.

Very localised electrons

As we know, the Hamiltonian is composed of two terms; kinetic and potential:

$$H = V + KE \tag{4.14}$$

If an electron is confined in a very strong potential, i.e $V \ggg KE$, the kinetic energy term in the Hamiltonian can be neglected. Therefore, the energy of the system is :

$$\begin{aligned} E(\mathbf{k}) &= \int \psi^*(\mathbf{r}) V(\mathbf{r}) \psi(\mathbf{r}) d^3\mathbf{r} \\ &= \int V(\mathbf{r}) |\psi(\mathbf{r})|^2 d^3\mathbf{r} \\ &= \int V(\mathbf{r}) |u(\mathbf{r})|^2 d^3\mathbf{r} \end{aligned} \tag{4.15}$$

Therefore, the energy of the states of the very localised electron is independent of $\mathbf{k}$, hence it is expected to see flat bands in the band structure of such a system as shown in Figure (4.10).

Figure 4.10: Band structure of isolated Hydrogen, adopted from First Principles Materials Modelling course material by Prof Matt Probert.

Free electron limit

The other opposite limit is for an electron moving freely in space. In this case, the potential term vanishes and the Hamiltonian consists only from the kinetic energy term; $H = -\frac{\hbar^2}{2m}\nabla^2$. The eigenstates of the Hamiltonian are plane waves as shown in equation

(4.5), thus the energy can be found as follows:

$$\begin{aligned} E(\mathbf{k}) &= -\frac{\hbar^2}{2m}\int \psi^*(\mathbf{r})\nabla^2\psi(\mathbf{r})d^3\mathbf{r} \\ &= -\frac{\hbar^2}{2m}(\mathbf{k}+\mathbf{G})^2\int |\psi(\mathbf{r})|^2 d^3\mathbf{r} \\ &= -\frac{\hbar^2}{2m}(\mathbf{k}+\mathbf{G})^2 \end{aligned} \tag{4.16}$$

Figure 4.11: Free band representation; (a) A single free band, (b) multi-parabola for different lattice points, and (c) folding bands representation, adopted from First Principles Materials Modelling course material by Prof Matt Probert

Consequently, $E(\mathbf{k})$ is quadratic in $\mathbf{k}$, with the lowest energy state at $\mathbf{G}$=0. Thus, the energy of each state changes quadratically with $\mathbf{k}$, and hence an energy band is formed in reciprocal space as shown in Figure (4.11.a). However, states are periodic in reciprocal space and hence a parabola about each lattice point is resulted as depicted in Figure (4.11.b) and hence all of these are folded back using $\mathbf{G}^{'} = \mathbf{G} \pm m.2\pi/\mathbf{L}$ as shown in Figure (4.11.c).

In real materials, electrons are neither completely localised, nor completely delocalised, however, these features in band structures can be recognised as it can be shown in aluminium and copper band structures figures (4.12) and (4.13), respectively. Al is an

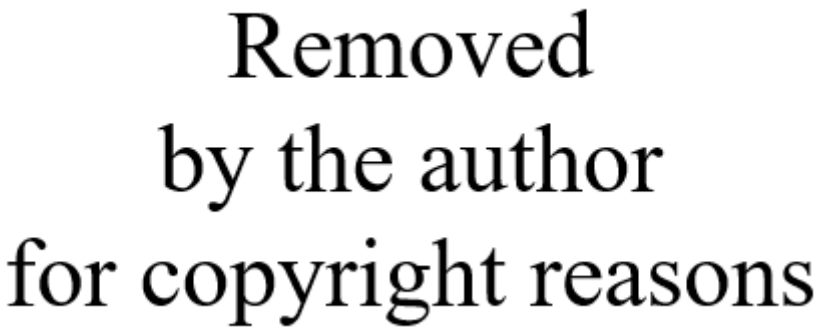

Figure 4.12: Band structure of Al [92].

example of a nearly free electron metal since most bands are parabolic with k. In copper, however, a mixture of localised d-bands and delocalised states can be seen clearly in the band structure. Furthermore, $\mathbf{k}$ is 3-dimensional vector so that $E(\mathbf{k})$ is difficult to visualise. Therefore, the energies are conventionally plotted along special high-symmetry directions. These energies indicate maximum or minimum for the bands across the whole Brillouin Zone. Electrons occupy the lowest energy states and at $T = 0K$ all electronic states below Fermi level are populated and the ones above are vacant. In DFT calculations, band structure is often moved so that $E_F = 0$ and if there is a region just above Fermi level with no bands, the material is a metal, a semiconductor or an insulator depending on the size of the energy gap.

4.8.2 Density of states

Although the band structure is a good way of visualising bands along high symmetry directions, it does not give any information about the number of electronic state at a particular energy which is important for electronic transitions and magnetic and some other properties. What is required in these cases is the full density of states (DOS)

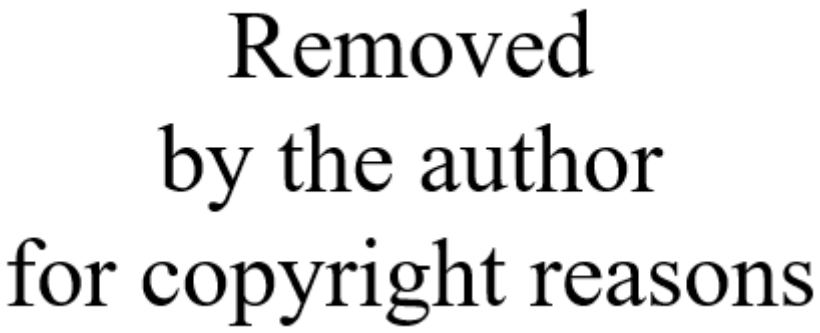

Figure 4.13: Calculated band structure of copper by DFT (solid line), compared with photoemission data (points), adopted from [113].

across the whole Brillouin Zone. The main idea of the plane wave DFT is to express the electronic density in plane-wave basis sets of the form $\exp(i\mathbf{G}.\mathbf{r})$. Therefore, once the calculations are accomplished, the electronic density of states can be calculated by integrating that density in k-space. Thus, uniformly sampling the BZ is essential for performing the integration as for the calculation of the ground state electronic structure. The only difference in this case is the large number of k-points which should be used in this calculation because the details of the DOS originate from integrals in k space.

Similar to the band structure calculation, the number of k-points is reduced to lie inside the irreducible region by symmetry. For delocalised electrons, energy is given by equation (4.16), so that for a fixed energy, the **k**-vectors form a sphere of radius $|\mathbf{k}+\mathbf{G}|$. Therefore, it is straight forward to show that

$$g(E) \sim \sqrt{E} \tag{4.17}$$

Calculation Examples

In this section, some examples of DOS calculations are presented for different materials to show the difference between semiconductors (insulators) and metals and between magnetic and non-magnetic systems.

A. Metallic systems

Figure (4.14) shows the ideal DOS and calculated DOS for three different metals; namely Al, Ag and Pt. The overall shape of the DOS looks similar for all metals where the energy is plotted with respect to Fermi energy, E_f. Clearly, Fermi level is crossing finite DOS which satisfies the definition of a metal. Comparing the three plots, two main differences can be clearly observed. Firstly, the electronic states are more spread in energy in Al and Pt than in Ag. Secondly, the number of the non-populated states just above Fermi level is lower in Ag than in Pt which explain the difference in chemical reactivity.

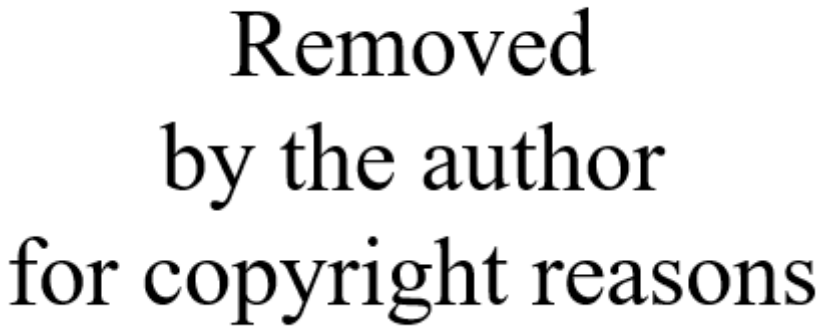

Figure 4.14: Calculated DOS of metals; ideal free electron DOS (top left), calculated DOS of Al (top right), Ag (bottom left), and Pt (bottom right), adopted from [90].

B.Semiconductors and insulators

Figures (4.15) shows the DOS plots for Si and silicon dioxide (quartz) respectively. A

gap region where there are no electronic states separates two regions of occupied and unoccupied bands at $T = 0$; namely the valence and conduction bands, can be clearly seen. Even though DFT predicts correctly the existence of the band gap, the calculated value is usually underestimated as shown in both examples where for instance, in Si the experimental band gap is 1.1 eV, whereas the calculated band gap is 0.67 eV. Similarly in quartz, the calculated value is 5.9 eV while the experimental is much higher; 8.9 eV. This is one of the known DFT failures. However, in these cases it predicts the correct behaviour of the material. It shows that Si is a semiconductor, while predicts an insulating behaviour of quartz. Additionally, there are some places where the slope of the DOS changes discontinuously. These are called Van Hove singularities.

In the previous examples, the band gaps are underestimated by DFT. What is sometimes worse is the failure in predicting the existence of the band gap which happens for a number of narrow band materials such as Ag_2O, Ge, InN, and ScN. In these materials, DFT predicts a metallic behaviour regardless of the numerical details; the same DOS obtained with and without using smearing in k-space and using different XC functionals. Nevertheless, as it has been mentioned earlier in this chapter, there are some approaches to correct for these failures and some of these approaches shall be discussed briefly later.

4.8.3 Magnetism in DFT

As discussed in the previous chapter, magnetic response of the material depends on the distribution of the electronic spins. If they are arranged in such a way that every spin is paired with anti-parallel spin state, the material is diamagnetic. However, if the spins are unpaired, they can be arranged in different ways. If they are parallel, the

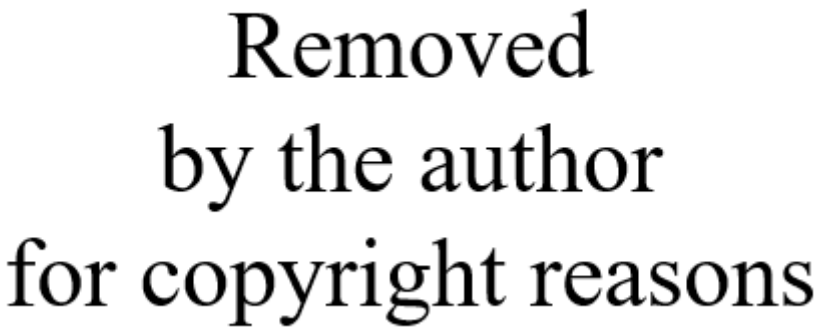

Figure 4.15: Calculated DOS of Si (left) and silicon dioxide (quartz) (right), adopted from [90].

material is ferromagnetic and if they are anti-parallel and have the same magnitudes, the material is antiferromagnetic. More complicated arrangements are also possible. In DFT calculations, if the material is non-magnetic, it is common to not include electron spin and such calculations are referred to as non-polarised. However, if the electron spin matters, the electronic spin state must be specified for the system. Figure (4.16) shows the prototype magnetic example; iron. It clearly shows how spin polarisation specification is important for magnetic materials. The middle plot predicts a non-magnetic state if no spin polarisation is switched on, however, magnetisation of the system is revealed when spin polarisation is included. In terms of the favoured magnetic state and lattice constant, Figure (4.17) shows a DFT energy calculation for the bcc Fe with different magnetic configurations for various lattice constants. It shows that the lowest energy configuration is that where all the spins are aligned parallel to each other. In other words, the spin arrangement greatly lowers the energy and increases the equilibrium lattice constant. Therefore, the ferromagnetic configuration is the most favourable for bcc iron.

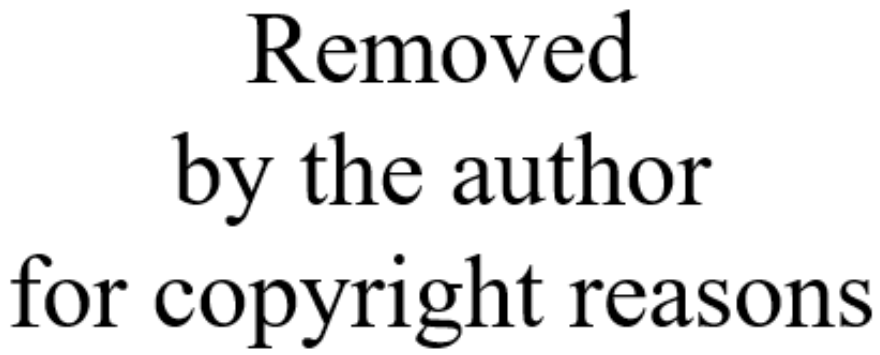

Figure 4.16: Ferromagnetic ground state of BCC iron (left), DOS plot of iron with spin polarisation switched off (middle), and DOS plot with spin polarisation on (right) [91].

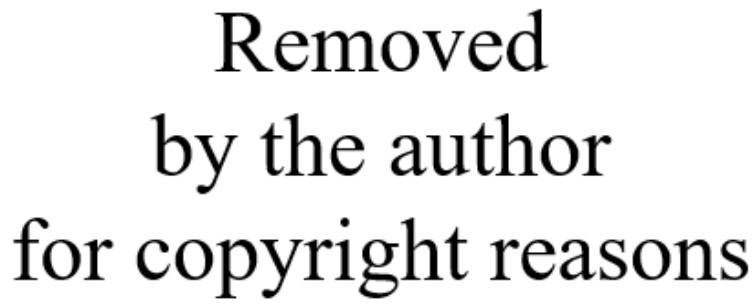

Figure 4.17: Energy of bcc Fe as a function of the lattice constant from DFT calculations with several different spin states. The results labeled 'No spin' are from calculations without spin polarization [90].

4.9 Summary

DFT is a very powerful material modelling technique. The basic principles of such a theory were introduced by Hohenberg, Kohn, and Sham. The first two set up the basic theorems about finding the ground state energy of the system as a function of the electronic density in which the dimensionality of the problem was reduced from being 3N-dimensional to only 3-dimensional. Kohn and Sham have developed an approach that made employing earlier theorems a reality by mapping the many-body problem

into many non-interacting quasi-particle problems. This mapping can be successfully achieved with the existence of some XC approximations which take into account all the neglected interactions. Such approximations are called exchange-correlation functionals and the exact form of the functional is not yet known, however, there are very good approximations.

By exploiting periodicity and Bloch's theorem, constructing the electronic density involves a summation over all possible **k** values. The sampling is performed over the 1^{st} BZ and the number of the **k** points depends on the size of the zone. The standard sampling is called Monkhorst-Pack mesh and the crystal symmetry is used to reduce the number of **k** points required. A dense sampling for metals is needed to capture the discontinuity at the Fermi level. A reasonable number of k points must be used so that the answer is well converged and this cane be checked by performing the convergence test of energy with respect to the number of k-points. Applying all the previous to solids yields a set of many eigenvalue equations where the eigenfunctions are the electron wavefunctions by which the density is constructed. A convenient way of representing the wavefunction and the density in a computer is by writing it in terms of coefficients of known basis functions. The obvious choice for periodic systems is the 3D Fourier series; *i.e* infinite number of plane waves. In practice, this infinite number must be cut at a certain value that insure converged answers for the system which is referred to as the cutoff energy and it is an important parameter in DFT calculations.

The pseudopotential approach is vital in plane wave DFT where the core electrons are combined with the nucleus to make a pseudo-ion, hence reducing the number of electrons

in KS equations. As a result, the outer electrons interact with a weaker potential so that the wavefunctions are smoother inside the core region. Therefore, they require fewer plane waves to be described and hence it is computationally cheaper. The PP approximation can be used safely without affecting any bonding and other properties.

A pre-requisite procedure to any DFT calculations is geometry optimisation of the system under investigation. There are various numerical methods towards achieving the most stable system that can be used. The initial configuration is vital towards achieving a reasonable relaxed geometry; therefore it is worth spending a reasonable time in constructing it. There various types and constrained can be applied to the system during relaxation.

Band structure is an important tool in visualising bands along symmetry directions. Even better tool in most cases is the DOS which shows the number of states at each energy interval and some care must be taken in k-sampling to calculate it. Furthermore, DFT is a very powerful tool in studying magnetic systems by including spin polarisation.

Overall, DFT theorems state that a good approximation to the ground state can be obtained. Although there is no theorem stating that the quasi-particles energies are accurate, however, they usually are using time-dependent DFT. TDFT is an approach to investigate the properties and dynamics of many-body systems in the presence of time-dependent potentials, such as electric or magnetic fields. The effect of such fields on molecules and solids can be studied with TDDFT to extract features like excitation energies, frequency-dependent response properties, and photoabsorption spectra.

Chapter 5

First principles modelling of Co nanoparticles in ZnO

5.1 Introduction

In this chapter, an investigation of Co nanoparticles (NPs) in pure ZnO is presented. The study was accomplished by modelling the Co nanoparticles with Co monolayers (MLs) to simplify the problem. The Co monolayers were considered in two structures; namely hexagonal closed packed structure (hcp), and face centred cubic (fcc) grown in the [0001] and [111]-directions, respectively sandwiched between the (0001) and (000$\bar{1}$) planes of ZnO. The ground state energy of both Co phases embedded in ZnO was compared for different numbers of Co layers. The magnetisation as a function of number of layers was calculated and qualitatively compared for both structures. Furthermore, the exchange coupling between the Co monolayers through the pure ZnO structure was investigated in both Co phases. Although there have been some experimental reports of detecting Co

nanoparticles in Co-doped ZnO films and single crystals, to the best of our knowledge, the Co nanoparticles have not been modelled in the literature and hence this work provides an original theoretical model of Co nanoparticles in ZnO.

This chapter is divided into four main sections; material description of the constituents considered in4rp this chapter presented in section 2. In the third section, the literature on Co ultra thin layers on different substrates as well as on ZnO and Co NPs embedded in ZnO matrix is reviewed in attempt to link the present work with the previous progress on the material. The computational method implemented in this chapter and the discussion of the results are presented in section 4. Finally, the main conclusions of the chapter are given in the final section.

5.2 Material description

5.2.1 Cobalt

Metallic cobalt can crystallize in three different crystal structures [114]: hexagonal closed packed; hcp (α-phase), face centred cubic; fcc (β-phase) and primitive cubic; (ϵ-phase). All these phases have similar energetic stabilities so that a small change in temperature and pressure can lead to a change in the crystal structure from one phase to another. Furthermore, in all these phases, the ferromagnetic ordering is the most stable magnetic configuration. In addition, all the phases possess high room temperature anisotropy of 4.2×10^6, 2.7×10^6 and 1.5×10^6 erg/cm^3 for α, β and ϵ phases respectively [115], [116] and [117]. The high anisotropy and uni-axial symmetry of the hcp structure

makes it applicable in magnetic recording due to its high coercivity, while the lower value of the fcc structure makes it applicable as a soft magnetic material.

Although, α and β- phases can coexist at different conditions, the α-phase is more stable at room temperatures while β-Co is a metastable form at temperatures above $450°C$. The two phases are closed packed structures with high density. The only difference between them is the stacking sequence along (111) plane. As Figure (5.1) demonstrates, the stacking of the three Co layers only differs in the third layer orientation for α and β phases. Therefore, the low energy of forming the stacking fault makes it usually possible to find both phases in the same sample. ϵ phase has a more complex structure which was reported by Dinega et *al* [118]. The structure is metastable and can be transformed to α or β phases easily by annealing. Both α and ϵ structures change their structure to β phase as the temperature is raised before reaching the transition to paramagnetic order. Therefore, the Curie temperature of the two phases has not been reported, while it is 1388 K for a β phase under ambient pressure.

Figure 5.1: HCP (a) and FCC (b) stacking consequence along [111] and [0001] planes.

5.2.2 ZnO

Like most of the group II-VI binary compounds which are composed of a metal from either group 2 or 12 of the periodic table (the alkaline earth metals and group 12 elements, formerly called groups IIA and IIB) and a nonmetal from group 16 (the chalcogens, formerly called group VI), ZnO crystallize in either cubic Zinc blende or hexagonal wurtzite structures. In these structures, each cation is surrounded by four anions at the edges of a tetrahedron, and vice versa. This tetrahedral configuration is typical for sp^3 hybridization of electron states. Therefore, the bonding in ZnO is typically covalent, however, it has a substantial amount of ionic bonding because of the different polarity of the constituents. In a crystal matrix, the neighbouring tetrahedrons form bi-layers, each consisting of a zinc and an oxygen layer. Depending on the stacking sequence of these bi-layers, the wurtzite or the zinc blende structures may be formed. A third phase may be crystallized at relatively high pressures which is the rocksalt structure. The thermodynamically stable phase at ambient conditions is the hexagonal wurtzite, whereas the zinc blende phase may be formed only by growth on cubic substrates. Figure (5.2) shows the three possible crystal structures of ZnO.

Figure 5.2: Cubic rocksalt (a), zinc blende (b) and hexagonal wurtzite (c) structures, taken from [12].

The hexagonal wurtzite structure as shown in Figure (5.2) (c) is uniaxial with two lattice parameters a and c. Its distinct third axis, referred to as c-axis, is directed along one of the tetrahedral binding orbitals. In the plane perpendicular to the c-axis, the primitive translation vectors **a** and **b** have the same magnitude and are separated by a angle of 120^0. The lattice constants are determined by several experimental techniques and theoretical calculations and they are in a good agreement [12]. The a parameter ranges from 3.2475 to 3.2501 Å, and the c constant from 5.2042 to 5.2075 Å. The ratio c/a has values between 1.593 to 1.6035. There is an other important parameter defining this phase which is the bonding length along the c-axis in units of c. The reported range for such value is between 0.383 to 0.3856 in fractional coordinates. The wurtzite primitive unit contains two pairs of ions, i.e. two ZnO formula units. The orientations of the axes and the faces in this type of crystals is denoted by four-digit Miller indices hkil. The c-axis direction is referred to as [0001], and the surface perpendicular to that direction is the hexagonal (0001) plane. The alternating order of the cations and the anions in planes perpendicular to the c-axis leads to faces different in polarity for a c-cut ZnO crystal, the Zn-terminated face on one side and the O-polar face on the other. In contrast, a non-polar face occurs when an equal number of cations and anions are involved. The opposite polarity for faces in the c-cut ZnO crystal is reflected in various properties, e.g. defect characterisation, epitaxial growth properties and magnetic behaviour.

The zinc-blende structure, shown in Figure (5.2)(b), results from two inter-penetrating fcc cubic sub-lattices, displaced by 1/4 of the body diagonal axis. Even though the structure can be considered as the result from interpenetrating cubic structures, the primitive unit cell is not cubic, rather it is an oblique parallelpiped and contains only one pair of

anions and cations. The lattice constant are predicted theoretically to be 4.60 and 4.619 Å, whereas the experimental reported values are lower with values of 4.463, 4.37 and 4.47 Å determined by different measurements.

The third ZnO structure, the rocksalt (NaCl) as shown in Figure (5.2)(a), can only be formed at relatively modest external hydrostatic pressures. The pressure required is about 10 GPa to transfer the wurtzite to rocksalt phase with a large volume reduction of 17% with lattice constant ranging from 4.058 to 4.30 Å [12].

5.3 Previous work

In this section, the main experimental and theoretical results of Co nanoparticles embedded in ZnO as well as the growth of Co on different substrates reported in the literature will be discussed in detail in order to compare them with our present results.

5.3.1 Cobalt hcp versus fcc crystallisation

Co nanoparticles precipitated in ZnO have been examined intensively in the literature see for example [24–27, 119, 120]. The reports have shown that Co clustering in ZnO enhances the magnetic properties of the doped samples. The metallic Co nanoparticles have been shown to be formed under certain experimental conditions such as annealing the implanted [25] or doped [120] samples, reducing the oxygen atmosphere [119], [120] or by hydrogenation [121]. Therefore, there has been a growing interest to study the properties of the metallic nanoparticles in ZnO. These properties include investigating the Co phase

formed in ZnO and its relationship to the in-plane/out-of-plane magnetisation caused in the specimen, calculating the size distribution of the NPs and their ferromagnetic or superparamagnetic behaviour and the magnetic coupling between the NPs.

It has been shown that Co thin (50-500 Å) films electrodeposited onto thin (001) single-crystal copper substrates had a dominant fcc Co structure [115]. Furthermore, a small fraction of the fcc phase has been shown to convert to hcp Co structure when stacking faults exist in the prepared samples. A similar report of the electro-deposited Co films on Au(111) has indicated that the dominant formed phase of Co is thickness dependant as it has been confirmed by NMR measurements shown in Figure (5.3) [122]. As the NMR results demonstrate, for a thickness of 2 nm, the dominant phase is the hcp, whereas, for medium thickness such as 40 nm, a mixed fcc-hcp phase is crystallized, and for large thickness such as 500 nm, the fcc structure is the prevailing phase. For thin samples and under specific growth conditions, the out of plane magnetisation is stabilized, whereas in-plane magnetisation has been found to be the favoured direction for thick samples under any growth conditions. The previous thickness dependant growth mode of cobalt has been found to be completely different to that seen for titanium polycrystalline thin films deposited on Si (100) substrate by planar DC magnetron sputtering [123]. In the latter, Ti films have been found to be gradually transferring from fcc to hcp structure when the thickness is increased.

Regarding Co clustering in ZnO, several investigations have been also implemented. One of these was reported by D.P. Norton *et al.* of bulk Sn-doped ZnO crystals implanted with Co^+ with doses of 3 or 5×10^{16} cm^{-2} at a voltage of 250 keV into the (110)

Figure 5.3: NMR spectra of $t_{Co} = 2, 40, 500$ nm ultra thin Co films deposited on Au(111) [122].

ZnO face [25]. The samples were held at $T = 550\ ^0C$ during the implantation to avoid amorphization of the ZnO lattice. The doped surface was about 2000 Åthick, producing a concentration of Co $\sim 3 - 5$ at %. The samples were then annealed at 700 ^0C for 5 mins in N_2 atmosphere. The XRD results have shown the presence of the metallic (110) oriented hcp Co in the ZnO matrix. Furthermore, in-plane XRD has shown that the Co nanocrystals were grown epitaxially with respect to ZnO host matrix. In addition, the reported magnetisation was consistent with what was expected from the metallic Co present. Another similar experiment was carried out by Yi Wang et al also on bulk ZnO samples doped with 6 at % Co prepared with the solid state reaction technique [121]. The prepared samples were then hydrogenated at 600 ^0C. The XRD measurement of the hydrogenated specimen has, however, detected the Co fcc phase.

More recently in 2016, the magnetic and the structural properties of Co ultra thin films deposited directly on different ZnO polar surfaces and capped with 2.4 nm Pt have been examined [124]. The films were deposited in three different thickness of layers (t_{Co} = 0.4, 0.48, and 0.6 nm). The magnetisation properties were highly polarity dependant. For the Zn-polar sample of the t_{Co}= 0.4 nm, the magnetisation was parallel to the plane

of the sample, whereas it was perpendicular to the plane for the O-polar film with the same thickness. The structural data including XRD and AFM measurements of the 3.6 nm film have demonstrated that the Zn-polar samples have a sharp interface and clear [111] XRD peaks of the Pt and the fcc Co, whereas no sharp interface or [111] peaks were detected of the O-polar film of the same thickness. On the other hand, in both 0.6 nm samples, the signals were present, albeit more pronounced in Zn-polar film. In addition, the HAADF-STEM image of the 3.6 nm Zn-polar sample has shown that the the Co layer near the Co/Pt interface has fcc structure, whereas that close to the Co/ZnO interface, the Co is dominant in hcp (0001) texture as shown in Figure (5.4).

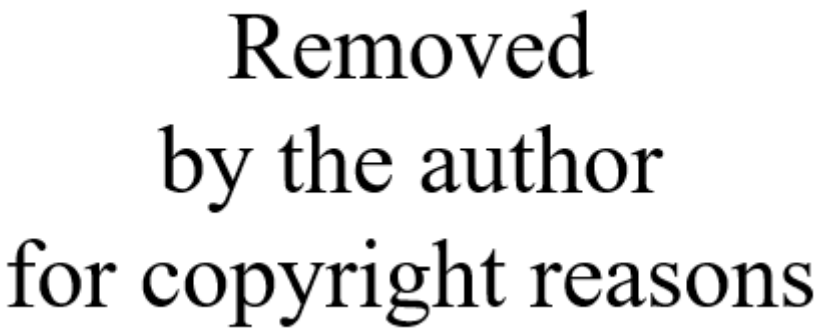

Figure 5.4: The HAADF-STEM image for a sample with t_{Co} =3.6 nm deposited on Zn-polar surface, adopted from [124].

In a very recent paper, a study of post-annealed Co-doped ZnO samples prepared by channel-spark ablation was reported [120]. The films were deposited on Si(100) with temperature range of 350- 450 ^{0}C. The films were then subjected to a post-annealing treatment at either 400 or 600^{0}C for an hour. Metallic Co phase has been detected in the deposited films by XRD measurements which have also shown that the amount of the detected Co slightly increased when the deposition temperature was raised from 350

to 450 ^{0}C. Furthermore, the measurements have shown an increase in the density of the Co nanoparticles in the post-growth annealed samples relative to the as-deposited films. However, annealing at 400 °C has been found to increase content of the hcp metallic Co as well as a better particle size and crystallinity of ZnO hexagonal wurtzite structure relative to the films annealed at 600 °C as shown in Figure (5.5).

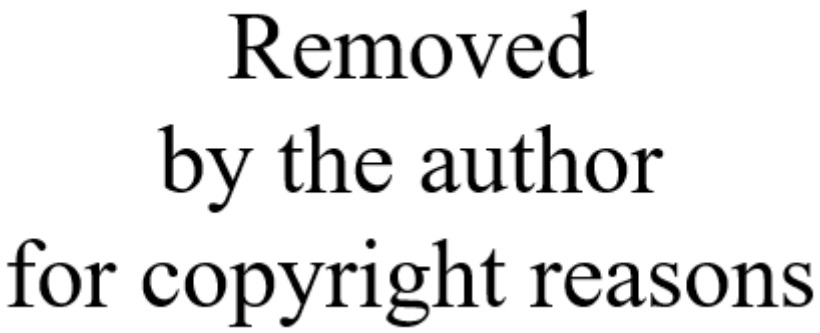

Figure 5.5: XRD measurements of as-grown Co-doped ZnO film at 450°C (a), annealed at 400°C, and annealed at 600°C, adopted from [120].

In a series of investigations in Co-doped ZnO films prepared by PLD under a reduced atmosphere at different substrate temperatures, Co nanoparticles were detected mostly with elliptical shape with their main axis was out of plane, however, some were spherical [15,125,126]. The crystallites were in the hcp phase and (0001)-oriented on ZnO(0001). Moreover, the sizes of the clusters were reported to be dependent on the substrate temperature. The average widths were 1.3 nm, 4-5 nm, and 10 nm and the heights were 6.5 nm, 4-60 nm, and 10-30 nm for the samples deposited at RT, 350°C, and 500 °C, respectively.

5.3.2 Co/ZnO interface

There have been very few theoretical models of a Co monolayer adsorbed on ZnO in literature. Nevertheless, these reports will be discussed in detail in order to compare what it has been found and our present results. Kim Y. *et al* have implemented a first principles study of transition metals adsorbed on polar-ZnO surfaces [127]. The electronic and magnetic properties of the investigated TMs, Co and Mn, were calculated using projected-augmented-wave(PAW) based on DFT. The generalized gradient approximation (GGA) exchange-correlation functional was employed as implemented in VASP. The wave functions were expanded using a cutoff energy 400 eV and the total energy of the system was calculated using a mesh of 3 $\times$ 3 $\times$1 Gamma-centred Monkhrost-Pack method mentioned in chapter 4. In both TMs investigated, it has been found that for T_4 position is energetically favourable for Zn-terminated, while in O-polar surface, the H_3 position is more stable (cf. Figure (5.6)). The total magnetic moment and the magnetisation energy has been acquired by spin-polarized calculation for the TM atoms in the polar ZnO surface supercell. It has been found that the adsorption of both TMs on the O-polar ZnO surface to induce half-metallic behaviour, stable ferromagnetism, and a wide spin band gap, which are preferable for realizing spintronics devices. Another similar calculation has been implemented using the same cutoff energy and same exchange-correlation functional and the simulation package VASP, however, a different k-point mesh of 4$\times$ 4$\times$ 1 by Chen X. et *el* [128]. The Co atom has been found to be easily adsorbed at the H_3 for the O-terminated surfaces with agreement with [127]. However, the calculated magnetic moment has been reported to be higher for the O-terminated surfaces unlike what has been found in the latter for the case of Co. From a calculation of the partial density of states of the 3d orbitals of the adsorbed Co with different polarity, it has been

found that the majority spin density of Co 3d is more delocalized on the O-polar surface. Furthermore, the exchange coupling for a pair of adsorbed Co atoms has been found to be ferromagnetically favourable for both termination and adsorption positions which is favourable in spin injection applications.

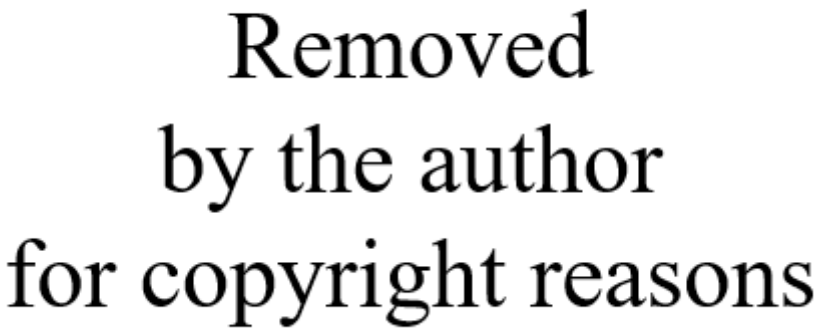

Figure 5.6: Top view of ZnO structure with H_3 and T_4 positions labelled, adopted from [127].

An interesting experimental study of the Co/ZnO interface has been carried out by Dumont *et al.* by means of high energy X-ray [129]. The Co ultra-thin layer were deposited on O-polar ZnO $(000\bar{1})$ single crystal by the nucleation of nanometre-sized clusters at room temperature. Post-growth annealing at different temperatures from 600 to 970 K have been indicated different interface reactions. At the minimum temperature used, the Co clusters have been found to accumulate preserving their metallic nature. At higher temperature namely at 780 K, the metallic Co atoms were gradually oxidized to Co^{2+} and hence a thin Co rich (Co,Zn)O layer is formed as a result of Co^{2+} substitution on Zn sites. Increasing the temperature to 970 K has induced a diffusion of Co into the ZnO lattice leaving zinc vacancies behind. The different reactions occur at various temperatures at the interface was demonstrated in Figure (5.7). A very similar report has been done earlier in 2009 for Co vapour-phase deposited on single crystal ZnO(0001) surfaces. Room

temperature deposition has led to a layer-by-layer growth of Co. However, similar to the previous study, heating the samples up to 700 K leads to formation of large Co nano particles. Annealing at temperatures between 700-800 K leads to a distribution of Co atoms over the ZnO surface and CoO was formed as a result of the reaction with ZnO support in this stage by XPS measurements, and increasing the temperature beyond that leads to an incorporation of Co into ZnO substrate.

Figure 5.7: Ultra-thin Co deposition on O-polar ZnO single crystal (a), (b) and (c), post-growth annealing at different temperatures from 600 to 970 K (d)- (h) [129].

5.3.3 Amorphous granular Co/ZnO films

The magnetisation and interfacial region were investigated in Co:ZnO sputtered amorphus films. The target system has been designed to compose of finite number of Co/ZnO wafers and finite layer thickness. Such systems have been studied intensively in the literature [14, 28, 70, 130–133]. It is usually grown on glass or silicon substrates by depositing the layers from Co and ZnO targets at room temperature by magnetron sputtering technique. Magnetron Sputtering is a Plasma Vapor Deposition (PVD) process in which a plasma (usually from argon) is created and positively charged ions from the plasma are

accelerated by an electrical field superimposed on the negatively charged electrode or "target". The positive ions are accelerated by potentials ranging from a few hundreds to a few thousands electron volts and strike the negative electrode with sufficient force to dislodge and eject atoms from the target. These atoms will be ejected in a typical line-of-sight cosine distribution from the face of the target and will condense on surfaces that are placed in proximity to the magnetron sputtering cathode [134]. The magnetisation measurements of $[\mathrm{Co(0.6nm)/ZnO(xnm)}]_{60}$ for $\mathrm{x} = 0.4\mathrm{nm}, 3\mathrm{nm}$ has indicated that the magnetisation has been enhanced for both thicknesses after annealing as shown in Figure (5.8), while the magneto-optical measurement has not shown any increase in the measured MCD spectra, however, the spectra has shown to be decreasing [70] which was not expected according to Maxwell-Garnet theory of nanoparticles [46]. Furthermore, the magnetism of the samples has been found to transfer from superparamagnetism to ferromagnetism after annealing. This has been explained by measuring the magnetoresistance of both samples before and after annealing, and it has been concluded that the multilayer structure may have transformed to granular structure by interdiffusion of Co into ZnO and the Co precipitate within this structure after annealing [14]. Quan *et al* have shown by means of structural and magnetic analysis of Co/ZnO amorphous films that the as-prepared specimen composed of regions of metallic Co and semiconducting ZnO [130]. Large negative magnetoresistance has been detected for the as-deposited sample containing 50.7 at % at 10 and 300 K. This has been attributed to the induced spin-dependant tunnelling between regions of conducting magnetic Co through ZnO semiconducting barriers. In another investigation [28], they have investigated the origin of the MR effect and the high spin polarisation of tunnelling electrons in Co/ZnO and Co/ZnCoAlO granular films at thickness x = 1.00 and 3.00 nm at room temperature. They have concluded that

the MR and the magnetisation are enhanced with decreasing thickness and with adding Al to ZnO matrix. By investigating the source of magnetisation in both films, a model of different regions in the film has been proposed, as shown in Figure (5.9). According to the proposed picture, the films consist of superparamagnetic Co particles, semiconductor matrix, and the interfacial magnetic semiconductors composing of $Zn_{1-x}Co_xO$, where $0 < x <$ Co solubility limit in ZnO.

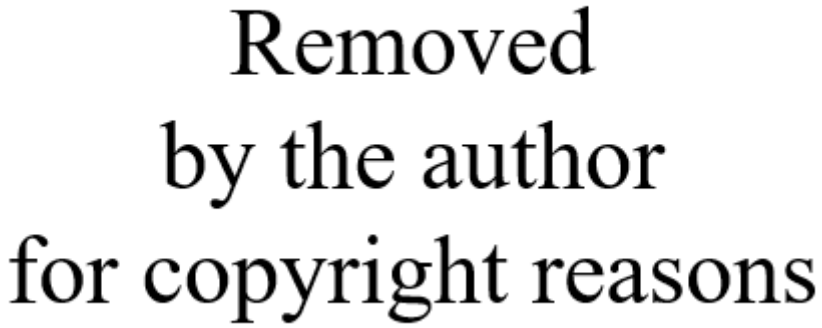

Figure 5.8: Hysteresis loops of $[Co(0.6nm)/ZnO(xnm)]_{60}$ befor and after annealing for x= 0.4 (a), and x= 3 (b), adopted from [70].

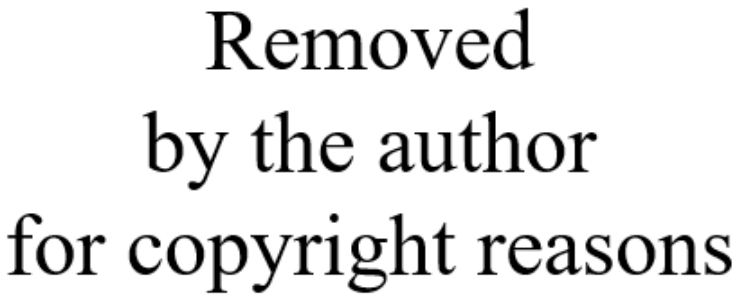

Figure 5.9: A proposed model of regions in Co/ZnO granular films. The regions are Co nanoparticles, semiconductor matrix, and the interfacial magnetic semiconductors [28].

Quan *et al.* have studied the relation between the value of the MR and the conductivity and the thickness of the ZnO buffer layer [133]. The main results of the study is shown in Figure (5.10). The results can be explained in the shade of the regimes described in [14]. For thin ZnO layers ,$\leq$ 0.7 nm, the increasing value of the MR is attributed to the strong coupling between the Co layers mediated by the nonmagnetic thin layer of ZnO. However, for the thick ZnO layers, $\geq$ 1 nm, the coupling between the Co layers is very weak through the thick ZnO buffer layer and hence the resistivity increases and the MR decreases in this regime.

Figure 5.10: MR value of Co/ZnO films as a function of resistivity for variant thicknesses of ZnO deposited layer, adopted from [129].

5.4 Present work

5.4.1 Computational method

System details

Two vertical ZnO unit cells were used as a base structure for all the calculations in this chapter. The initial lattice parameters were constructed from the experimental values reported in the literature as in table (5.1). The system was then fully relaxed with variable cell optimisation and the theoretical lattice constants were determined. Bulk Co was distorted to obtain perfect lattice matching with the ZnO base structure. The distortion was accomplished by expanding the lattice constant in the direction parallel to the (0001) plane with a ratio ~ 1.3 and shrinking the lattice constant in the perpendicular direction so that the volume of the unit cell is the same as that for bulk. Co monolayers (MLs) were then sequentially added and fully relaxed on the top of the ZnO base structure in two different Co phases; namely fcc and hcp in the [111] and [0001] directions, respectively. The optimisation was done with constant volume and relaxing the internal coordinates of the ions after adding the Co MLs on top of ZnO. The Co atoms in the first ML were placed at H_3 position as shown in Figure (5.6) [128] and Figure (5.13). In the B-layer, the atoms are positioned immediately on top of the final Zn layer, whereas in C-oriented layer, the Co atoms were positioned at the top of the final O-layer, in T_4 position. No vacuum was used in this study, rather, Co MLs were sandwiched within the ZnO base structure in the [0001] direction by exploiting periodicity implemented in DFT. A sketch of the model structure of Co nanoparticles in ZnO is shown in Figure (5.11). The real nanoparticles that are observed in a fc/zfc experiments are large > 2 nm which is equivalent to approx-

imately 10 unit cells in size. Ideally the lateral direction should also have been restricted to 10 unit cells too. As we were modelling the centre of the nanoparticle we can assume that the boundaries with ZnO in the x-y plane are too far away to be considered. This is especially true for oblate-shaped nanoparticles (pancake) with their main axis normal to the [0001] direction. In this case the lateral size is much larger than the vertical as shown in Figure(5.11). The layer by layer growth has been justified experimentally for Co nanocrystals with respect to ZnO host matrix [25]. Furthermore, the nanoparticles have been found to be (0001)-oriented on ZnO(0001) plane for ZnO PLD samples containing Co nanoparticles [15, 125, 126]. A sketch of the simulation cell used in the calculatons with Co in the hcp phase for six Co MLs is shown in Figure (5.12).

The exchange calculations were performed in both phases by repeating the structure

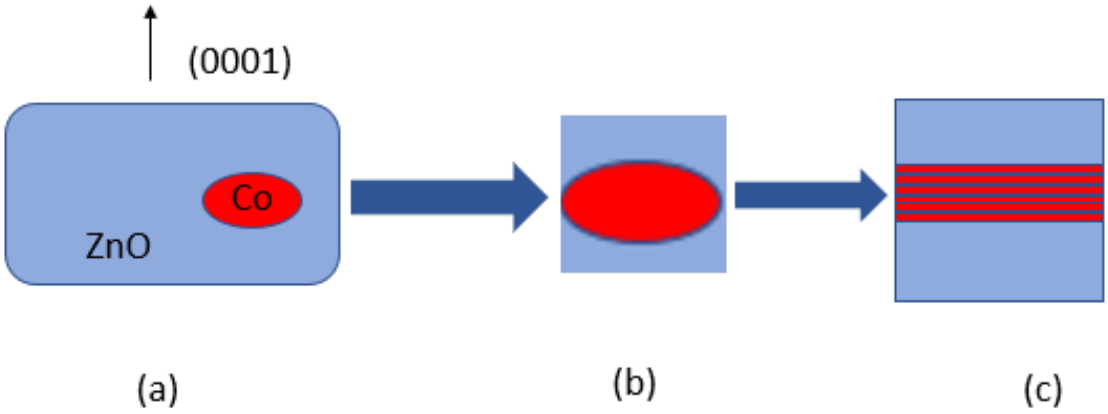

Figure 5.11: A simplified model of Co nanoparticle with oblate-shape in ZnO (a), the model zooms in the interfacial region of the oplate-shaped NP (b), which is modelled with Co monolayers sandwiched within the ZnO structure in the (0001) direction (c).

with the largest number of Co layers, ie. six, in the z-direction with parallel and antiparallel alignments of Co blocks as shown in Figure (5.13) and calculating their corresponding energies.

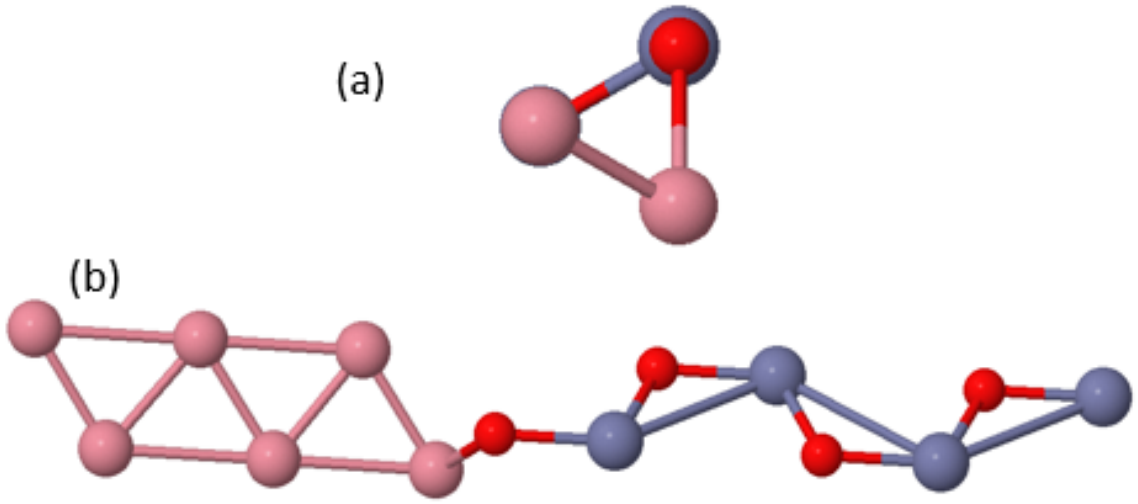

Figure 5.12: A sketch of the simulation cell used in calculation considering the Co in hcp structure with six MLs, (a) top view, (b) side view of the supercell.

Method details

The total energy and electronic structure calculations were performed using Kohn-Sham [87], [88] formalism of density functional theory as implemented in the CASTEP package [135]. The (OTF) CASTEP (16.11) potential was used with valence electrons for Zn $(3d)^{10}(4s)^2$, $(2s)^2(2p)^4$, for O and $(3d)^7(4s)^2$ for Co. A cutoff energy of about 870 eV for plane wave expansion was used. Integration in the reciprocal space was implemented using the Monkhorst-Pack sampling of the Brillouin zone, and k-point mesh of 10×10×2 and 10×10×1 Gamma-centred Monkhorst-Pack method [107] for calculating the magnetisation and exchange energies, respectively. The very high cutoff energy and the fine k-point grid were implemented due to the sensitivity of the magnetic interactions to the convergence quality [136]. The DOS plots were calculated using OptaDOS method [137].

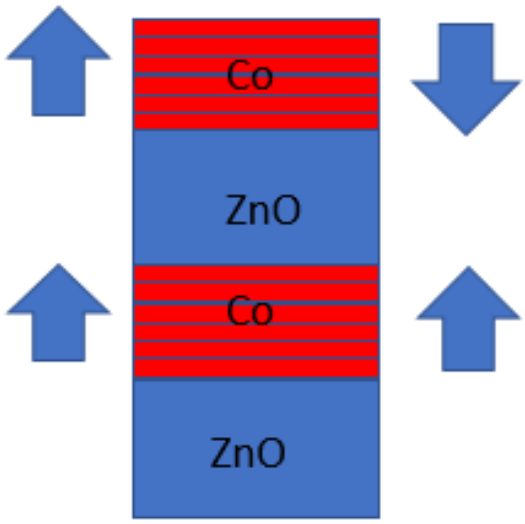

Figure 5.13: A sketch of exchange supercell.

For all geometry optimisations of the Co/ZnO systems of different number of Co MLs, the volume was kept constant and all the internal coordinates were relaxed until Hellmann-Feynman forces were less than 0.001 eV/Å. A Gaussian smearing technique with 0.05 eV width was applied to enhance convergence but all energies presented in the following were obtained by extrapolating to zero smearing.

The exchange-correlation functional was approximated with the Local Density Approximation (LDA). GGA (PBE) was also used for bulk calculations and for one Co ML only for comparison. For the magnetic calculations of the Co/ZnO with hcp Co, the fully localised limit of the LDA+ U method was also used for the system with one to three Co layers only for comparison. Here we use a typical value of $U_{eff} = U - J$ of 4 eV on all d-orbitals of Co atoms. Furthermore, a spin polarisation scheme was adopted and applied for all Co atoms in all calculations.

5.4.2 Results and discussion

Bulk calculations

A. LDA calculations

Table (5.1) presents the calculated lattice constants of ZnO and Co and the details of the magnetic moments and the ground state energy change of Co fcc and hcp due to distortion compared to bulk values. The results showed a reduction of the ZnO lattice parameters with respect to the experimental values. The theoretical values are a =3.186 Å and c = 5.15 Å in good agreement with other DFT calculated values [138] and compared to the experimental values of 3.25 Å and 5.205 Å respectively [12]. The present results of lattice constants are lower than the experimental values since they were obtained using LDA which shortens the bonding lengths and hence underestimates the lattice constants. Distortion of both Co phases led to a slight increase in the ground state energy as it was expected, however, the magnetisation of the distorted Co, in both phases, slightly increased.

B. GGA calculations

The ZnO base structure was also geometry optimised but using GGA functional (PBE) in order to compare between the two results. The resulted lattice constants were 3.28 Å, and 5.29 Å for a and c, respectively. These are higher than the experimental results, in sharp contrast to LDA result as it was expected, as the GGA under-binds the species and hence lengthens the lattice parameters. However, the ratio c/a was 1.614 which is

material	**lattice constant a (Å)**	**lattice constant c (Å)**	**Magnetic moment μ_B/Co**	**Ground state energy per atom** (eV)
ZnO	3.19 *(3.25)*	5.15 *(5.20)*	/	/
Co (fcc)	3.43 *(3.54)*	/	1.62 *(1.70)*	-1094.87
Co(fcc) distorted	4.5		1.87	-1093.99
Co (hcp)	2.45 (*2.50*)	4.00 (*4.06*)	1.56 (*1.70*)	-1094.91
Co(hcp) distorted	3.19	3.00	1.76	-1094.15

Table 5.1: Lattice constants, magnetic moments and ground state energies of the bulk and the distorted systems. The experimental values (in italics) are added for comparison, adopted from [12].

comparable to experimental results. The value of u was 0.378 in fractional coordinates which is slightly lower than experimental values.

Co phase preference in ZnO

The calculated ground state energy of Co/ZnO system in two different Co phases; fcc and hcp, was compared for both phases for an increased number of Co layers. The main results of the comparison are shown in Figure (5.14). As the plot shows, for three cobalt monolayers, the difference is nearly zero which means that when the Co layer at the Co-Zn interface is A (hcp) or C (fcc), the system nearly has the same ground state energy.

Whereas whenever there is a choice between A and B as an interfacial layer, the system prefers to have A layer at the Co-Zn interface as in four layers stack, where the system is more stable in fcc structure, and the five where hcp is more stable. Furthermore, the system prefers the B Co layer when the choice is between B and C layers as in the six monolayers case. This gives higher probability of forming hcp cobalt phase in ZnO as indicated in the literature review [25, 120, 124]. Figure (5.15) shows a schematic sketch of

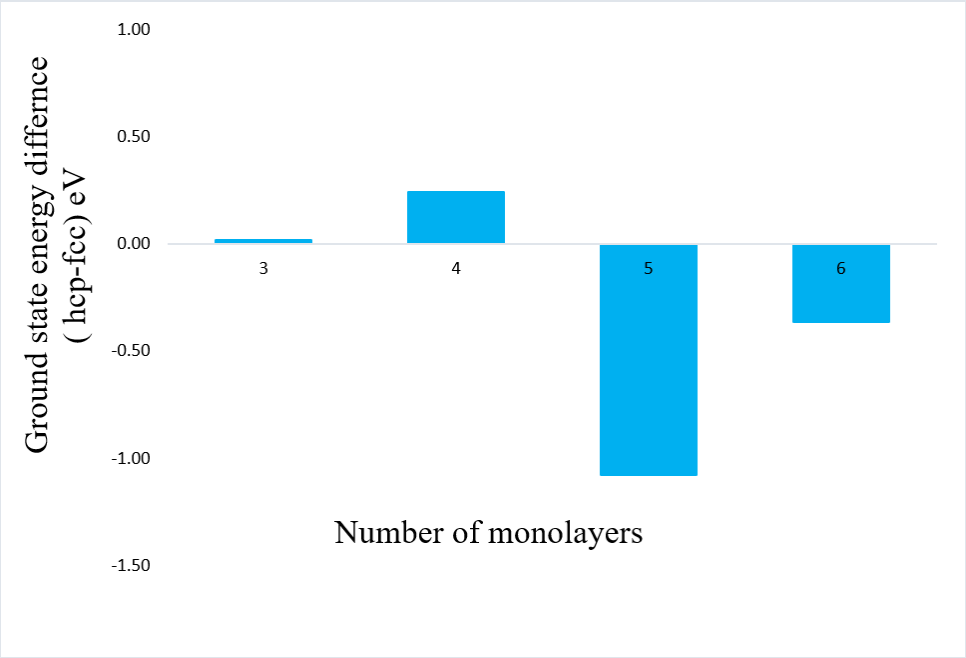

Figure 5.14: The difference of the ground state energy per supercell between hcp and fcc cobalt phases in ZnO.

the Co-O interface and the three orientations at the Co-Zn interface. The O-Co interfacial Co layer was fixed as A-oriented, where all Co atoms were placed in the H_3 as shown in Figure (5.15)(a). However, the Co-Zn interfacial Co can have any orientation depending on the number of layers and on the Co phase, Figure (5.15)(b-d).

The ground state energy per atom increases linearly with increasing the number of the added Co layers as it was expected as shown in Figure (5.16) (a). As the figure shows,

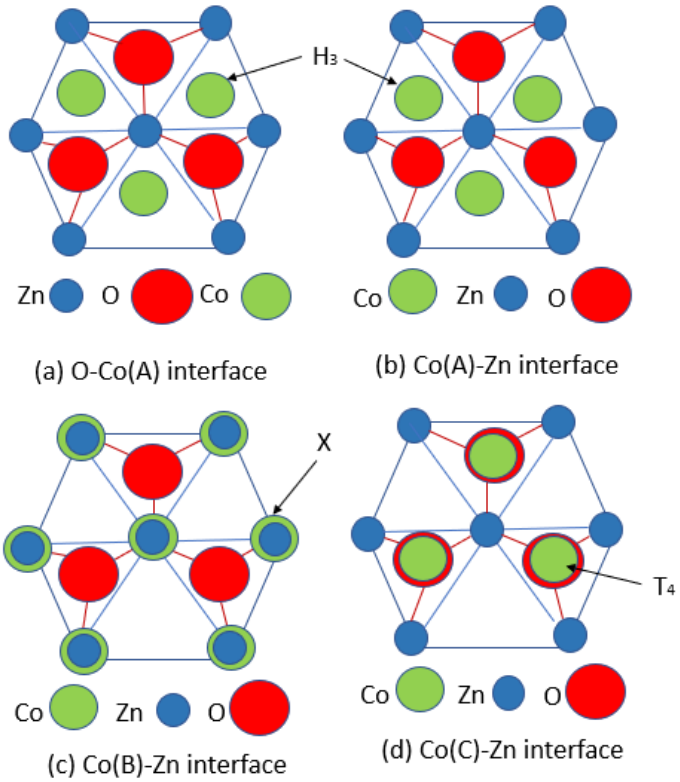

Figure 5.15: Top view of O-Co(A) (a), Co(A)-Zn (b), Co(b)-Zn (c), and Co(C)-Zn interfaces with the positions H_3, X and T_4 are labelled.

the energy calculated for the Co/ZnO system was very close to that calculated from bulk values of Co and ZnO for both phases. Figure(5.16)(b) shows the difference of the ground state energy per Co layer. The difference between the two values was small and it is due to the energy of the interfaces. As figure (5.16) (b) demonstrates, the average difference between the two ground state energies per Co for $n > 1$ decreases with increasing the number of Co layers which means adding more Co layers will stabilize the system towards bulk Co structure.

Magnetisation of Co/ZnO system; hcp cobalt

A. LDA (GGA) calculations

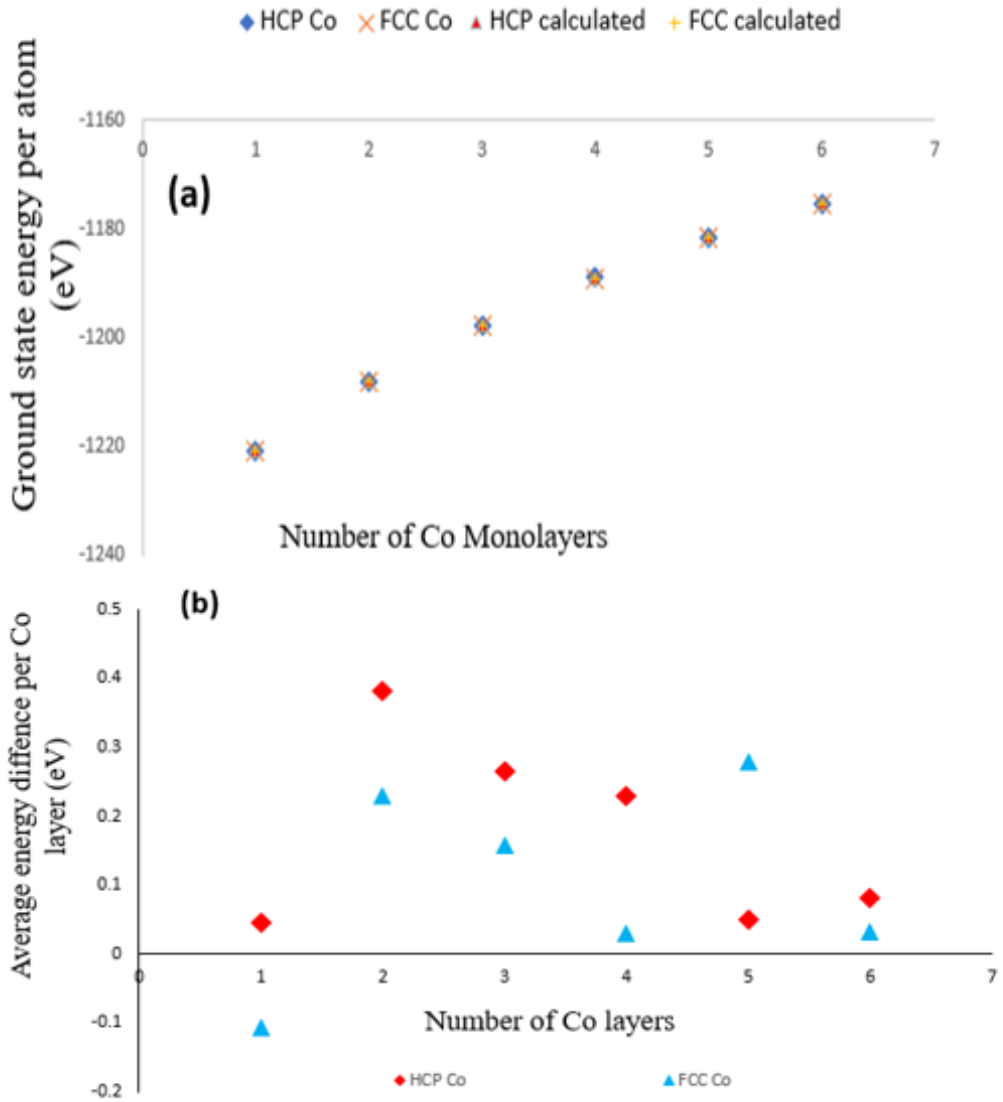

Figure 5.16: (a) The ground state energy per atom of the Co/ZnO system as a function of the number of Co layers in fcc and hcp phases compared to those calculated using bulk values. (b) The average energy difference per Co layer as a function of number of layers in supercell.

The magnetic moment of the Co/ZnO system where the Co monolayers are stacked in the hcp phase along (0001) direction for multiple number of monolayers up to six was evaluated. The results of the calculations are shown in Figure (5.17) where the magnetic moment (measured in $\mu_B/atom$) was labelled on each magnetic layer. The one and two monolayers system were common for both cobalt phases as the specific phase is defined with how the third layer is stacked. As shown in the figure, the layer stacking alternated

sequentially between A and B (ABABABA...). For all systems from three to six cobalt layers, the oxygen layer at the Co-O interface was slightly polarised. Moreover, the cobalt layer at the Co-O interface had lower magnetic moment than other cobalt layers, however, it was slightly more magnetic in the even number of layers system than that of the odd ones. Another obvious difference between the odd and the even systems was the way that the magnetic moment varies between the cobalt layers from Co-O to the Co-Zn interface. In both systems, the magnetic moment increased gradually in this direction till the final B layer was reached and then it dropped for the final A layer as in the odd-layers system. As more layers were added, the magnetic moments of the middle and the interfacial Co-Zn layers approached the bulk value. This was because of the charge flow from the oxygen and its adjacent Co towards the other Co layers. The results showed that adding more Co layers stablizes the metallic stack towards the bulk charge and magnetisation which is useful in estimating magnetisation due to Co clusters in ZnO samples. The interfacial polarised region is important in device applications since it gives high values of magnetoresistnace due to electron tunnelling between the semiconductor and the metallic region [28]. The FM coupling preference was confirmed by the resulting bond angles between Co and O ions. By inspecting the Co-O-Co bonding angles, which were 108°, 124°, 109°, 105°, 104°, and 105° for n_{Co}=1 to 6, respectively, which were closer to 90° than 180° and hence there was no signs of any reduction in the Co moments due to AFM exchange between Co ions at the Co-O interface. Furthermore, the interfacial Co ions were influenced by the other ferromagnetic Co ions in the metallic stack and therefore they are ferromagnetic.

Figure 5.17: Magnetisation results of multiple number of hcp (A, B, A, ...) cobalt, oxygen and zinc interfacial layers. The magnetic moment is labelled on each magnetic layer in (μ_B) and the charge in multiple of e (middle bold).

The calculations were also performed using the GGA functional (PBE) for only one Co layer in order to compare with LDA results. The magnetic moment of the Co, O-interfacial and Zn-interfacial layers were found to be 2.15, 0.33 and -0.07 μ_B respectively. Not surprisingly, the magnetic moments using PBE were slightly higher than the corresponding values using LDA, Figure (5.17), as GGA was found to result in larger lattice parameters. Figure (5.18) shows the total magnetic moment of the system as a function of the number of layers. As it can be seen, the total magnetic moment was slightly higher for the even number of layers than that of the odd ones because of the higher magnetic moment of both

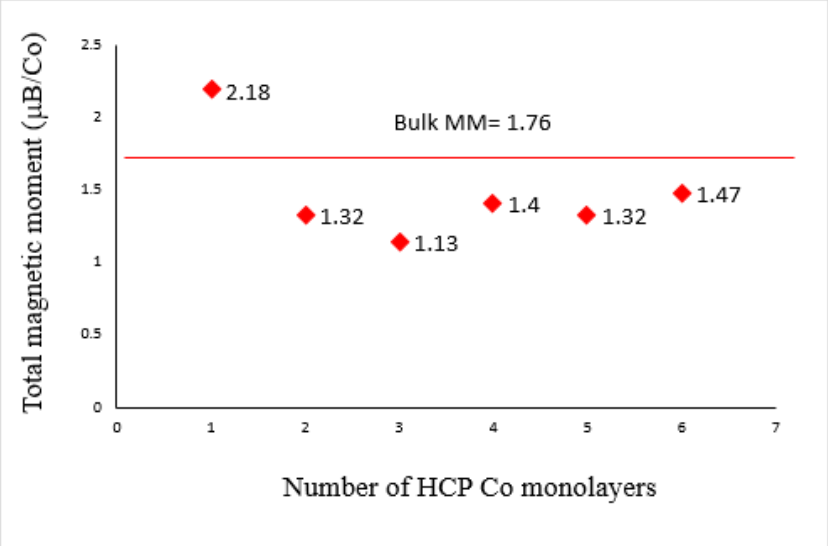

Figure 5.18: The variation of the total magnetic moment of the Co/ZnO in hcp cobalt as a function of the number of Co layers. Bulk magnetic of the distorted Co hcp was added for reference.

cobalt interfacial layers of the even-layer system. Additionally, the total magnetisation of the system increased gradually with adding more Co layers for even and odd-layers systems separately. This pattern of magnetic moment fluctuation between the odd and even systems with an overall increase of each is expected to continue by adding more layers until the bulk magnetisation value is reached. Figure (5.19) shows the calculated density of states (DOS) of the Co/ZnO system in the hcp cobalt phase for one to six Co layers. The change of the total magnetisation between different number of layers was reflected in the different values of the DOS at the Fermi level. The main feature of all DOS plots was the finite DOS at Fermi level which is a fingerprint of the metallic systems. Figure (5.20) shows the density of states plots for six Co monolayers systems compared with bulk Co and ZnO for both Co phases. It shows that the calculated DOS of the Co/ZnO system is an overlap of the DOS of the two bulk materials. The overall difference between the systems in both phases is due to the slightly different shape of the DOS of the corresponding Co phases. In both phases, the metallic feature at the Fermi

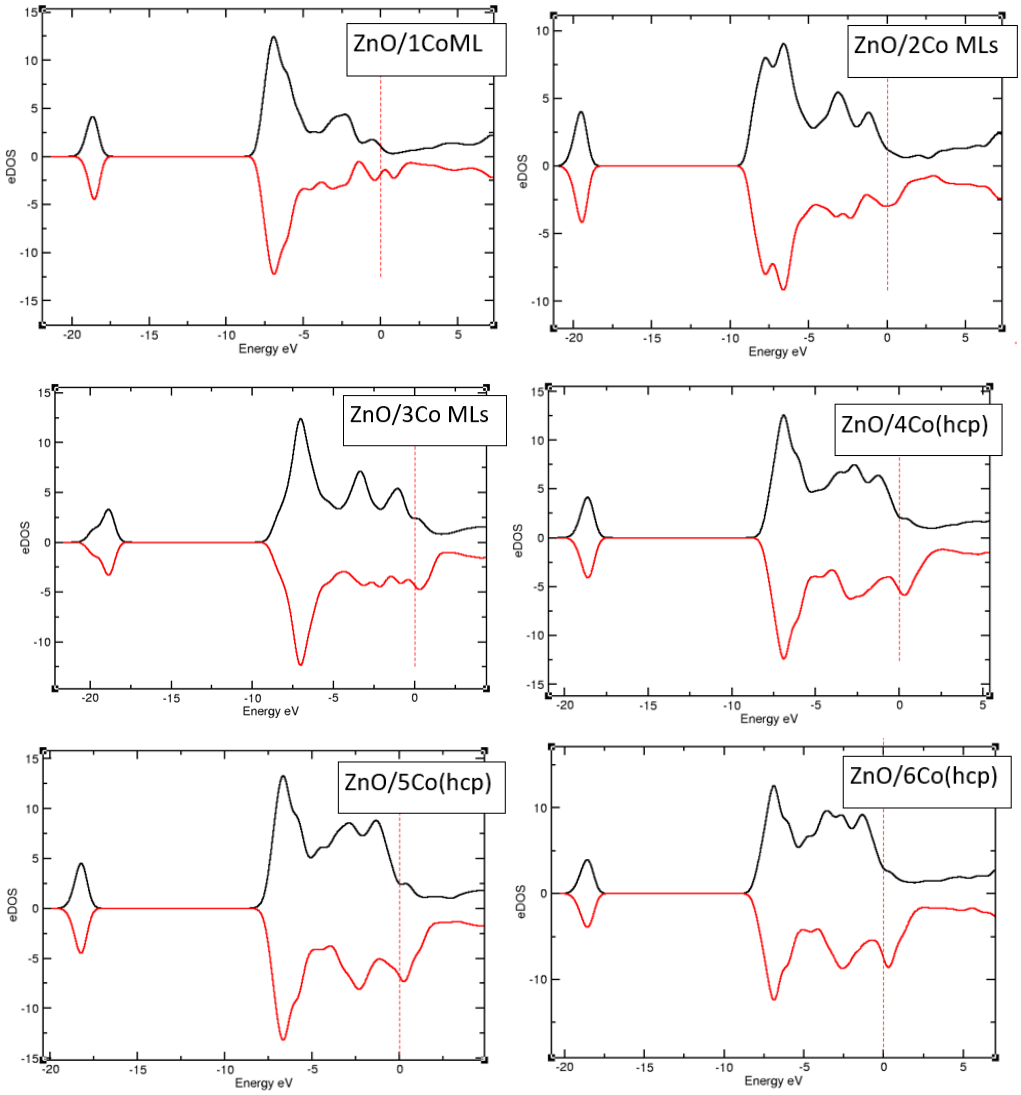

Figure 5.19: Calculated DOS for Co/ZnO system in the hcp phase for one to six MLs from left to right. Energy was scaled with respect to E_F. All DOS plots were produced by OptaDOS method [137].

level is clearly exhibited.

The magnetic exchange energies of the ferromagnetic and the antiferromagnetic alignments were calculated between two blocks of six cobalt layers through two unit cells of ZnO as shown in Figure (5.13). The difference of energy between the two alignments ($\Delta E = E_{AFM} - E_{FM}$) was found to be about + 77 meV per supercell. The sign indicates that the ferromagnetic alignment is energetically more stable than the counterpart anti-

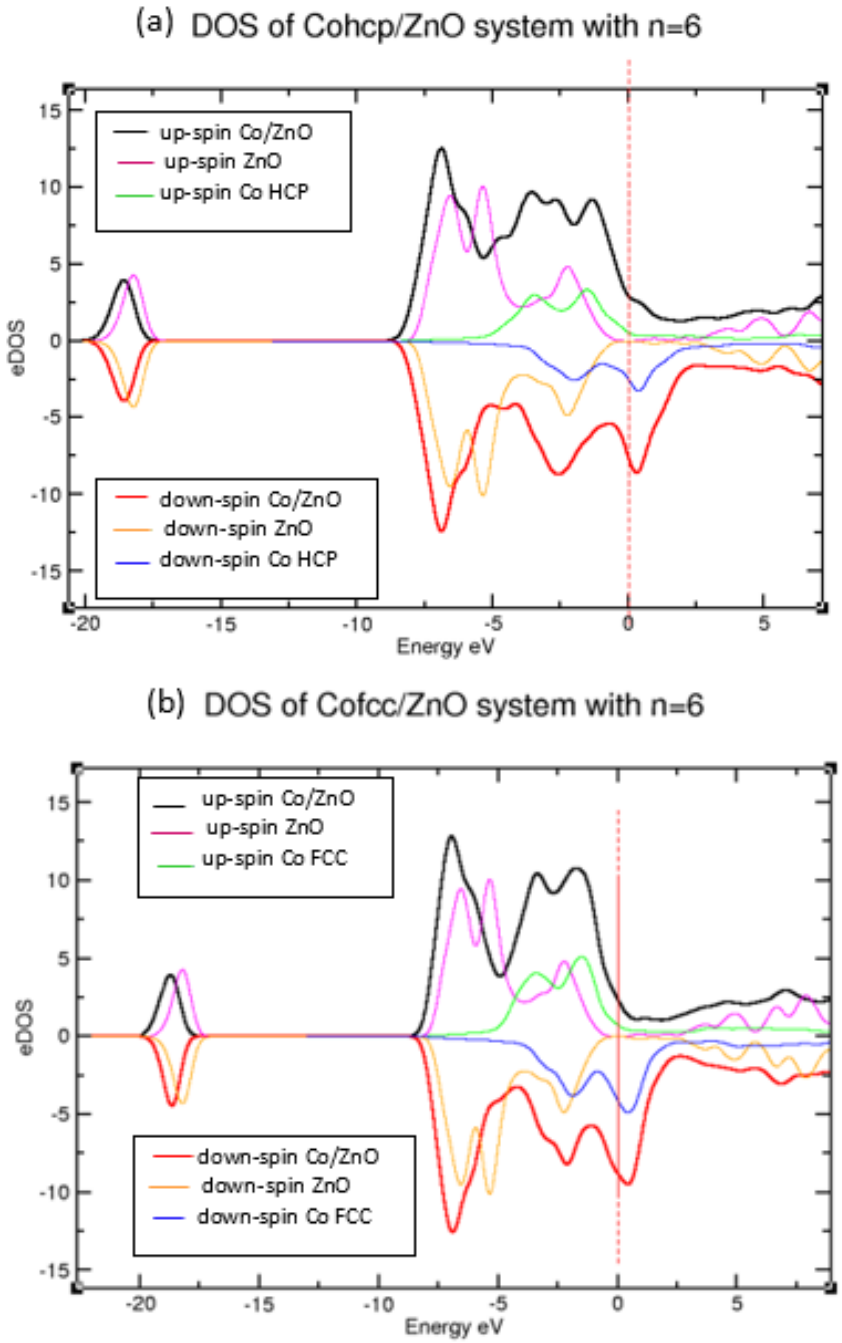

Figure 5.20: Calculated DOS for Co/ZnO system in the (a) hcp phase, and (b) fcc phase for six Co monolayers compared with DOS of bulk ZnO (purple and orange) and Co (distorted) (green and blue). Energy was scaled with respect to Fermi level.

ferromagnetic orientation. In experiments, the ZnO spacer is much thicker than that in our simulation, and that is also true for the thickness of the Co nanoparticle which means the magnitude may be very different from what we calculate. However, the type of the

magnetic interaction between the NPs which matters in our study.

B. LDA +U calculations

The magnetic properties of the hcp Co/ZnO system were also investigated using LDA+U

O		
Zn		
A	+ 0.36	2.52
O	- 0.71	0.23
Zn	+ 0.22	-0.03

O		
Zn		
B	- 0.32	1.95
A	+ 0.23	2.33
O	- 0.69	0.21
Zn	+ 0.43	-0.04

O		
Zn		
A	- 0.34	1.99
B	- 0.28	2.02
A	+ 0.30	2.41
O	- 0.70	0.24
Zn	+ 0.64	0.00

Figure 5.21: LDA+U results of the magnetic moment and the charge of the hcp system up to n=3.

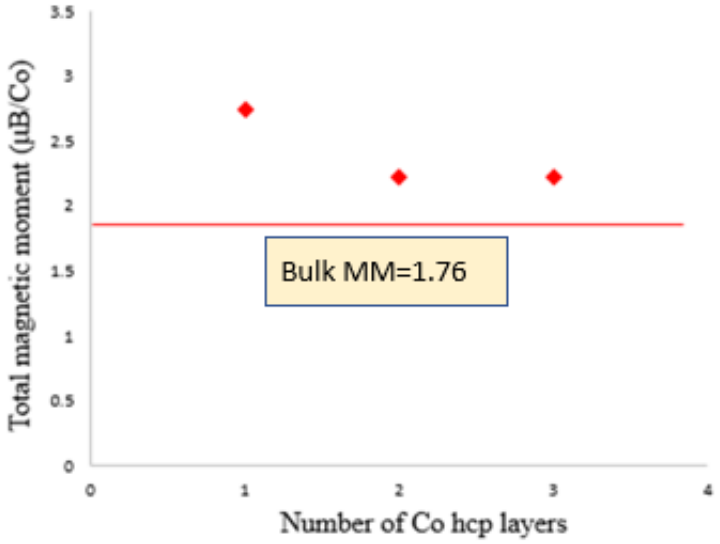

Figure 5.22: The total magnetic moment of the hcp system up to n=3 using LDA+U as a function of n, number of Co layers.

method. The magnetic moment of the distorted bulk Co in hcp phase was, unsurprisingly, found to be $1.85\mu_B$ per Co which was higher than LDA value ($1.76\mu_B$) presented

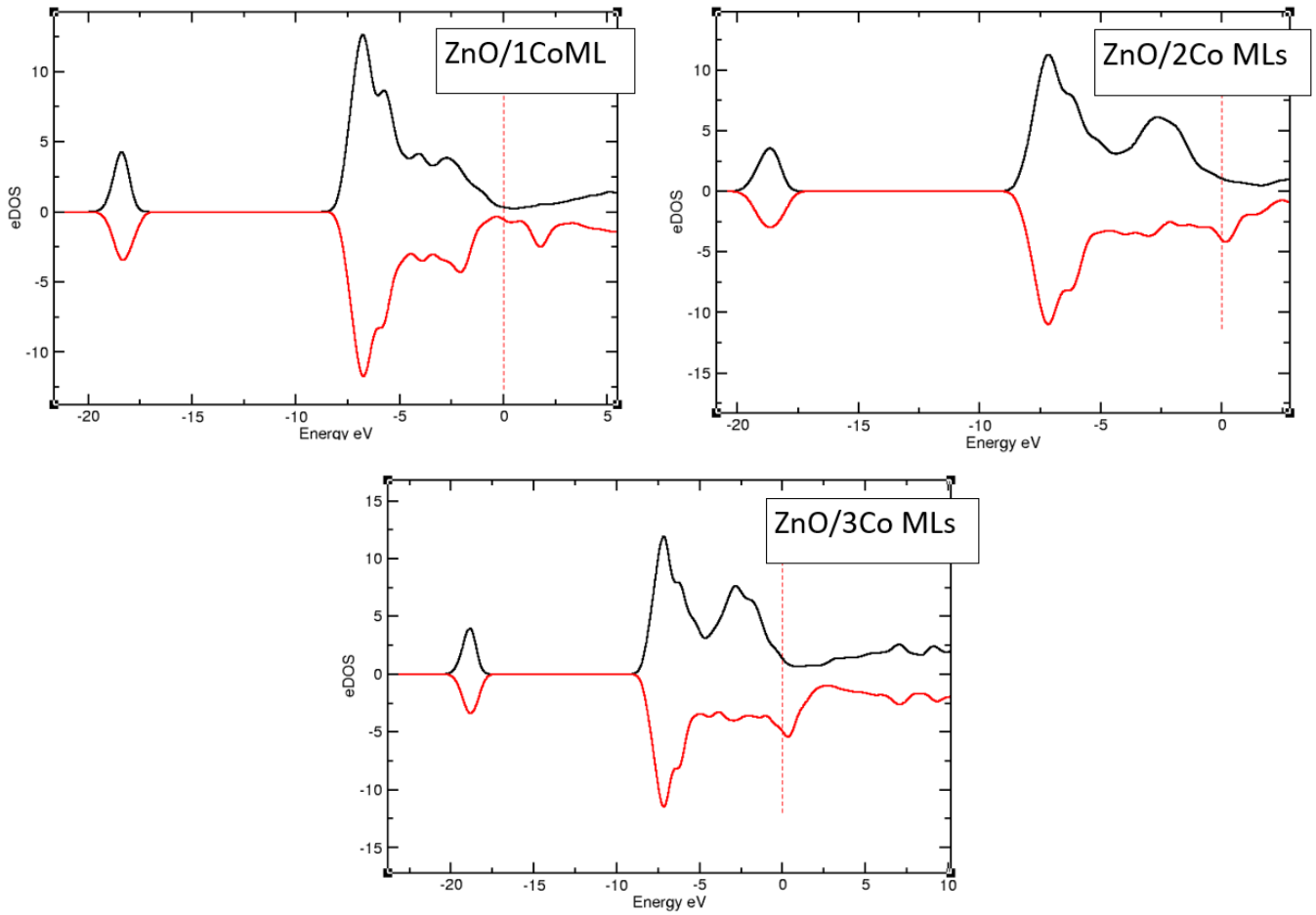

Figure 5.23: LDA +U calculated DOS for Co/ZnO system in the hco phase for one to three MLs from left to right. Energy was scaled to Fermi level.

in section 4.4.1 A, table (5.1), due to the increased splitting between the empty and filled orbitals of d-band. Therefore, the individual moments of the Co layers were higher than those obtained by LDA as Figure (5.21) shows compared to Figure (5.17). However, the pattern of the charge transfer was the same as that in LDA results transferring from the O-interface towards the other end. The magnetic moment of the Co layer which is adjacent to the O-layer had higher magnetisation than bulk due to d-band narrowing. The FM coupling preference between Co ions in the first A layer was confirmed by the resulting bond angles between Co and O ions at the interface. The measured angles for the relaxed systems were 108°, 102°, and 107 ° for systems with n=1 to n=3, respectively.

The magnetic moment of the cobalt layers decreased gradually from O-end to Zn-end which was reflected in the slow decrease of the total magnetisation with increasing n_{Co} as shown in Figure (5.22). The oxygen layer was also positively polarised, however with higher magnitudes than those obtained by LDA. Figure (5.23) shows the calculated DOS of the hcp system up to three layers using LDA+U method. Comparing to Figure (5.18), the overall increase of the splitting between the filled and empty orbitals can be clearly distinguished.

Magnetic interactions between the modelled NPs in the hcp phase were also investigated using LDA+U method. The magnetic exchange energy was calculated only for three monolayers stacks in the FM and AFM alignments. The calculations confirmed the ferromagnetic coupling between the monolayers with a magnitude $\Delta E_{(AFM-FM)} \sim +\ 150$ meV which six times larger than thermal energy at room temperature. The important result is the type of the coupling which was the same as that calculated using LDA in both Co phases.

Magnetisation of Co/ZnO system; fcc cobalt

Similarly, magnetisation of the Co/ZnO system was also investigated in the fcc cobalt for different number of Co layers. The results of the calculation are presented in Figure (5.24) with the magnetic moments labelled on each magnetic layer. The magnetic polarisation of the oxygen layer was higher than the equivalent systems with the hcp cobalt. The magnetic moment, however, depended on the Co-Zn interfacial layer where the highest moment occurs if the layer was C type as in the three MLs system, and it slightly dropped if the layer was A as in the four, and the lowest moment occurred if the interfacial layer

Figure 5.24: The change of the magnetic moment (in μ_B) and the charge (in e (bold)) of the Co/ZnO system with the fcc Co structure with the change of the number of the Co layers from one to six.

was B as in the five MLs case. The magnetic moment of the Co layer at the Co-O interface also depended on the other interfacial layer, where the highest value was if the terminated layer was A as in the four MLs system, in which the magnetic moment of the Co-O interfacial cobalt layer is (1.97 μ_B) which was higher than the bulk value (1.87 μ_B) similar of having only one ML. However, it was (1.83 μ_B) slightly lower than bulk value when the termination was C as in the three MLs system, and even lower (1.60 μ_B) when the cobalt terminated with B as in the five MLs. Comparing this interfacial layer with that of hcp cobalt, it can be found that the magnetic moment of fcc interfacial layer was much higher than that of the hcp. Similar to hcp structure, the Co-O-Co angles at the interface

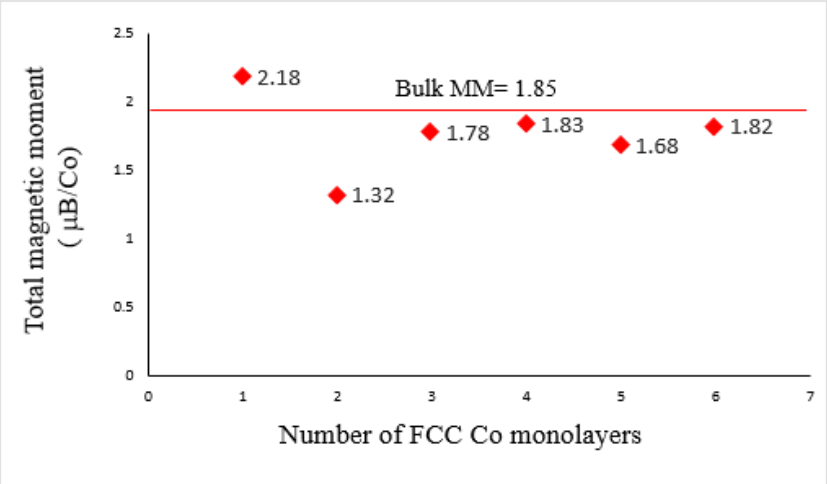

Figure 5.25: The total magnetic moment of the Co/ZnO system as a function of the fcc cobalt monolayers relative to the distorted bulk value.

of the relaxed structures were 123°, 109°, 107°, and 109° for n_{Co} =3 to 6, respectively and hence the interfacial Co layer is ferromagnetic. The trend of the magnetic moment of the cobalt layers was similar when there were three and four cobalt layers where the magnetic moment started with high value at the Co-O interface and decreased slightly towards the other end. However, for the five monolayer stack, the magnetic moment of the three layers were the same and increased slightly for the last two layers.

Figure (5.25) shows the total magnetic moment of the Co/ZnO system with the fcc cobalt. Because of the higher magnetic moment of the oxygen and its adjacent cobalt layer of the fcc than those of the hcp structure, the total magnetic moment of the former was generally higher than that of the latter for all number of layers considered. However, there was a small fluctuation between the total magnetic moment of the fcc depending on the Co-Zn interface layer giving the highest magnetisation to the four layers system whereas the three and the five layers systems had slightly lower total magnetisation. Similar to hcp system, this total magnetic moment fluctuation is expected to continue till

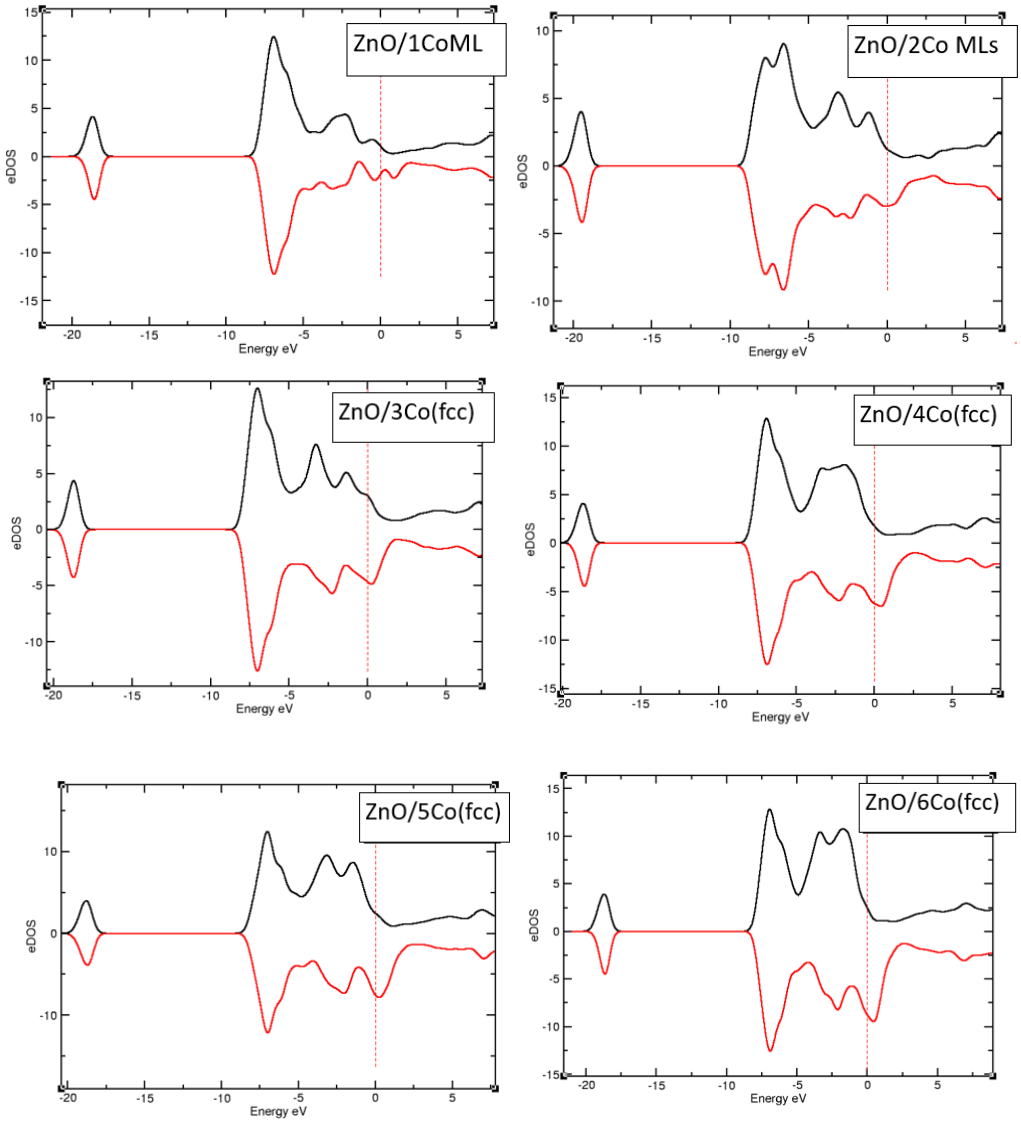

Figure 5.26: Calculated DOS for Co/ZnO system in the fcc phase for one to six MLs from left to right. Energy was scaled to Fermi level; $E_F = 0$.

the bulk value is averaged over when a very large number of cobalt layers is considered. The DOS plots of the Co/ZnO system in fcc cobalt structure are shown in Figure (5.26). Similar to the DOS plots of the hcp cobalt, the main features are the metallic signature and the change of the total DOS with increasing the number of the Co layers.

The magnetic exchange energies were also calculated for fcc Co using two blocks of six monolayers separated by two ZnO unit cells, Figure (5.13). The result of the energy

difference ($\Delta E = E_{AFM} - E_{FM}$) was + 71 meV per supercell which indicates that the coupling was also ferromagnetic for fcc Co phase with similar strength as that in hcp.

5.5 Conclusions

In order to investigate the Co NPs in ZnO, the Co metallic cluster was modelled as a multi-monolayer structure sandwiched in the ZnO matrix in the [0001] direction. The multi-layer system was stacked in two different phases; hcp, in the [0001] direction, and fcc, in the [111] orientation. Comparing the ground state energy of the fcc and hcp structures in ZnO with same number of cobalt layers, it was found that the preference depended greatly on the interfacial cobalt layer at the Zn side. The system was more stable in the hcp structure for the five and six monolayers, where it was slightly favourable in the fcc when four monolayers were present in the system. However, for the three monolayers, the system can be in either phase if the choice was between the A and C layers as an interfacial layer at the Co-Zn interface. This indicates that the probability of forming the hcp structure is higher in ZnO matrix with a very good agreement with the experimental reports [25, 120, 124].

For hcp cobalt phase, the oxygen layer at the interface was slightly polarised in the same direction as the modelled NP. The total magnetic moment of the Co/ZnO system fluctuates up and down between the even and odd number of the cobalt layers, respectively. This variation between the even and odd cobalt layers was due to the stronger magnetisation of both cobalt interfacial layers in the even-layer system. The fluctuated value increased with increasing the number of Co layers, and it is expected to continue

to increase till the bulk value is reached. For fcc cobalt structure, however, the magnetic moments of the interfacial oxygen layers were higher than their equivalent layers in hcp Co/ZnO system, and their magnitude depended on the cobalt layer at the Co-Zn interface. The magnetic moment of the oxygen layer was maximum when cobalt terminates with C layer, and slightly lower if the Co at the Co-Zn interface was A-type, and lowest when it was B-oriented. Thus, the total magnetic moment varied slightly depending on the Co-Zn interfacial layer being A, B or C and it also fluctuated just below the bulk values. Therefore, at very large number of cobalt layers, the total magnetic moment is expected to be averaged to the bulk magnetisation. The latest result showed that the magnetisation at low temperatures, ~ 5 K, due to metallic Co in ZnO can be safely estimated by their fraction with respect with the dopants, the doping percentage, and the bulk magnetisation value as it has been implemented in literature [24, 27]. The Co ions at the O-interface in both phases were found to be ferromagnetic, and this was confirmed by the measured Co-O-Co angles which all were closer to 90° than 180° and hence ferromagnetic coupling is the preferable exchange interaction. The latter result agrees with what has been found in the literature for one Co monolayer adsorbed on different polar ZnO surfaces [127]. It is an important result since it implies that no antiferromagnetism is expected at the Co NP surface. For both Co phases, the calculations showed that when Co nanoparticles are precipitated in ZnO matrix, the interfacial layer, between Co and ZnO matrix, was spin-polarised which agrees well with the proposed picture of Co NPs in ZnO in [28]. Although in our model, the ZnO matrix was not doped with Co, the model can still show a spin-polarised interfacial region. The interfacial magnetic semiconductor part was crucial in providing large tunnelling magneto-resistance (MR) effect and high spin polarisation where it helps the tunnelling electrons to overcome the conductivity

mismatch between the metallic Co NPs and the semiconductor matrix.

An important finding of this study is that the magnetic coupling was found to be ferromagnetic in both cobalt structures with similar strengths using LDA as an exchange-correlation functional. The ferromagnetic coupling was further confirmed by LDA+U calculations for three hcp Co layers. This is largely preferable in spin injection devices and spintronics applications in general. The obtained results were satisfactory and agree with the available experimental data and hence, this provides a confirmation of the validity of our model.

Chapter 6

Effect of Co-dopants on magnetism of Co nanoparticles in ZnCoO

6.1 Introduction

In the previous chapter, Co nanoparticles were modelled in pure ZnO by multilayer stacks in two different phases, hcp and fcc. The magnetisation of the individual layers was investigated and the ground state of the modelled nanoparticles was found to be ferromagnetically coupled with the antiferromagnetic state lying $\sim$ 70 meV higher in energy in both Co phases. In experiments, Co nanoparticles are always accompanied by Co ions on Zn sites in the ZnO lattice. In fact, the NPs are secondary phases formed as a result of doping. In this chapter, to make the model more realistic, the dopants are added in the ZnO lattice to study the change on the magnetisation and the coupling of the nanoparticles in two different ways.

This chapter is divided into four main sections. In section 2, a review of the magnetic properties of Co-doped ZnO films and crystals is presented in an attempt to link our results to what have been reported in the literature. Section 3 contains the results of the calculations; the computational details are presented at the beginning of the section. Finally, the main conclusions of the work are given in section 4.

6.2 Previous work

There are various sources of magnetisation in Co-doped ZnO samples. These include nanoparticles, which are the focus of our model, spin polarised point defects, grain boundaries, and surface states. These different sources can be induced by different preparation conditions and post-growth treatments. In this section, a brief review of the magnetic properties of Co-doped ZnO samples containing Co nanoparticles is presented.

6.2.1 Magnetisation of ZnCoO thin films and crystals with metallic Co inclusion

This subsection reviews some of the experimental results for magnetisation of Co:ZnO with metallic Co contamination. Figure (6.1) shows magnetisation loops of ZnO doped with 5 at % of Co samples prepared by PLD under low oxygen pressure using different target precursors with fractions of 24, 9 and 10 at % of the Co in the metallic state for samples A, D, and E, respectively [24]. The samples exhibit larger magnetisations and coercive fields at 5 K than the values expected for nanoparticles with nanometre size for Co:ZnO thin films which indicates that there is another origin of magnetism in

these samples. The very weak magnetisation of sample A at 300 K indicates that the nanoparticles are small, < 2 nm, and hence their moments are not saturated in a field of 1 T.

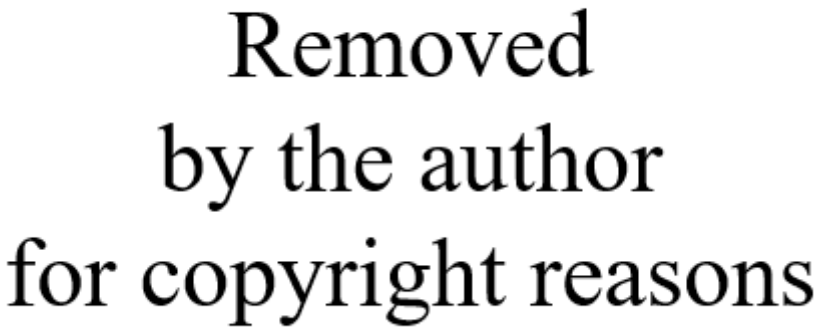

Figure 6.1: M-H loops of Co:ZnO samples prepared by PLD with metallic Co inclusion exhibit a large temperature dependence of the magnetisation. The inset is a zoom of t he coercive fields at 5K, adopted from [24].

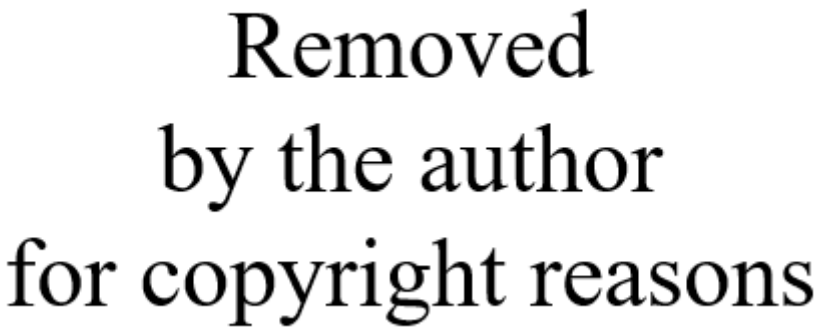

Figure 6.2: M-H loops of Co:ZnO samples with metallic Co inclusions at RT showing an increase in the magnetisation after annealing and decreasing the thickness x, of the deposited ZnO layer in Co:ZnO amorphous films, adopted from [70].

In Figure (6.2), the $M - H$ curves are shown for amorphous films made from sputtered Co/ZnO multilayers [70]. The ratio of the metallic to the semiconductor content, R, is

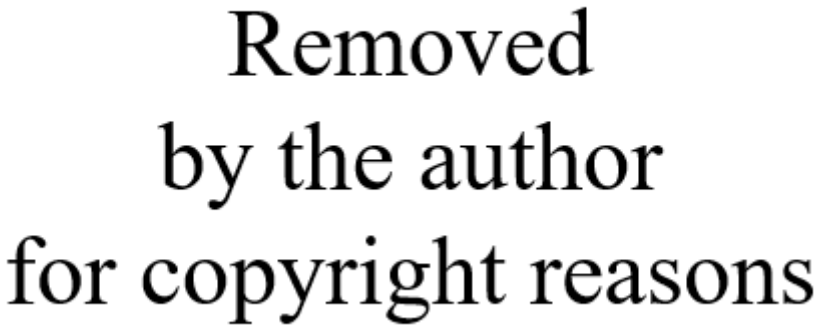

Figure 6.3: M-H loops of Co:ZnO sputtered amorphous samples with metallic Co inclusions showing an increase in the magnetisation with adding Al with ratio R equals to (a) 3:5 and (b) 1:5. The ZFC-FC magnetisation curves Co/ZnO (c) and Co/ZAO (d) for R=3:5 in 100 Oe field, the diamagnetic contribution from the substrate was subtracted; the Curie-Weiss fittings to the high-temperature regions are indicated by the dashed curves, adopted from [28].

3:2 for sample (a), while it is 1:5 for sample (b). This indicates larger metallic clusters in sample (a) than those in (b). The magnetisation results indicate a strong dependence on the thickness of the ZnO deposited layer, x. Therefore, the magnetisation for sample (a) is larger than that for (b) for the as-deposited and the annealed cases. Additionally, the magnetisation and coercivity largely increases with annealing for both ZnO thicknesses which is an indicative of increasing the fraction of the metallic Co in these samples after annealing. The highest saturation magnetisation for all cases was about 1 μ_B/Co for the case of x=0.4 nm annealed sample.

Figure (6.3) shows that the magnetisation also depends on the ratio R in the same pattern as in Figure (6.2) when it is compared for two ratios; namely 3:5 and 1:5 in samples (a) and (b), respectively. Furthermore, for both samples, the magnetisation has enhanced when Al is added which has been also observed in [27].

6.2.2 Magnetic exchange of Co nanoparticles and Co dopants in ZnO

(a) Theory

Magnetic exchange of Co nano-clusters have not been studied extensively in the literature. Nevertheless, in this subsection, a brief review of the main work which has been reported so far is presented. In addition, the exchange between the Co dopants is also presented in order to obtain an overview of possible effects of the dopants on the ferromagnetic exchange between the Co NPs in pure ZnO found in the previous chapter.

Figure 6.4: Co-dopant positions in (a) Zn-terminated and (b) O-polar wurtzite polar ZnO with with pseudo-hydrogen atoms [128].

The position of Co dopants have been tested in Zn- and O-polar ZnO by DFT as shown in Figure (6.4) [128]. It has been found that the dopants energetically prefer the outermost Zn layer for substitution for both polarities, Zn and O. Moreover, the energy increases with increasing the depth of the Co ion within the ZnO lattice. Additionally, the magnetic interaction has been also investigated. The exchange coupling between the dopants has been found to be antiferromagnetic in the near configuration; between $Co_{1,2}$,

$Co_{3,4}$, and $Co_{5,6}$ pairs, in both polar ZnO supercells. The theory of an adsorbed monolayer of Co placed on top of both polar structures has also been studied. The position of the Co adsorbed atoms have been shown to depend on the polarity of the ZnO. Co atoms energetically prefer the H_3 site for the O-terminated structure, whereas in a Zn-polar supercell, the atoms energetically prefer be positioned in the T_4 site as shown in the previous chapter. The magnetic coupling between a pair of adsorbed Co ions has been found to be ferromagnetic in both polarities.

The magnetic interactions in transition metal doped ZnO with the dopants in two different configurations, near and far as shown in Figure (6.5), of the dopants have been calculated by first principles [105]. The near configuration, Figure (6.5)(a), has been found to be more energetically preferable for all transition metals except Mn, where the energies of the two configurations were equivalent, as shown in Figure (6.6). The difference in energy was $\Delta E \sim 50$ meV for Co. The magnetic interaction between the dopants have been shown to depend on whether the system had been relaxed, and on the configuration of the transition metals, being far or near. Adding Hubbard U to the calculations has changed the magnetic coupling between the dopants in most cases, as shown in Figures (6.7) and (6.8). The exchange has been found to be ferromagnetic and weakly antiferromagnetic in the near and far arrangements, respectively using LDA. However, adding the Hubbard U term has shown to reverse the interaction completely to antiferromagnetic in the near and weakly ferromagnetic in the far arrangement of the TM. Furthermore, adding point defects has been shown to affect the type of the coupling between the Co dopants, where the coupling has shown to be AFM when oxygen vacancies or Zn interstitials have been included, whereas FM coupling has been shown to

be maintained when Zn vacancy has been formed.

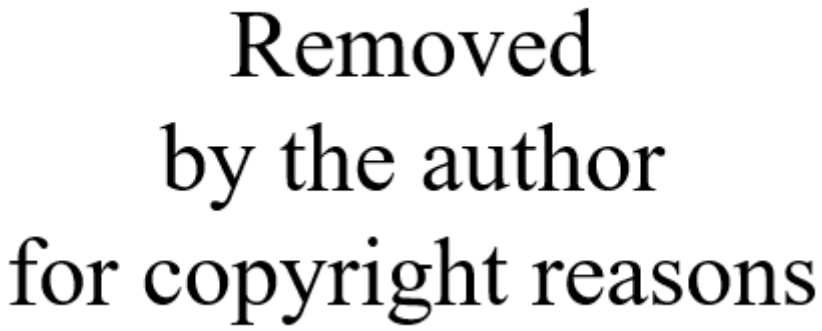

Figure 6.5: TM doping in ZnO in (a) near and (b) far arrangements [105].

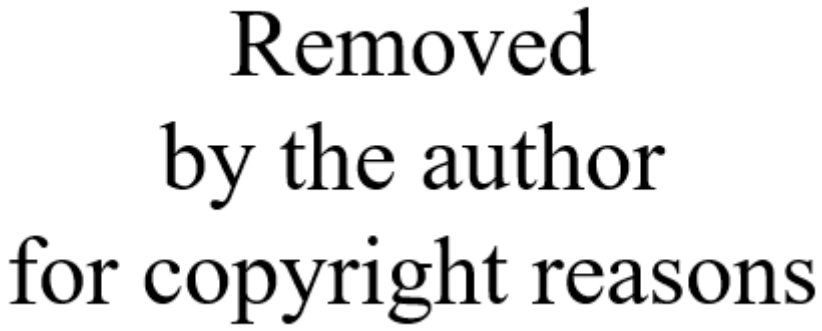

Figure 6.6: Energy difference between the near and the far configurations for different transition metals in TM-doped ZnO [105].

(b) Experiment

In an experimental investigation of magnetic exchange between Co NPs in ZnO, three different PLD samples on a c-cut sapphire have been characterised and qualitatively compared [27]. The content of the metallic Co was about 7, $\sim$ 0 and 2 at % of the doping percentages which were 20, 14.5, and 25 at %, respectively. The first two samples were Co-doped whereas 0.6 at % of Al was included to the third one. The first and the third samples were characterised with temperature dependent magnetisation and relatively high

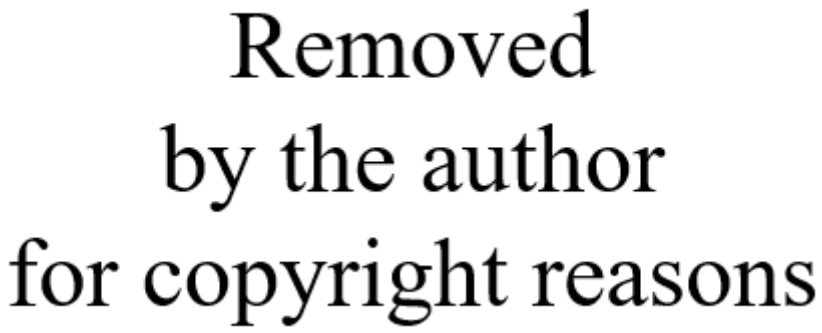

Figure 6.7: LDA calculations of the magnetic exchange energy difference for the (a) near and (b) far configurations. Filled bars represent the un-relaxed systems, and the unfilled bars represent the case when the internal coordinates were fully relaxed [105].

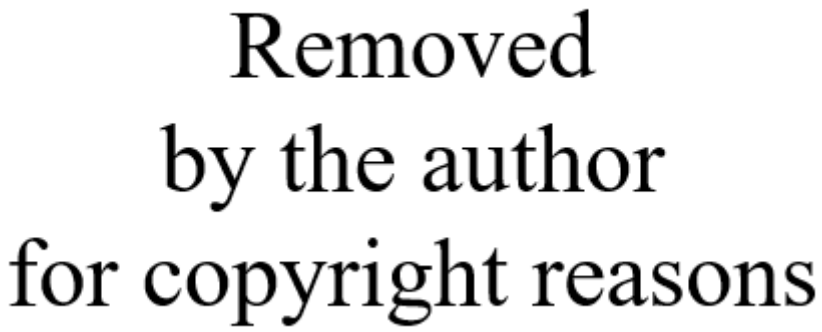

Figure 6.8: LDA + U calculations of the magnetic exchange energy difference for the (a) near and (b) far configurations. Filled bars represent the un-relaxed systems, and the unfilled bars represent the case when the internal coordinates were fully relaxed [105].

.

coercive fields typical for any nanoparticle dominant magnetisation. The second sample, however, has been characterised with small coercive field and almost temperature independent magnetisation typical for defect-induced ferromagnetism. In addition, the magnetic exchange between the nanoparticles in the first sample has been found to be antiferromagnetic, whereas adding Al has changed the coupling into ferromagnetic due to the

extra carrier. By fitting the the ZFC-FC curves to the Curie-Weiss law at high temperatures Figure (6.3) (c,d), the exchange has been found to be antiferromagnetic between the nanoparticles in Co:ZnO samples, whereas the ferromagnetic ground state energy has been found to be lower when Al has been included.

6.3 Present work

6.3.1 Computational method

System details

Method I The supercell of pure ZnO with one Co ML was adopted from previous calculations, from Chapter 5, and used as a seed cell to be doped with Co. The two vertical unit cells were repeated twice in the y-direction to obtain a $1 \times 2 \times 2$-ZnO supercell with one Co monolayer at the top. This resulted in eight Zn and eight O atoms in the supercell. Substituting one Zn atom with Co lead to a doping percentage of 12.5 at % which is an experimentally reasonable concentration. The whole supercell with one Co ML and 12.5 % doping was geometrically relaxed keeping the volume constant. The position of the Co-dopant was varied in the third and fourth Zn layers and the total energies of the supercells were compared. Additionally, the O and Zn positions were swapped and the total energies were calculated and compared.

Method II In the second method of treating the system, the ZnO pure cell was repeated to construct a $1 \times 2 \times 2$-supercell and doped with 12.5 at % of Co in the fourth layer of Zn.

The supercell was geometrically relaxed with changing the volume in order to obtain the optimum volume after doping. The relaxed Co-doped ZnO supercell was adopted and Co MLs were added and each time the supercell was geometrically optimised with constant volume.

In both methods, the dopants are added in such a way so that they were separated only by an oxygen ion which means the doping configuration is adopted in the near arrangement as shown in Figure (6.5 a).

In both methods, the doping position of the supercell is repeated in the system by symmetry which is not experimentally true since the doping positions are random and do not necessarily repeat in the same pattern. However, the model can still be used and give good results compared to experiments.

Computational details

The total energy and electronic structure calculations were performed using Kohn-Sham [87, 88] formalism of density functional theory as implemented in the CASTEP package [135]. The default CASTEP(18.1) potential was used with valence electrons for Zn $(3d)^{10}(4s)^2$, $(2s)^2(2p)^4$, for O and $(3d)^7(4s)^2$ for Co. A cutoff energy of about 1000 eV for plane wave expansion was used. Integration in the reciprocal space was implemented using the Monkhorst-Pack sampling of the Brillouin zone, and k-point mesh of 10×5×2 and 10×5×1 Gamma-centred Monkhorst-Pack method [107] for calculating the magnetisation and exchange energies, respectively. The very high cutoff energy and the fine k-point grid were implemented due to the sensitivity of the magnetic interactions

to the convergence quality [136].

For all geometry optimisations of the Co/ZnO systems of different number of Co MLs, the volume was kept constant and all the internal coordinates were relaxed until Hellmann-Feynman forces were less than 0.001 eV/Å. A Gaussian smearing technique with 0.05 eV width was applied to enhance convergence but all energies presented in the following were obtained by extrapolating to zero smearing.

The exchange-correlation functional was approximated with the Local Density Approximation (LDA). Furthermore, a spin polarisation scheme was adopted and applied for all Co atoms in all calculations.

6.3.2 Results and discussion

Co-doping in ZnO

General properties In the second method to treat the system, the ZnO supercell was doped with Co before any Co MLs were added. Since the system is an insulator, it was treated with a U= 4 eV term as well as U=0 on the d-orbitals of the Co-dopants. The main results of such calculations are presented in Table (6.1). Compared to the pure ZnO lattice constants obtained in the previous chapter, a= 3.19 $\mathring{A}$ and c= 5.15 Å, it can be seen that the doping leads to increasing the lattice constant c in both cases which agrees with the experimenatlly observed increase of the lattice constant after Co doping [24]. For a and b, however, they were smaller after doping using LDA, and slightly larger when U= 4 eV was added to the calculations as it was expected. Hence, the relaxed volume

using LDA +U was larger than the corresponding volume using LDA alone. On the other hand, the total magnetic moments of the two supercells were the same although the magnetisations of constituents were slightly different as will be shown.

	U= 0	**U =4 eV**
lattice constant a **(Å)**	3.13	3.19
lattice constant b **(Å)**	3.18	3.20
lattice constant c **(Å)**	5.17	5.19
Volume($\mathring{A}^3$)	180	184
Total magnetic moment μ_B**/Co**	1.00	1.00
Ground state energy per supercell (eV)	-18844.67	-18842.07

Table 6.1: Results of lattice constants, magnetic moments and ground state energies of Co-doped ZnO supercell with U=0 and U=4 eV.

Distribution of magnetic moments Figure (6.9) shows the results of the distribution of the magnetic moments on atoms in the supercell for LDA and LDA+U. As it is well known, adding Hubbard U term on d-orbitals of Co leads to a higher magnetic moment on Co, 1.11 μ_B compared to 0.90 μ_B. However, the positive magnetic polarisation on

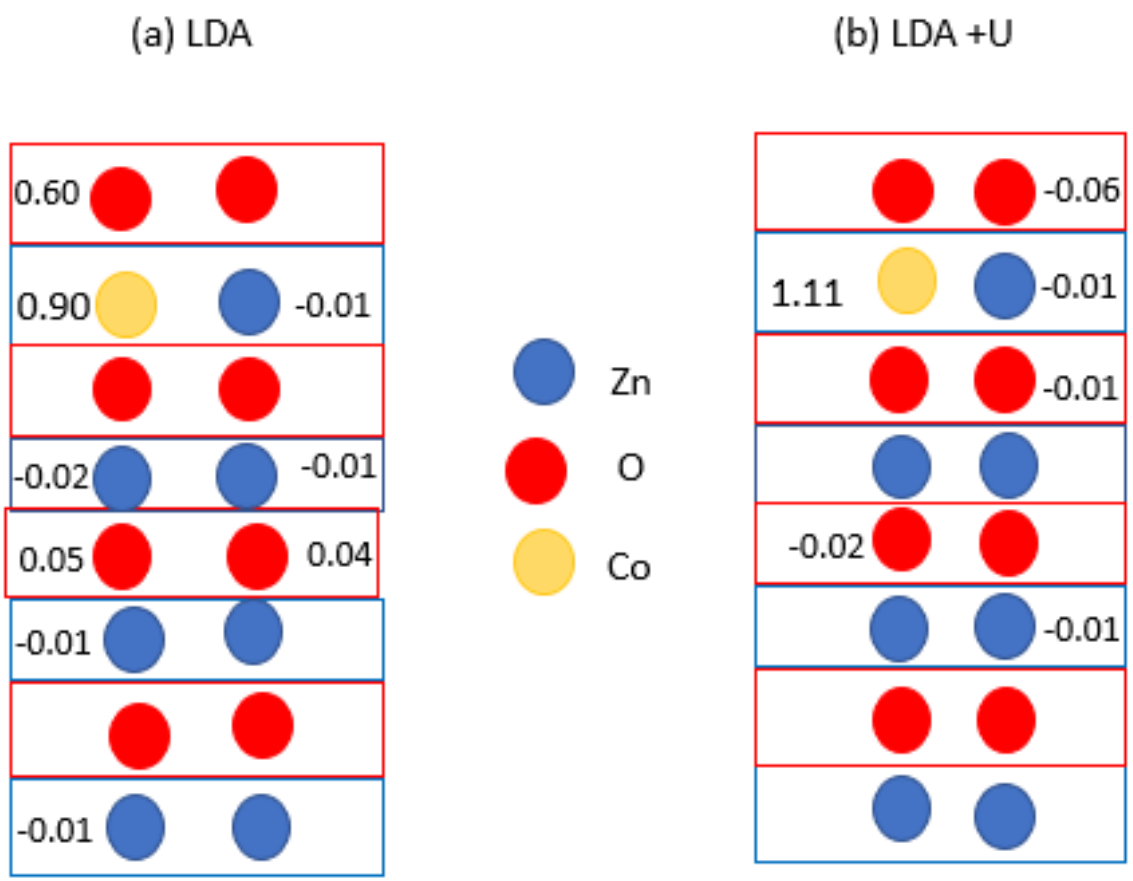

Figure 6.9: Distribution of magnetic moments on the atoms in the Co-doped ZnO supercell composed of two ZnO unit cells using (a) LDA, and (b) LDA+U.

some oxygen atoms due to charge perturbation was changed to negative when Hubbard U was added, Figure (6.9 b) compared to (6.9 a). This may be due to the AFM coupling between Co ions when U was added compared to the FM coupling when U=0 as it has been shown by Gopal et *al* [105]. The calculated DOS plots of the system in the two cases are presented in Figure (6.10). The two plots are very similar. However, the only difference is the increasing the exchange splitting of the d-band of Co at Fermi level when Hubbard-U term was added.

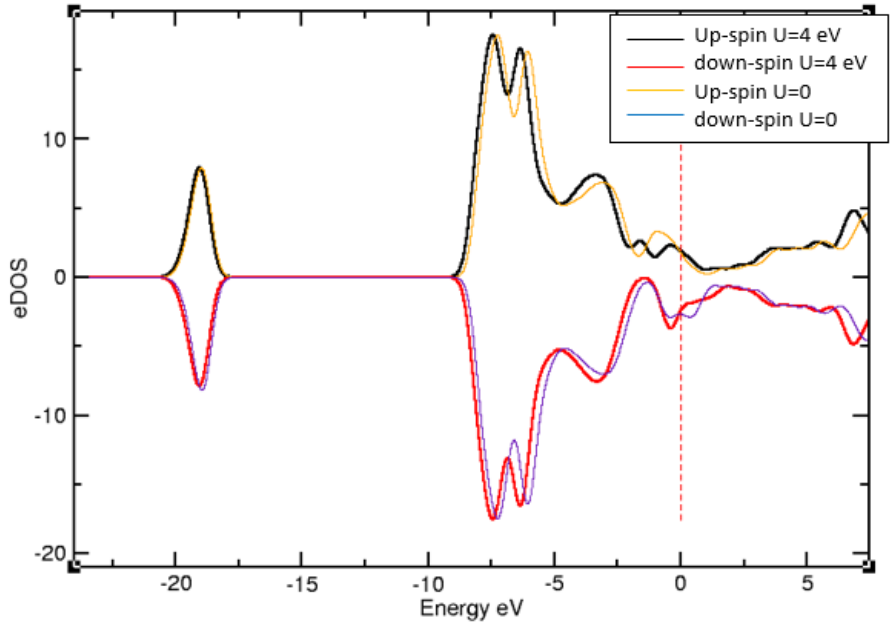

Figure 6.10: DOS plots of Co:doped ZnO with U=0, and U=4 eV.

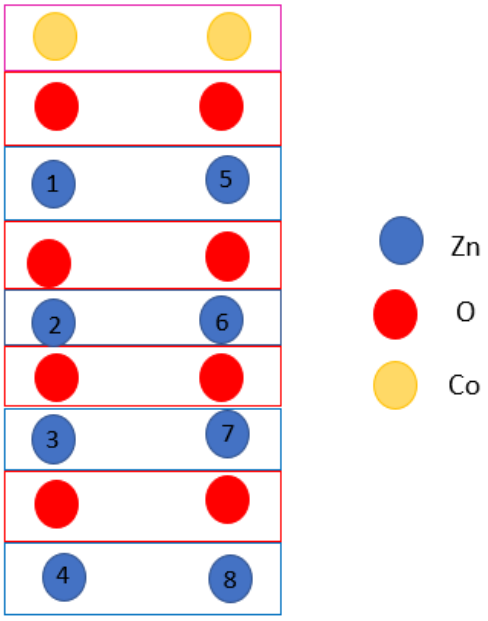

Figure 6.11: A sketch of one Co layer on top of two ZnO unit cells. The numbers on the Zn atoms show the possible substitutional positions of Co atoms refered in the text.

Effect of changing Co dopant position on ground state energy

In the presence of one Co ML ad using method (I) mentioned above, the Co position was tested between 1 and 2 in the third and fourth Zn layers as shown in the sketch in Figure

(6.11). Positions 5 and 6 are equivalent to 1 and 2, respectively because of symmetry. The energy difference between the supercells when Co was place in position 1 and 2 was about $\Delta E = E_1 - E_2 = -0.25$ eV. This gives an energy preference for Co dopant to be placed in position 1 over position 2 with an agreement with the test performed in [128] for pure ZnO with different polar surfaces. Therefore, position 1 was adopted for the dopant for all following calculation with adding extra Co MLs at the top of the doped supercell.

Effect of switching oxygen and zinc positions in the ZnO lattice

The coordinates of oxygen and zinc atoms were swapped in Figure (6.11) so that the fourth Zn layer is immediately adjacent to Co layer. The dopant was placed in the position of one of Zn atoms in that layer, position n. The energy of the supercell was calculated and compared to that with Co in position 1. The energy of the system with the Co being immediately adjacent to the Co ML was lower. The energy difference was $\Delta E = E_n - E_1 = -0.46$ eV, however, this arrangement corresponds to Co NP with a rough surface as Co atoms prefer to be clustered together. Thus, this arrangement, even though it is lower in energy than that with position 1, the system does not correspond to what we are trying to model.

The effect of Co dopants on the magnetisation and the coupling of the Co nanoparticles

A. Magnetisation of one Co monolayer system

The calculated magnetic moments and charges of each Co ion as well as the interfacial Zn and O for one Co monolayer are shown in Figure (6.12). The magnetic moment of the

(a) Method I

0.01	*-0.76*	**0.00**	*-0.76*
-0.05	*+0.20*	**-0.06**	*+0.18*
1.84	*+0.41*	**0.02**	*+0.49*
0.18	*-0.58*	**0.29**	*-0.64*
1.78	*+0.43*	**0.01**	*+0.89*

Zn

Co

O

(b) Method II

0.01	*-0.75*	**0.00**	*-0.76*
0.00	*+0.22*	**-0.05**	*+0.17*
1.23	*+0.35*	**1.53**	*+0.42*
0.20	*-0.63*	**0.11**	*-0.56*
0.23	*+0.52*	**0.02**	*+0.90*

Figure 6.12: Magnetic moment (in bold, left-hand side) and charge distribution (in italics, right hand side) on Co and interfacial Zn and O ions calculated for one Co ML from methods (a) (I) and (b) (II) described above.

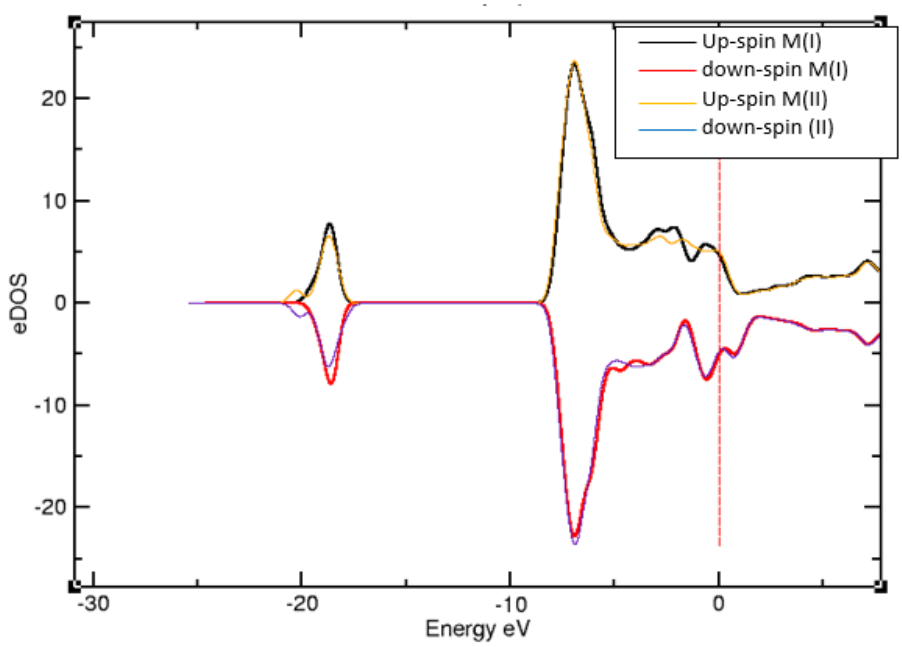

Figure 6.13: DOS Plots for one Co ML sandwiched within Co-doped ZnO supercell calculated from methods (I) and (II) described above.

substitutional Co ion has a very different value of the magnetic moment in each method, it carries 1.78 μ_B in results of method (I) whereas it has much less value of 0.23 μ_B using method (II). The magnetic moment values of the Co ions in the monolayer are also different. In results of method I, the Co ion that is close to the substitutional has a value larger than bulk 1.84 μ_B, whereas the farther ion has a vanishingly small moment, 0.02

μ_B. In method (II), the values are more reasonable as the closer to the substitutional has a slightly lower value than adjacent ion in the monolayer, as the close Co ion carries a magnetic moment of 1.23 μ_B and the far ion has a value of 1.53 μ_B. The oxygen atoms are also positively spin polarised using both methods as it has been found in the previous chapter for Co NPs in pure ZnO with slightly higher values in results of method I. Additionally, there are small negative spin perturbations on Zn ions as previously found. These all moments result in a total magnetic moment of values of 1.33 and 1.11 μ_B/Co for systems using methods I and II, respectively. The results also showed that the ground state energy of the supercell using the second method is lower than that calculated using method (I) by an energy difference ΔE = 42 meV. The charge transfer path was similar to that found for Co NPs in pure ZnO from the oxygen and its adjacent Co layer at the O-Co interface to the other Zn interface by comparing charges of Zn and O ions to bulk charges in ZnO which are $\pm$ 0.80, respectively. Figure (6.13) shows the DOS plots of the one Co layer system using the two methods.

B. Magnetisation of two and three Co systems

Magnetisation of the two and three monolayers stystems were also investigated using method (II) since it gave a lower energy for the one Co layer system. The calculated moments and charge on Co layers, Zn and O layers are shown in Figure (6.14). The results show a small magnetic moment on the substitutional Co in ZnO lattice for the two systems, with values 0.05 and 0.12 μ_{B}/Co for the two and three layer systems, respectively and positive charges as expected for the dopants. The magnetic moment distribution in the metallic stacks are fluctuating around the bulk Co magnetisation. The charges on the first Co layer at the oxygen interface are positive and those for the second and third layers are negative due to the charge transfer from the oxygen layer and its adjacent

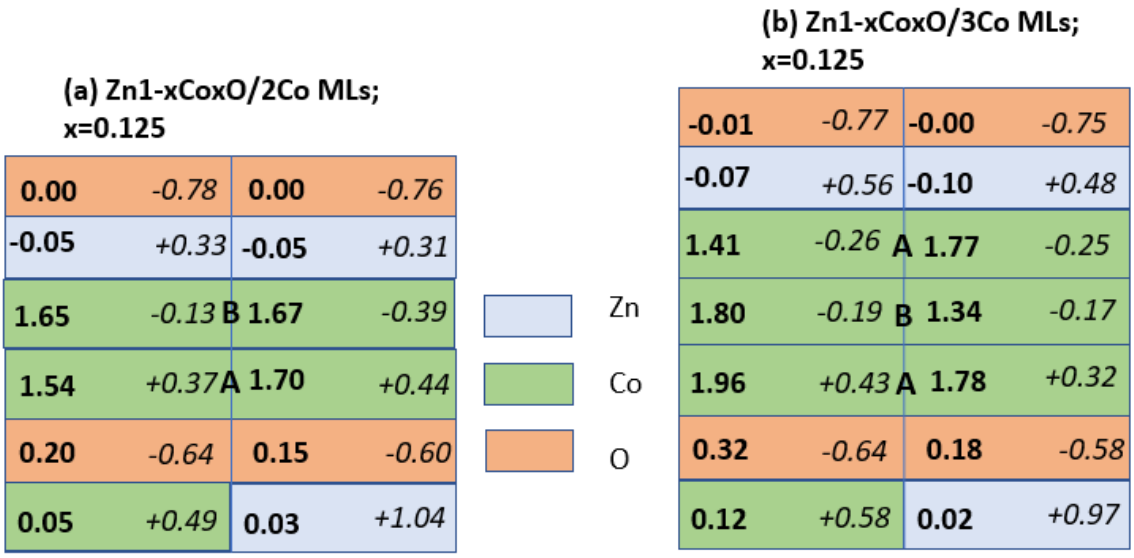

Figure 6.14: Magnetic moment (in bold font, left-hand side) and charge distribution (in italic, right-hand side) on Co layers and interfacial Zn and O ions calculated for two (a) and (b) three Co monolayers from method (II) with hcp Co stacking squence (A,B,..).

Co layer towards the other Co layers and the Zn interfacial layer. The negative charge values of the middle layer are the lowest which indicates the stabilisation of the middle layers towards bulk charge with adding extra Co layers. The total magnetisation for the two and the three layers stuctures are 1.37 and 1.50 μ_B/Co. An important result is the positive spin polarisation on oxygen ions at the interface for both systems as found in the pure system. There were also negative spin polarisations on Zn ions at the interface, however with smaller magnitudes than those on oxygen. It can be found that adding the dopant to the ZnO matrix makes the magnetic moment of the second layer higher in the two layers system compared to the corresponding un-doped system from the previous chapter. It also leads to a much higher average moment on the first layer for the three layers system. The positive spin polarisations on oxygen layer are similar in the two layers structures and much higher in the three monolayers system all when compared to their similar undoped structures. Again, the interfacial region is vital in device applications

since it gives rise to high values of magnetoresistnce since it bridges the conductivity gap between the metallic and the semiconductor region and hence they provide good systems in data storage devices (ReRAM) mentioned in Chapter 1.

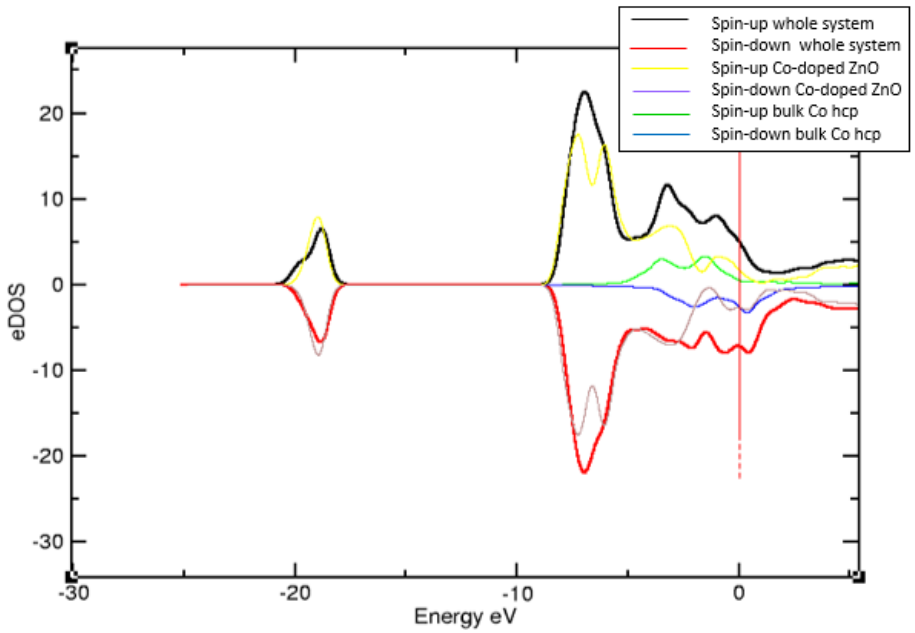

Figure 6.15: DOS Plot for two Co MLs sandwiched within Co-doped ZnO supercell calculated from methods (II) compared to DOS plots of Co-doped ZnO and bulk Co. Fermi energy was scaled to zero

The DOS plots for the two and three Co layers structures are shown in Figures (6.15) and (6.16), respectively. They both show an overlap of the DOS plots of the constituents to produce the total DOS of the two structures. They also clearly exibit the expected metallic feature at the Fermi level. In both DOS plots (5.15 and 5.16), the doped ZnO system should show a semiconducting behaviour, however since the supercell used in the calculation is small and the doped Co ions are separated with short distance which gives a high probability of electron tunnelling between Co ions and hence the Co-doped ZnO system shows small value of DOS at Fermi level. The d-band feature of the metallic Co

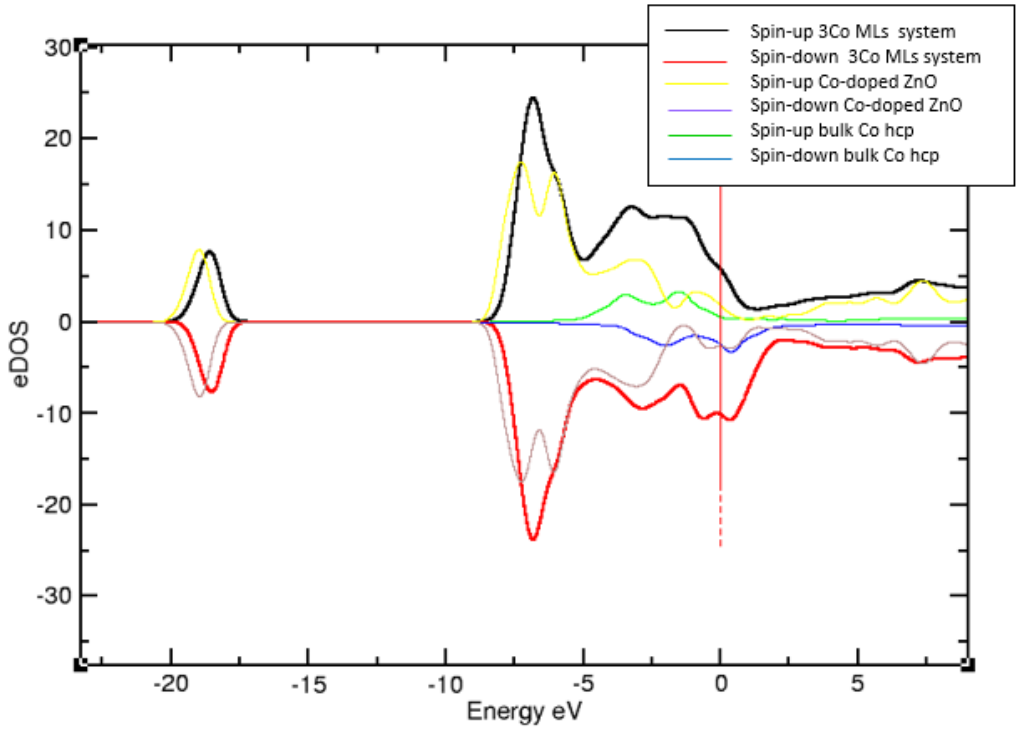

Figure 6.16: DOS Plot for three Co MLs sandwiched within Co-doped ZnO supercell calculated from methods (II) compared to DOS plots of Co-doped ZnO and bulk Co. Fermi energy was scaled to zero.

is strongly enhanced in the system with Co multilayers between 0 and 5 eV.

C. Magnetic Exchange between Co multilayers

The magnetic exchange interactions between the Co MLs with the presence of Co dopants in ZnO lattice were investigated as was done in the previous chapter. The exchange was calculated for two monolayers system. The difference in energy between the ferromagnetic and the antiferromagnetic alignments of Co MLs was found to be; $\Delta E = E_{AFM} - E_{FM} = -88$ meV per supercell. The sign of the difference indicates the presence of the antiferromagnetic exchange coupling of the Co layers for the system after doping which agrees well with what has been found in the literature [27, 28]. The magnitude suggests that the antiferromagnetic exchange may be stabilized at temperatures much higher than room

temperature.The exchange is here antiferromagnetic as we believe that the interactions in an insulator like ZnO are short range and hence similar to the strong AFM superexchange interaction expalined in Chapter 2 section 2.4.2.

6.4 Conclusions

The work in this chapter is a continuation of modelling Co NPs in ZnO by first principles presented in the previous chapter, however, the ZnO matrix is now doped with Co in two different methods. The first method which was doping ZnO supercell in the Co/ZnO structure for one Co layer. In the second method, the volume of the Co-doped ZnO supercell was relaxed first and then the Co monolayers were added and the system was relaxed in each with constant volume. Comparing the ground state energy of the two systems with one Co layer in each, the system using method (II) was lower in energy by an energy difference of 42 meV and hence was adopted for addition of extra Co layers.

The magnetic moment of the Co ions in the metallic stacks have reasonable values for all multilayered systems. The substitutional Co ions have very small magnetic moments compared to bulk value and to their calculated values in ZnO matrix without Co layers. The magnetisation values of those in the Co monolayer are slightly less than bulk for one and two systems, however, they were found to fluctuate around the bulk value in the three layers system. The total magnetic moment was found to increase with increasng the number of Co layers. There were 1.11, 1.37 and 1.50 μ_{B}/Co for one, two and three layers structures, respectively. The oxygen ions at the interface were found to be spin polarised in the same direction as the Co layers, whereas there were small spin perturba-

tions in the opposite direction on the Zn ions at the interface as it has been found in the undoped structure and which agrees with the picture proposed in [28] for the magnetic regions classification in Co-doped ZnO films with metallic Co. As it was mentioned in Chapter 5, the polarisation in the interfacial semiconductor is important in increasing the magnetoresistance values of the films.

The charge transfer path was found to be exactly the same as that in the Co/ZnO system from oxygen interfacial layer and its adjacent Co layer to the Zn interfacial layer and the other Co layers. Thus, adding more Co layers is expected to stabilize the bulk charge and magnetisation to bulk values and this happens faster for the middle layers.

An important finding is the exchange interaction which was calculated in the presence of the substitutional Co in ZnO lattice. The results showed that the antiferromagnetic exchange between the metallic Co layers is lower in energy. The magnitude of the coupling indicates that the exchange may be maintained at temperatures higher than room temperature which agrees well with what has been found experimentally [27, 28].

In summary, the addition of Co ions in the ZnO lattice has changed the charge and the magnetic moment distributions. The charge perturbation becomes higher and also the magnetic moment of the Co ions in the metallic layers compared to the corresponding system with no dopants. Additionally, the calculations showed that exchange interaction changed to antiferromagnetic when substitutional Co ions are included in ZnO lattice.

Chapter 7

Conclusions and future recommendations

7.1 Conclusions

The work presented in this thesis is divided into three main parts: the first part is concerned with characterising magnetic circular dichroism, (MCD), signals due to point defects in ZnO by means of quantum mechanical derivation of an equation that is proportional to the experimental signal. The second section was on modelling another source of magnetism in ZnO, namely Co nanoparticles with hcp and fcc structures embedded in pure ZnO lattice by density functional theory. In the third part of the thesis, the model of the Co nanoparticles in ZnO was made more realistic by adding Co dopants to the ZnO lattice and the magnetisation and the exchange of the system were calculated and compared to the corresponding systems without Co dopants.

An equation that gives a relative magnitude and sign of the expected MCD signals which originate from transitions involving point defects was derived by treating spin-orbit and Zeeman interactions on defect states in ZnO as perturbations. The equation shows that the relative strength is governed completely by the deviation of the g-factor from the free spin value of the defect. This theory was valid provided that the spin-orbit coupling is much larger than the Zeeman energy. Considering the three most common gap states reported in the literature, the strongest signal, according to the equation, may be due to Zn interstitial states which are shallow donor levels contribute to MCD signal at the band edge. Such MCD signals have been observed and reported in literature many times especially for samples prepared at low oxygen pressure conditions. The gap states due to vacancies are expected to produce slightly weaker signals in the middle of the band gap. However, according to the equation, the signals that arise from donor levels, such as Zn interstitials and oxygen vacancies, are expected to be negative whereas those that may be caused by acceptor states, such as zinc vacancies, are predicted to be positive. This is a very useful characterisation tool that gives us the opportunity to distinguish between transition that may have similar energy range. However, this comparison may be performed only after making sure that there is no secondary phases are present in the sample. The MCD signals of a number of Co-doped ZnO films prepared by PLD were studied and it was found that the magnitude of the positive signals observed in the middle of the band gap increases with increasing the saturation magnetisation values which means that the ferromagnetism observed is due to the defects causing such signals especially if the temperature dependence of the magnetism is weak.

A systematic DFT study using LDA as an exchange correlation functional of Co nanoparticles (NPs) in ZnO was implemented. The size of the NPs, which is measured in nanometres, is very large on an atomic scale. Furthermore, the reported shapes of the detected NPs in ZnO are either elliptical with the major axis in the [0001]-direction or spherical. Full three-dimensional DFT modelling of nanometre sized Co particles of various shapes is unrealistic, and so in this work, we focus on the interfacial region between the ZnO and the Co cluster. This enables us to model the system as a planar, multi-layer structure of Co sandwiched within ZnO slabs. The lateral size of the NP is also large on atomic scale so our approximation of assuming lateral periodicity should not affect the validity of our results. The nanoparticles were modelled as a multi-layered stacks sandwiched first within pure ZnO unit cells in the [0001] direction. The multi-layer structure was considered in hcp and fcc crystallisations in the [0001] and [111] directions, respectively. By comparing the ground states of the systems with both phases, it is concluded that hcp Co phase has higher probability of formation than fcc within ZnO which agrees well with what has been reported in the literature. The magnetisation of the sandwich structure with both phases was evaluated as a function of increasing the number of Co layers, and it was found that with an exception for the interfacial Co layers, the magnetisation and the charges of the other layers tend to bulk values which confirms the validity of the model. The calculations confirmed that there is no possibility of any antiferromagnetic interaction between the Co ions at the oxygen interface for both Co phases compared to bulk CoO which is antiferromagnetic. In addition, the oxygen ions in the interfacial semiconductor region were spin polarised in the same direction as the magnetisation of the metallic layers. This is important in technological applications in producing high magnetoresistance values and spin injection devices. The magnetic exchange interaction

between the modelled NPs are also investigated. The calculations showed that the ground state of the NPs is ferromagnetic with the antiferromagnetic state lying about 70 meV higher in both phases.

To make the previous model more realistic, since the nanoparticles are secondary phases produced under specific conditions, the ZnO lattice was doped with 12.5 at % Co and the magnetisations of the individual layers of Co and ZnO were calculated and compared with previous study for number of layers up to three. The magnetisation of Co ions in the metallic layers approach bulk magnetisation faster than for the corresponding pure structure. The results also showed that there was a magnetic semiconductor region at the interface as it was found in the pure Co/ZnO structure and which agrees well with experiments. The charge perturbations followed the same pattern as for Co in pure ZnO, however with larger magnitudes with the least magnitudes for the middle layers. The exchange interaction energies between the two Co monolayers stacks through the doped ZnO structure were also calculated and compared with the previous results. The calculations showed that antiferromagnetic exchange coupling between the metallic stacks is lower in energy which agrees well with what has been found experimentally for the exchange between the Co nanoparticles in cobalt-doped ZnO. The results showed that the magnetisation of the Co NP is equivalent to bulk values for large number of Co layers which is important in estimating magnetism due to metallic clusters in the system. Moreover, the model has justified the availibility of the interfacial magnetic region between the metallic cluster and the semiconducting host material. This region is vital in device applications since it results in high MR values and hence the samples can be used in DMS as spin injectors and in magnetic storage devices, ReRAM as it has been mentioned in

chapter 1.

Overall, the results of the MCD calculations gives an important tool to diagnosis the native point defects formed in ZnO samples when no other secondary phases are present. However, when the magnetism arises from secondary phases such as Co NPs in ZnO, the shape and the magnitude of the spectra is well modelled by Maxwell-Garnett theory in relation to the volume of the metallic cluster formed. Moreover, this study presents a model of Co NPs in ZnO and characterises its magnetisation and the possible magnetic interaction between them in which can not be extrapolated from MCD spectra. Therefore, the two theoretical studies give new results in an attempt to understand different sources taht may be responssible for ferromagnetism in ZnO.

7.2 Future work

This is a simplified model of Co nanoparticles in ZnO. To work towards improving the model, there are some future recommendations should be accomplished. These are listed as follows:

- In this model, two unit cells of ZnO in the [0001]-directions were used. It would be interesting to investigate the magnetic properties and the magnetic interactions of the modelled NPs after increasing the number of the ZnO unit cells in this direction.
- The Co doping percentage, 12.5%, which was used in this model, was reasonable compared to experiments. However, investigating the effect of decreasing the doping percentage, which will require larger supercells, on the magnetic properties of the

system is an other objective should be followed to deeply understand the magnetic behaviour of the system.

- Adding Al to the ZnO lattice in small concentrations $\sim$ 1 at % is an important goal towards understanding the effect of adding extra carriers to the system on the system magnetisation and the exchange between Co NPs in order to explain the experimental data.

- Adding different defects in ZnO to the model, e.g. vacancies or Zn interstitials, and investigating how the magnetic properties change is another point should be achieved in order to gain a deep insight into the magnetisation behaviour of the system.

- This investigation of Co NPs dispersed in ZnO was implemented in the [0001]-direction of ZnO. Other Co growth directions, such as Co hcp growing on (110) ZnO surface is highly recommended to be modelled.

Bibliography

[1] T. Tietze, M. Gacic, G. Schütz, G. Jakob, S. Brück, and E. Goering, "Xmcd studies on co and li doped zno magnetic semiconductors," *New Journal of Physics*, vol. 10, no. 5, p. 055009, 2008.

[2] P. Zhan, W. Wang, C. Liu, Y. Hu, Z. Li, Z. Zhang, P. Zhang, B. Wang, and X. Cao, "Oxygen vacancy–induced ferromagnetism in un-doped zno thin films," *Journal of Applied Physics*, vol. 111, no. 3, p. 033501, 2012.

[3] H. Hsu, J.-C. A. Huang, Y. Huang, Y. Liao, M. Lin, C. Lee, J. Lee, S. Chen, L. Lai, and C.-P. Liu, "Evidence of oxygen vacancy enhanced room-temperature ferromagnetism in co-doped zno," *Applied Physics Letters*, vol. 88, no. 24, p. 242507, 2006.

[4] H. Ren, G. Xiang, G. Gu, X. Zhang, W. Wang, P. Zhang, B. Wang, and X. Cao, "Zinc vacancy-induced room-temperature ferromagnetism in undoped zno thin films," *Journal of Nanomaterials*, vol. 2012, p. 6, 2012.

[5] G. Xing, Y. Lu, Y. Tian, J. Yi, C. Lim, Y. Li, G. Li, D. Wang, B. Yao, J. Ding, *et al.*, "Defect-induced magnetism in undoped wide band gap oxides: Zinc vacancies in zno as an example," *AIP Advances*, vol. 1, no. 2, p. 022152, 2011.

[6] B. Straumal, A. Mazilkin, S. Protasova, P. Straumal, A. Myatiev, G. Schütz, E. Goering, and B. Baretzky, "Ferromagnetism of nanostructured zinc oxide films," *The Physics of Metals and Metallography*, vol. 113, no. 13, pp. 1244–1256, 2012.

[7] B. B. Straumal, A. A. Mazilkin, S. G. Protasova, P. B. Straumal, A. A. Myatiev, G. Schütz, E. J. Goering, T. Tietze, and B. Baretzky, "Grain boundaries as the controlling factor for the ferromagnetic behaviour of co-doped zno," *Philosophical Magazine*, vol. 93, no. 10-12, pp. 1371–1383, 2013.

[8] B. B. Straumal, S. G. Protasova, A. A. Mazilkin, T. Tietze, E. Goering, G. Schütz, P. B. Straumal, and B. Baretzky, "Ferromagnetic behaviour of fe-doped zno nanograined films," *Beilstein journal of nanotechnology*, vol. 4, p. 361, 2013.

[9] B. B. Straumal, S. G. Protasova, A. A. Mazilkin, E. Goering, G. Schütz, P. B. Straumal, and B. Baretzky, "Ferromagnetic behaviour of zno: the role of grain boundaries," *Beilstein journal of nanotechnology*, vol. 7, no. 1, pp. 1936–1947, 2016.

[10] H. Ohno, "Making nonmagnetic semiconductors ferromagnetic," *science*, vol. 281, no. 5379, pp. 951–956, 1998.

[11] S. Ghosh, V. Sih, W. Lau, D. Awschalom, S.-Y. Bae, S. Wang, S. Vaidya, and G. Chapline, "Room-temperature spin coherence in zno," *Applied Physics Letters*, vol. 86, no. 23, p. 232507, 2005.

[12] Ü. Özgür, Y. I. Alivov, C. Liu, A. Teke, M. Reshchikov, S. Doğan, V. Avrutin, S.-J. Cho, and H. Morkoç, "A comprehensive review of zno materials and devices," *Journal of applied physics*, vol. 98, no. 4, p. 11, 2005.

[13] C. Song, X. Liu, F. Zeng, and F. Pan, "Fully epitaxial (zn, co) o/ zn o/(zn, co) o junction and its tunnel magnetoresistance," *Applied Physics Letters*, vol. 91, no. 4, p. 042106, 2007.

[14] X.-L. Li, Z.-Y. Quan, X.-H. Xu, H.-S. Wu, and G. Gehring, "Magnetoresistance in co/zno films," *IEEE Transactions on Magnetics*, vol. 44, no. 11, pp. 2684–2687, 2008.

[15] M. Hamieh, N. Jedrecy, C. Hebert, D. Demaille, and J. Perriere, "Ferromagnetism and magnetoresistance of nanocomposite zno-co thin films," *Physical Review B*, vol. 92, no. 15, p. 155302, 2015.

[16] X. Li, J. Jia, Y. Li, Y. Bai, J. Li, Y. Shi, L. Wang, and X. Xu, "Realization of resistive switching and magnetoresistance in zno/zno-co composite materials," *Scientific reports*, vol. 6, p. 31934, 2016.

[17] K. R. Kittilstved, W. K. Liu, and D. R. Gamelin, "Electronic structure origins of polarity-dependent high-t c ferromagnetism in oxide-diluted magnetic semiconductors," *Nature materials*, vol. 5, no. 4, p. 291, 2006.

[18] M. Opel, S. T. Goennenwein, M. Althammer, K.-W. Nielsen, E.-M. Karrer-Müller, S. Bauer, K. Senn, C. Schwark, C. Weier, G. Güntherodt, *et al.*, "Zinc oxide–from dilute magnetic doping to spin transport," *physica status solidi (b)*, vol. 251, no. 9, pp. 1700–1709, 2014.

[19] S. B. Ogale, "Dilute doping, defects, and ferromagnetism in metal oxide systems," *Advanced materials*, vol. 22, no. 29, pp. 3125–3155, 2010.

[20] M. Gacic, G. Jakob, C. Herbort, H. Adrian, T. Tietze, S. Brück, and E. Goering, "Magnetism of co-doped zno thin films," *Physical Review B*, vol. 75, no. 20, p. 205206, 2007.

[21] T. C. Kaspar, T. Droubay, S. M. Heald, P. Nachimuthu, C. M. Wang, V. Shutthanandan, C. A. Johnson, D. R. Gamelin, and S. A. Chambers, "Lack of ferromagnetism in n-type cobalt-doped zno epitaxial thin films," *New Journal of Physics*, vol. 10, no. 5, p. 055010, 2008.

[22] C. Rao and F. Deepak, "Absence of ferromagnetism in mn-and co-doped zno," *Journal of Materials Chemistry*, vol. 15, no. 5, pp. 573–578, 2005.

[23] S. Yin, M. Xu, L. Yang, J. Liu, H. Rösner, H. Hahn, H. Gleiter, D. Schild, S. Doyle, T. Liu, *et al.*, "Absence of ferromagnetism in bulk polycrystalline zn 0.9 co 0.1 o," *Physical Review B*, vol. 73, no. 22, p. 224408, 2006.

[24] M. Ying, H. J. Blythe, W. Dizayee, S. M. Heald, F. M. Gerriu, A. M. Fox, and G. A. Gehring, "Advantageous use of metallic cobalt in the target for pulsed laser deposition of cobalt-doped zno films," *Applied Physics Letters*, vol. 109, no. 7, p. 072403, 2016.

[25] D. Norton, M. Overberg, S. Pearton, K. Pruessner, J. Budai, L. Boatner, M. Chisholm, J. Lee, Z. Khim, Y. Park, *et al.*, "Ferromagnetism in cobalt-implanted zno," *Applied Physics Letters*, vol. 83, no. 26, pp. 5488–5490, 2003.

[26] S. M. Heald, T. Kaspar, T. Droubay, V. Shutthanandan, S. Chambers, A. Mokhtari, A. J. Behan, H. J. Blythe, J. R. Neal, A. M. Fox, *et al.*, "X-ray absorption fine structure and magnetization characterization of the metallic co component in co-doped zno thin films," *Physical Review B*, vol. 79, no. 7, p. 075202, 2009.

[27] Q. Feng, W. Dizayee, X. Li, D. S. Score, J. R. Neal, A. J. Behan, A. Mokhtari, M. S. Alshammari, M. S. Al-Qahtani, H. J. Blythe, *et al.*, "Enhanced magnetic properties in zncoalo caused by exchange-coupling to co nanoparticles," *New Journal of Physics*, vol. 18, no. 11, p. 113040, 2016.

[28] Z. Quan, X. Zhang, W. Liu, X. Li, K. Addison, G. A. Gehring, and X. Xu, "Enhanced room temperature magnetoresistance and spin injection from metallic cobalt in co/zno and co/znalo films," *ACS applied materials & interfaces*, vol. 5, no. 9, pp. 3607–3613, 2013.

[29] C. Kittel, P. McEuen, and P. McEuen, *Introduction to solid state physics*, vol. 8. Wiley New York, 1996.

[30] B. D. Cullity and C. D. Graham, *Introduction to magnetic materials*. John Wiley & Sons, 2011.

[31] J. M. Coey, *Magnetism and magnetic materials*. Cambridge University Press, 2010.

[32] N. A. Spaldin and N. D. Mathur, "Magnetic materials: Fundamentals and device applications," *Physics Today*, vol. 56, no. 12, pp. 62–63, 2003.

[33] J. Crangle, *Solid· State Magnetism*. Springer Science & Business Media, 2012.

[34] S. Blundell, *Magnetism in condensed matter*. Oxford Univ. Press, 2001.

[35] M. Levine, A. Heath, *et al.*, "Quantum chemistry," 1991.

[36] S. Chikazumi and C. D. Graham, *Physics of Ferromagnetism 2e*, vol. 94. Oxford University Press on Demand, 2009.

[37] J. B. Goodenough, "Goodenough-kanamori rule," *Scholarpedia*, vol. 3, no. 10, p. 7382, 2008.

[38] M. Opel, "Spintronic oxides grown by laser-mbe," *Journal of Physics D: Applied Physics*, vol. 45, no. 3, p. 033001, 2011.

[39] M. Getzlaff, *Fundamentals of magnetism*. Springer Science & Business Media, 2007.

[40] M. Marolt, "Superparamagnetic materials," seminar, 2014.

[41] R. Torchio, *Magnetism, structure and chemical order in 3d metals ad their alloys at extreme pressures*. PhD thesis, Université de Grenoble, 2012.

[42] S. A. Majetich, T. Wen, and O. T. Mefford, "Magnetic nanoparticles," *MRS Bulletin*, vol. 38, no. 11, pp. 899–903, 2013.

[43] L. Néel, "Théorie du traînage magnétique des ferromagnétiques en grains fins avec application aux terres cuites," *Ann. géophys.*, vol. 5, pp. 99–136, 1949.

[44] C. Bean and u. D. Livingston, "Superparamagnetism," *Journal of Applied Physics*, vol. 30, no. 4, pp. S120–S129, 1959.

[45] Wikipedia, "Wikipedia."

[46] P. Mallet, C.-A. Guérin, and A. Sentenac, "Maxwell-garnett mixing rule in the presence of multiple scattering: Derivation and accuracy," *Physical Review B*, vol. 72, no. 1, p. 014205, 2005.

[47] Y. Matsumoto, M. Murakami, T. Shono, T. Hasegawa, T. Fukumura, M. Kawasaki, P. Ahmet, T. Chikyow, S.-y. Koshihara, and H. Koinuma, "Room-temperature ferromagnetism in transparent transition metal-doped titanium dioxide," *Science*, vol. 291, no. 5505, pp. 854–856, 2001.

[48] S. Ogale, R. Choudhary, J. Buban, S. Lofland, S. Shinde, S. Kale, V. Kulkarni, J. Higgins, C. Lanci, J. Simpson, *et al.*, "High temperature ferromagnetism with a

giant magnetic moment in transparent co-doped s n o 2- δ," *Physical Review Letters*, vol. 91, no. 7, p. 077205, 2003.

[49] M. Venkatesan, C. Fitzgerald, J. Lunney, and J. Coey, "Anisotropic ferromagnetism in substituted zinc oxide," *Physical review letters*, vol. 93, no. 17, p. 177206, 2004.

[50] J. Coey, "Dilute magnetic oxides," *Current Opinion in Solid State and Materials Science*, vol. 10, no. 2, pp. 83–92, 2006.

[51] M. Venkatesan, C. Fitzgerald, and J. Coey, "Thin films: unexpected magnetism in a dielectric oxide," *Nature*, vol. 430, no. 7000, p. 630, 2004.

[52] N. H. Hong, J. Sakai, N. Poirot, and V. Brizé, "Room-temperature ferromagnetism observed in undoped semiconducting and insulating oxide thin films," *Physical Review B*, vol. 73, no. 13, p. 132404, 2006.

[53] N. Khare, M. J. Kappers, M. Wei, M. G. Blamire, and J. L. MacManus-Driscoll, "Defect-induced ferromagnetism in co-doped zno," *Advanced Materials*, vol. 18, no. 11, pp. 1449–1452, 2006.

[54] P. Zhan, Z. Xie, Z. Li, W. Wang, Z. Zhang, Z. Li, G. Cheng, P. Zhang, B. Wang, and X. Cao, "Origin of the defects-induced ferromagnetism in un-doped zno single crystals," *Applied Physics Letters*, vol. 102, no. 7, p. 071914, 2013.

[55] J. M. D. Coey, P. Stamenov, R. Gunning, M. Venkatesan, and K. Paul, "Ferromagnetism in defect-ridden oxides and related materials," *New Journal of Physics*, vol. 12, no. 5, p. 053025, 2010.

[56] J. Neal, A. Behan, R. M. Ibrahim, H. Blythe, M. Ziese, A. Fox, and G. Gehring, "Room-temperature magneto-optics of ferromagnetic transition-metal-doped zno thin films," *Physical review letters*, vol. 96, no. 19, p. 197208, 2006.

[57] A. Janotti and C. G. Van de Walle, "Native point defects in zno," *Physical Review B*, vol. 76, no. 16, p. 165202, 2007.

[58] A. Janotti and C. G. Van de Walle, "Fundamentals of zinc oxide as a semiconductor," *Reports on progress in physics*, vol. 72, no. 12, p. 126501, 2009.

[59] A. Kohan, G. Ceder, D. Morgan, and C. G. Van de Walle, "First-principles study of native point defects in zno," *Physical Review B*, vol. 61, no. 22, p. 15019, 2000.

[60] X. Wu, G. Siu, C. Fu, and H. Ong, "Photoluminescence and cathodoluminescence studies of stoichiometric and oxygen-deficient zno films," *Applied Physics Letters*, vol. 78, no. 16, pp. 2285–2287, 2001.

[61] K. Vanheusden, W. Warren, C. Seager, D. Tallant, J. Voigt, and B. Gnade, "Mechanisms behind green photoluminescence in zno phosphor powders," *Journal of Applied Physics*, vol. 79, no. 10, pp. 7983–7990, 1996.

[62] K. Kodama and T. Uchino, "Thermally activated below-band-gap excitation behind green photoluminescence in zno," *Journal of Applied Physics*, vol. 111, no. 9, p. 093525, 2012.

[63] B. Lin, Z. Fu, and Y. Jia, "Green luminescent center in undoped zinc oxide films deposited on silicon substrates," *Applied physics letters*, vol. 79, no. 7, pp. 943–945, 2001.

[64] P. Sagar, P. Shishodia, R. Mehra, H. Okada, A. Wakahara, and A. Yoshida, "Photoluminescence and absorption in sol–gel-derived zno films," *Journal of Luminescence*, vol. 126, no. 2, pp. 800–806, 2007.

[65] Y.-S. Kim, W.-P. Tai, and S.-J. Shu, "Effect of preheating temperature on structural and optical properties of zno thin films by sol–gel process," *Thin Solid Films*, vol. 491, no. 1-2, pp. 153–160, 2005.

[66] F. Fabbri, M. Villani, A. Catellani, A. Calzolari, G. Cicero, D. Calestani, G. Calestani, A. Zappettini, B. Dierre, T. Sekiguchi, *et al.*, "Zn vacancy induced green luminescence on non-polar surfaces in zno nanostructures," *scientific reports*, vol. 4, p. 5158, 2014.

[67] J. Čížek, J. Valenta, P. Hruška, O. Melikhova, I. Procházka, M. Novotnỳ, and J. Bulíř, "Origin of green luminescence in hydrothermally grown zno single crystals," *Applied Physics Letters*, vol. 106, no. 25, p. 251902, 2015.

[68] H. Villarraga Gomes, "Magneto-optical studies of cobalt-doped nickel oxide thin films," 2010.

[69] M. Ying, W. Dizayee, Z. Mei, X. Du, A. M. Fox, and G. A. Gehring, "Zno gap states investigated using magnetic circular dichroism," *Journal of Physics D: Applied Physics*, vol. 48, no. 25, p. 255502, 2015.

[70] D. S. Score, M. Alshammari, Q. Feng, H. J. Blythe, A. M. Fox, G. A. Gehring, Z.-Y. Quan, X.-L. Li, and X.-H. Xu, "Magneto-optical properties of co/zno multilayer films," in *Journal of Physics: Conference Series*, vol. 200, p. 062024, IOP Publishing, 2010.

[71] K. R. Kittilstved, J. Zhao, W. K. Liu, J. D. Bryan, D. A. Schwartz, and D. R. Gamelin, "Magnetic circular dichroism of ferromagnetic co 2+-doped zno," *Applied physics letters*, vol. 89, no. 6, p. 062510, 2006.

[72] M. Ying, S. Wang, T. Duan, B. Liao, X. Zhang, Z. Mei, X. Du, F. Gerriu, A. Fox, and G. Gehring, "The structure, optical and magnetic properties of arsenic implanted zno films prepared by molecular beam epitaxy," *Materials Letters*, vol. 171, pp. 121–124, 2016.

[73] A. Behan, A. Mokhtari, H. Blythe, D. Score, X. Xu, J. Neal, A. Fox, and G. Gehring, "Two magnetic regimes in doped zno corresponding to a dilute magnetic semiconductor and a dilute magnetic insulator," *Physical review letters*, vol. 100, no. 4, p. 047206, 2008.

[74] G. A. Gehring, M. S. Alshammari, D. S. Score, J. R. Neal, A. Mokhtari, and A. M. Fox, "Magneto-optic studies of magnetic oxides," *Journal of Magnetism and Magnetic Materials*, vol. 324, no. 21, pp. 3422–3426, 2012.

[75] A. Ali, F. Dejene, and H. Swart, "Effect of mn doping on the structural and optical properties of sol-gel derived zno nanoparticles," *Open Physics*, vol. 10, no. 2, pp. 478–484, 2012.

[76] L. Zhi-Fu, L. Yong-Xiang, S. Fu-Kai, X. Zhi-Hua, and Y. Yun-Sik, "Highly c-oriented nanocolumn structure zno films on sapphire substrates by pulsed laser deposition," *Chinese Physics Letters*, vol. 21, no. 4, p. 747, 2004.

[77] M. Pryce, "A modified perturbation procedure for a problem in paramagnetism," *Proceedings of the Physical Society. Section A*, vol. 63, no. 1, p. 25, 1950.

[78] L. Vlasenko and G. Watkins, "Optical detection of electron paramagnetic resonance for intrinsic defects produced in zno by 2.5-mev electron irradiation in situ at 4.2 k," *Physical Review B*, vol. 72, no. 3, p. 035203, 2005.

[79] R. Bartram, C. Swenberg, and S. La, "Theory of f-center g values in divalent compounds," *Physical Review*, vol. 162, no. 3, p. 759, 1967.

[80] D. Gullberg and U. Litzén, "Accurately measured wavelengths of zn i and zn ii lines of astrophysical interest," *Physica Scripta*, vol. 61, no. 6, p. 652, 2000.

[81] D. Wang, Z. Chen, D. Wang, N. Qi, J. Gong, C. Cao, and Z. Tang, "Positron annihilation study of the interfacial defects in zno nanocrystals: Correlation with ferromagnetism," *Journal of Applied Physics*, vol. 107, no. 2, p. 023524, 2010.

[82] Y. Li, R. Deng, B. Yao, G. Xing, D. Wang, and T. Wu, "Tuning ferromagnetism in mg x zn 1- x o thin films by band gap and defect engineering," *Applied Physics Letters*, vol. 97, no. 10, p. 102506, 2010.

[83] J. Yi, C. Lim, G. Xing, H. Fan, L. Van, S. Huang, K. Yang, X. Huang, X. Qin, B. Wang, *et al.*, "Ferromagnetism in dilute magnetic semiconductors through defect engineering: Li-doped zno," *Physical review letters*, vol. 104, no. 13, p. 137201, 2010.

[84] T. Gupta and A. Miller, "Improved stability of the zno varistor via donor and acceptor doping at the grain boundary," *Journal of Materials Research*, vol. 3, no. 4, pp. 745–754, 1988.

[85] H. Peng, H. Xiang, S.-H. Wei, S.-S. Li, J.-B. Xia, and J. Li, "Origin and enhancement of hole-induced ferromagnetism in first-row d 0 semiconductors," *Physical review letters*, vol. 102, no. 1, p. 017201, 2009.

[86] H.-B. Wang, L.-M. Tang, P. Peng, Y.-H. Tang, and K.-Q. Chen, "Enhancement of the hole-induced d0-ferromagnetism in zno through compensated donor–acceptor complexes: a first-principles study," *Semiconductor Science and Technology*, vol. 28, no. 3, p. 035017, 2013.

[87] P. Hohenberg and W. Kohn, "Inhomogeneous electron gas," *Physical review*, vol. 136, no. 3B, p. B864, 1964.

[88] W. Kohn and L. J. Sham, "Self-consistent equations including exchange and correlation effects," *Physical review*, vol. 140, no. 4A, p. A1133, 1965.

[89] R. O. Jones, "Density functional theory: Its origins, rise to prominence, and future," *Reviews of modern physics*, vol. 87, no. 3, p. 897, 2015.

[90] D. Sholl and J. A. Steckel, *Density functional theory: a practical introduction*. John Wiley & Sons, 2011.

[91] F. Giustino, *Materials modelling using density functional theory: properties and predictions*. Oxford University Press, 2014.

[92] R. M. Martin, *Electronic structure: basic theory and practical methods*. Cambridge university press, 2004.

[93] E. Gross and W. Kohn, "Local density-functional theory of frequency-dependent linear response," *Physical review letters*, vol. 55, no. 26, p. 2850, 1985.

[94] P. A. Dirac, "Note on exchange phenomena in the thomas atom," in *Mathematical Proceedings of the Cambridge Philosophical Society*, vol. 26, pp. 376–385, Cambridge University Press, 1930.

[95] J. P. Perdew and Y. Wang, "Accurate and simple analytic representation of the electron-gas correlation energy," *Physical Review B*, vol. 45, no. 23, p. 13244, 1992.

[96] F. Herman, J. P. Van Dyke, and I. B. Ortenburger, "Improved statistical exchange approximation for inhomogeneous many-electron systems," *Physical Review Letters*, vol. 22, no. 16, p. 807, 1969.

[97] A. D. Becke, "Density-functional exchange-energy approximation with correct asymptotic behavior," *Physical review A*, vol. 38, no. 6, p. 3098, 1988.

[98] J. P. Perdew, K. Burke, and M. Ernzerhof, "Generalized gradient approximation made simple," *Physical review letters*, vol. 77, no. 18, p. 3865, 1996.

[99] V. I. Anisimov, F. Aryasetiawan, and A. Lichtenstein, "First-principles calculations of the electronic structure and spectra of strongly correlated systems: the lda+ u method," *Journal of Physics: Condensed Matter*, vol. 9, no. 4, p. 767, 1997.

[100] V. I. Anisimov, J. Zaanen, and O. K. Andersen, "Band theory and mott insulators: Hubbard u instead of stoner i," *Physical Review B*, vol. 44, no. 3, p. 943, 1991.

[101] J. Hubbard, "Electron correlations in narrow energy bands-iv. the atomic representation," in *Proc. R. Soc. Lond. A*, vol. 285, pp. 542–560, The Royal Society, 1965.

[102] R. Powell and W. Spicer, "Optical properties of nio and coo," *Physical Review B*, vol. 2, no. 6, p. 2182, 1970.

[103] S. Hüfner, P. Steiner, I. Sander, F. Reinert, and H. Schmitt, "The optical gap of nio," *Zeitschrift für Physik B Condensed Matter*, vol. 86, no. 2, pp. 207–215, 1992.

[104] K. Terakura, T. Oguchi, A. Williams, and J. Kübler, "Band theory of insulating transition-metal monoxides: Band-structure calculations," *Physical Review B*, vol. 30, no. 8, p. 4734, 1984.

[105] P. Gopal and N. A. Spaldin, "Magnetic interactions in transition-metal-doped zno: An ab initio study," *Physical Review B*, vol. 74, no. 9, p. 094418, 2006.

[106] P. Gopal, R. De Gennaro, M. S. dos Santos Gusmao, R. A. R. Al Orabi, H. Wang, S. Curtarolo, M. Fornari, and M. B. Nardelli, "Improved electronic structure and magnetic exchange interactions in transition metal oxides," *Journal of Physics: Condensed Matter*, vol. 29, no. 44, p. 444003, 2017.

[107] H. J. Monkhorst and J. D. Pack, "Special points for brillouin-zone integrations," *Physical review B*, vol. 13, no. 12, p. 5188, 1976.

[108] J. D. Pack and H. J. Monkhorst, """ special points for brillouin-zone integrations"—a reply," *Physical Review B*, vol. 16, no. 4, p. 1748, 1977.

[109] R. Janisch and N. A. Spaldin, "Understanding ferromagnetism in co-doped ti o 2 anatase from first principles," *Physical Review B*, vol. 73, no. 3, p. 035201, 2006.

[110] M. Methfessel and A. Paxton, "High-precision sampling for brillouin-zone integration in metals," *Physical Review B*, vol. 40, no. 6, p. 3616, 1989.

[111] P. E. Blöchl, O. Jepsen, and O. K. Andersen, "Improved tetrahedron method for brillouin-zone integrations," *Physical Review B*, vol. 49, no. 23, p. 16223, 1994.

[112] D. Vanderbilt, "Soft self-consistent pseudopotentials in a generalized eigenvalue formalism," *Physical Review B*, vol. 41, no. 11, p. 7892, 1990.

[113] A. Marini, G. Onida, and R. Del Sole, "Plane-wave dft-lda calculation of the electronic structure and absorption spectrum of copper," *Physical Review B*, vol. 64, no. 19, p. 195125, 2001.

[114] V. A. de la Peña O'Shea, I. d. P. Moreira, A. Roldán, and F. Illas, "Electronic and magnetic structure of bulk cobalt: The α, β, and ε-phases from density functional theory calculations," *The Journal of chemical physics*, vol. 133, no. 2, p. 024701, 2010.

[115] H. Gaigher and N. Van Der Berg, "The fcc-hcp phase transition in electrodeposited epitaxial cobalt films," *Electrochimica Acta*, vol. 21, no. 1, pp. 45–49, 1976.

[116] H. Yang, C. Shen, Y. Su, T. Yang, H. Gao, and Y. Wang, "Self-assembly and magnetic properties of cobalt nanoparticles," *Applied physics letters*, vol. 82, no. 26, pp. 4729–4731, 2003.

[117] V. F. Puntes and K. M. Krishnan, "Synthesis, structural order and magnetic behavior of self-assembled/spl epsi/-co nanocrystal arrays," *IEEE transactions on magnetics*, vol. 37, no. 4, pp. 2210–2212, 2001.

[118] D. P. Dinega and M. Bawendi, "A solution-phase chemical approach to a new crystal structure of cobalt," *Angewandte Chemie International Edition*, vol. 38, no. 12, pp. 1788–1791, 1999.

[119] M. Opel, K.-W. Nielsen, S. Bauer, S. T. Goennenwein, J. Cezar, D. Schmeißer, J. Simon, W. Mader, and R. Gross, "Nanosized superparamagnetic precipitates in cobalt-doped zno," *The European Physical Journal B*, vol. 63, no. 4, p. 437, 2008.

[120] A. Ali and R. Henda, "Effect of post-annealing on the properties of co-doped zno thin films deposited by channel-spark ablation," *Materials Science in Semiconductor Processing*, vol. 84, pp. 24–35, 2018.

[121] Y. Wang, L. Sun, L.-G. Kong, J.-F. Kang, X. Zhang, and R.-Q. Han, "Room-temperature ferromagnetism in co-doped zno bulk induced by hydrogenation," *Journal of alloys and compounds*, vol. 423, no. 1-2, pp. 256–259, 2006.

[122] J. Bubendorff, C. Meny, E. Beaurepaire, P. Panissod, and J. Bucher, "Electrodeposited cobalt films: hcp versus fcc nanostructuring and magnetic properties," *The European Physical Journal B-Condensed Matter and Complex Systems*, vol. 17, no. 4, pp. 635–643, 2000.

[123] J. Chakraborty, K. Kumar, R. Ranjan, S. G. Chowdhury, and S. Singh, "Thickness-dependent fcc–hcp phase transformation in polycrystalline titanium thin films," *Acta Materialia*, vol. 59, no. 7, pp. 2615–2623, 2011.

[124] D. Chiba, N. Shibata, and A. Tsukazaki, "Co thin films deposited directly on zno polar surfaces," *Scientific reports*, vol. 6, p. 38005, 2016.

[125] N. Jedrecy, H. Von Bardeleben, and D. Demaille, "High-temperature ferromagnetism by means of oriented nanocolumns: Co clustering in (zn, co) o," *Physical Review B*, vol. 80, no. 20, p. 205204, 2009.

[126] N. Jedrecy, M. Hamieh, C. Hebert, and J. Perriere, "High magnetoresistance at low magnetic fields in self-assembled zno–co nanocomposite films," *Nanoscale*, vol. 9, no. 29, pp. 10431–10439, 2017.

[127] Y.-S. Kim, S.-H. Lee, J.-I. Im, and Y.-C. Chung, "Magnetic properties and electronic structure of transition metal adsorbed polar-zno surfaces: Ab initio calculations," *Japanese Journal of Applied Physics*, vol. 46, no. 9S, p. 6312, 2007.

[128] X. Chen, D. Huang, W.-J. Deng, and Y.-J. Zhao, "Structural stability and magnetic properties of co-doped or adsorbed polar-zno surface," *Physics Letters A*, vol. 373, no. 3, pp. 391–395, 2009.

[129] J. A. Dumont, M. C. Mugumaoderha, J. Ghijsen, S. Thiess, W. Drube, B. Walz, M. Tolkiehn, D. Novikov, F. M. de Groot, and R. Sporken, "Thermally activated processes at the co/zno interface elucidated using high energy x-rays," *The Journal of Physical Chemistry C*, vol. 115, no. 15, pp. 7411–7418, 2011.

[130] Z.-Y. Quan, X.-H. Xu, X.-L. Li, Q. Feng, and G. Gehring, "Investigation of structure and magnetoresistance in co/zno films," *Journal of Applied Physics*, vol. 108, no. 10, p. 103912, 2010.

[131] Z. Wang, H. Zhao, Q. Yao, J. Xu, and H. Kimura, "The influence of layer thickness and post annealing on magnetism of pulsed laser deposited zno/co multilayers," *Journal of Magnetism and Magnetic Materials*, vol. 345, pp. 41–47, 2013.

[132] Z.-Y. Quan, X.-P. Zhang, W. Liu, H. Albargi, G. Gehring, and X.-H. Xu, "Structural and magnetotransport properties of ultrathin co/zno and co/znalo films," *Journal of Applied Physics*, vol. 115, no. 23, p. 233908, 2014.

[133] Z.-Y. Quan, L. Zhang, W. Liu, H. Zeng, and X.-H. Xu, "Resistivity dependence of magnetoresistance in co/zno films," *Nanoscale research letters*, vol. 9, no. 1, p. 6, 2014.

[134] P. J. Kelly and R. D. Arnell, "Magnetron sputtering: a review of recent developments and applications," *Vacuum*, vol. 56, no. 3, pp. 159–172, 2000.

[135] S. J. Clark, M. D. Segall, C. J. Pickard, P. J. Hasnip, M. I. Probert, K. Refson, and M. C. Payne, "First principles methods using castep," *Zeitschrift für Kristallographie-Crystalline Materials*, vol. 220, no. 5/6, pp. 567–570, 2005.

[136] R. Janisch, P. Gopal, and N. A. Spaldin, "Transition metal-doped tio2 and zno—present status of the field," *Journal of Physics: Condensed Matter*, vol. 17, no. 27, p. R657, 2005.

[137] R. Nicholls, A. Morris, C. Pickard, and J. Yates, "Optados-a new tool for eels calculations," in *Journal of Physics: Conference Series*, vol. 371, p. 012062, IOP Publishing, 2012.

[138] M. Yaakob, N. Hussin, M. Taib, T. Kudin, O. Hassan, A. Ali, and M. Yahya, "First principles lda+ u calculations for zno materials," *Integrated Ferroelectrics*, vol. 155, no. 1, pp. 15–22, 2014.